UNIVERSITY OF ILLINOIS
URBANA

AERONOMY REPORT NO. 118

SOLAR FLARE IONIZATION IN THE MESOSPHERE OBSERVED BY COHERENT-SCATTER RADAR

by
J. W. Parker
S. A. Bowhill

January 1, 1986

Library of Congress ISSN 0568-0581

Supported by
National Aeronautics and Space Administration
National Science Foundation

Aeronomy Laboratory
Department of Electrical and Computer Engineering
University of Illinois
Urbana, Illinois

UILU-ENG-86-2501

A E R O N O M Y R E P O R T

N O. 118

SOLAR FLARE IONIZATION IN THE MESOSPHERE OBSERVED BY COHERENT-SCATTER RADAR

by

J. W. Parker
S. A. Bowhill

January 1, 1986

Supported by
National Aeronautics
and Space Administration
Grant NSG 7506
National Science Foundation
ATM 81-20371

Aeronomy Laboratory
Department of Electrical and
Computer Engineering
University of Illinois
Urbana, Illinois

ABSTRACT

The coherent-scatter technique, as used with the Urbana radar, is able to measure relative changes in electron density at one altitude during the progress of a solar flare when that altitude contains a statistically steady turbulent layer. This work describes the analysis of Urbana coherent-scatter data from the times of 13 solar flares in the period from 1978 to 1983. Previous methods of measuring electron density changes in the D-region are summarized. Models of X-ray spectra, photoionization rates, and ion-recombination reaction schemes are reviewed. The coherent-scatter technique is briefly described, and a model is developed which relates changes in scattered power to changes in electron density. An analysis technique is developed using X-ray flux data from geostationary satellites and coherent scatter data from the Urbana radar which empirically distinguishes between proposed D-region ion-chemical schemes, and estimates the nonflare ion-pair production rate.

TABLE OF CONTENTS

LIST OF FIGURES

1. INTRODUCTION

1.1 Significance of D-region flare effects

The study of the ionosphere has several unusual features as a scientific discipline. As in astronomy, the subject matter is remote. Therefore, the investigator must (usually) wait and watch for revealing natural conditions, rather than setting up controlled experiments under conditions of his own choosing.

Unlike astronomy, ionospheric studies have a short history. All of the methods used to observe the ionosphere may be regarded as modern, developed in this century. Radio communication links yielded much of the early data about the ionosphere, but ionospheric observations were usually a secondary consideration, the primary goal being the establishment of reliable and inexpensive long-range communication. More recent methods include in situ rocket probes and satellites, as well as earth- and satellite-based remote sensing devices such as radar and lidar.

Early in the commercial use of the ionosphere as a means of extending radio broadcasting range, anomalous patterns of behavior were discovered. Many of these interrupted communications, increasing interest in the disturbed ionosphere as a nuisance. Now that more methods are used to examine the ionosphere as a subject in its own right, much ionospheric research still centers on disturbed conditions. This is so because the subject is remote, and dependencies of observed quantities upon conditions are quite complex. Brief disturbances provide the observer with a time when only a few conditions are changed, but most remain constant. Thus interpretation of the effects is simplified. Solar flares have proved to be particularly useful phenomena from this point of view. They provide the

ionospheric researcher a brief time period in which parts of the spectrum of electromagnetic radiation from the sun change drastically, and some of the observable properties of the ionosphere change a corresponding amount. The fact that flares are of short duration gives a high probability that other control variables will remain relatively constant.

Satellite monitoring of solar radiation now provides a reasonably good estimate of the change in conditions at the time of the observed changes in ionospheric features. The D region of the ionosphere has shown the largest relative changes due to solar flares. Therefore, it has been the primary focus of studies of the flare-disturbed ionosphere.

1.2 Prior studies of D-region flare effects

The discovery of sudden D-region electron density enhancements and the conclusion that their cause is of solar origin are summarized by Dellinger (1937). The enhancement in electron density is deduced in that work from HF radio blackouts. Further, the sun is deduced to be the cause by the facts that incidences of such blackouts are confined to the sunlit hemisphere, and that the severity of the blackouts is greatest for small solar zenith angles. The observed fadeouts occurred from 1934 to 1936. Dellinger concludes that the disturbances are due to electromagnetic radiation of a variety different from that forming the E and F layers, and also different from any detectable from the earth's surface. He also reports confirmation from astronomical observatories that visible disturbances on the sun coincide with the ionospheric disturbances.

More recent works focusing on ionospheric effects of solar flares include an extended summary of theory and results by Mitra (1974), which expands on a series of articles by Deshpande and Mitra (Deshpande et al. 1972a and 1972b; and Deshpande and Mitra 1972a, 1972b, and 1972c). These

works are drawn upon heavily in the present study. An effort to describe the expected radio propagation disturbances based on satellite observations of X-ray events has been undertaken by Bleiweiss (1972). There are also several surveys which examine the frequency of joint occurrences of types and magnitudes of solar flare events with ionospheric disturbances. Particularly important are those of Kreplin et al. (1962) and Deshpande et al. (1972a) which relate such disturbances to solar X-ray events.

1.3 Scope of this study

This study is confined to effects in the D region. The D region is defined to be the part of the ionosphere in the altitude range 60-90 km, the lowest layer. It happens that this is largely coterminous with the mesosphere, defined to be the region of negative temperature gradient between about 50 and 85 km. Thus the terms "D region" and "mesosphere" refer to nearly the same region of the atmosphere, depending on whether the context involves ion densities or temperature gradient. The D region is weakly ionized, even when disturbed.

The combined air molecular number density in the D region is about 10^{20} to 10^{22} m^{-3} (NOAA, 1976), and the electron density is typically about 10^{8} to 10^{10} m^{-3} during the day (Hargreaves, 1979). Thus the maximum ratio of electrons to molecules is thus on the order of 10^{-10}. In contrast, the F region may reach ionization ratios exceeding 10^{-3} near 300 km (comparison of NOAA, 1976 and Hargreaves, 1979).

Turbulence exists in the atmosphere to an altitude of about 100 km. In the D region, this turbulence acts upon the vertical gradient of electron density. Because the ionization levels are so small, the ions follow the motion of turbulent neutral air, causing small-scale irregularities in electron density. This creates a scattering mechanism for VHF radio waves.

Investigation of this phenomenon has been carried out at Urbana since 1978, using a technique called coherent-scatter radar. A large database of observations has been collected since that time, including several time periods which overlap major solar flare events. This is the primary data used in this work.

Different sorts of analyses are required to investigate delayed effects of flares such as Polar Cap Absorption (PCA) events and magnetic storms. These are not dealt with in this work.

1.4 Statement of the problem

Current theories of solar flare emissions, D-region chemistry, and coherent scatter allow us to expect a flare-time effect observable with coherent-scatter radar. This effect has been observed in past studies (Miller et al. 1978, and Rottger, 1983) but never analyzed or discussed in any detail. The objective of this work is to map out some of the areas of knowledge which may be expanded by the analysis of the data from the coherent-scatter observations of D-region flare effects. The database of the Urbana radar is searched for such effects, and the occurrences of flare-time effects are noted. These events form the basis for the analysis and conclusions of this work.

Some of the questions to be examined are quite general. What is roughly the minimum size of solar flare required to cause an effect? Which altitude ranges show coherent scatter enhancements during a solar flare? How does the information gained by coherent-scatter observation compare with the observation of D-region flare effects by older methods? What sort of limitations are specifically due to the nature of clear-air turbulence which produces the scattered power, and what sorts of features of mesospheric turbulence does this indicate?

More detailed questions arise from the comparison of the observed responses with those predicted by current theories. One of the areas of theory which is still incomplete is the chemical reaction scheme of the D region. More than one sort of D-region chemical model may apply, depending on geophysical conditions. We seek to determine which model best describes each flare enhancement in scattered power. There is one particular aspect of these models which we consider in this work: the relationship between the solar flare ion production rate at a given altitude, and the electron density at that altitude. The models and observations of past works usually imply three possible forms for this relationship: quadratic, linear, and delayed. Analysis is performed in this work to determine, when possible, which of these forms best describes the observed coherent-scatter effect.

This leads to quite specific questions. When can we account for the features (size, decay rate, smoothness) by these chemical theories, and which models seem to apply under which conditions? Zenith angle and seasonality are two conditions examined. Some geophysical quantities may be estimated from the coherent-scatter data; these are also examined.

Chapter 2 provides historical background, discussing previous methods for studying D-region flare effects. Chapter 3 discusses the solar radiations and chemistry of the ionosphere relevant to these effects. Chapter 4 describes features of the Urbana radar and the underlying theory of coherent scatter which are pertinent to this work. The criteria for choosing flare effects for study and the analysis and interpretation of the chosen events are discussed in Chapter 5.

2. PRIOR METHODS USED TO OBSERVE D-REGION FLARE EFFECTS

2.1 Simple, older methods

A description of the techniques used to detect and observe the immediate response of the D region to solar flares is given in the second chapter of Mitra (1974). The techniques may be divided into two classes: simple methods, which are generally older, and in world-wide continuous use; and sophisticated methods, of recent invention, which are used only on a campaign basis at a few major research facilities. Both types of methods are briefly summarized here, with some additional information about more recent developments.

During the time of rapid improvement and expansion of ionospheric radio communication links in the 1930s, several anomalous types of radio signal behaviors were discovered. Sudden changes in the strength of various forms of environmental radio noise, and changes in the amplitude, phase and frequency of radio signals were found to occur coinciding with optical observations of solar flares. These are known collectively as Sudden Ionospheric Disturbances (SIDs). The equipment necessary for such observations can be as modest as a low-cost receiver and a recording device. Records of various sorts of SIDs are shown in Figure 2.1.

The types of SID which are directly due to D-region effects are:

1. Sudden Enhancement/Decrease of Atmospherics (SEA/SDA). This is a change in the received levels of natural VLF or ELF noise from sources within the atmosphere, such as thunderstorm activity. Excess electron density created by solar flare emissions changes the propagation modes available at these frequencies. The earth and the bottom edge of the ionosphere may be considered at first approximation to be a parallel plate

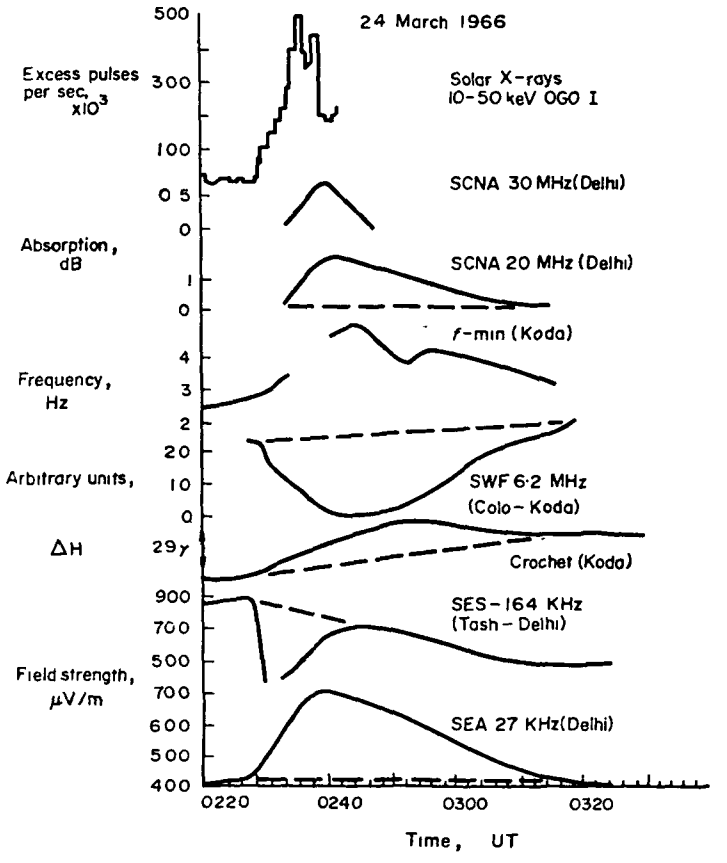

Figure 2.1 Time curves of 10-50 keV X-rays and several SID effects for event of March 24, 1966 (Deshpande, 1972a).

waveguide. Flare enhancement of the electron density in the D region produces two changes in the waveguide. The distance between the plates is reduced, and the effective conductivity of the upper plate increases. Thus higher frequencies in the VLF range, which propagate, have less attenuation, but fewer low frequencies are able to propagate because the cut off frequency rises.

2. Sudden Field Anomalies (SFA), also referred to as Sudden Increases in Long Wave Signals (SIL) and Sudden Enhancements in Signals (SES). These are the same as SEA/SDAs in their cause, the changing effective altitude and conductivity of the ionosphere. However, additional features exist due to the steady frequency, amplitude, and location of the source. In some VLF and LF links, the radio signal arrives at the receiver by two transmission modes, a ground wave, propagating along the line of sight, and a sky wave reflected from the ionosphere. These versions of the same signal may interfere at the receiver, either constructively or destructively. Reducing the effective altitude of the reflection level of the ionosphere changes the relative phase of these waves, which may result in either an increase or decrease in amplitude, depending on the initial relative phase. This is one sort of SFA; on other links, more complicated explanations are required, but the fundamental factor remains a change in the available propagation modes.

3. Sudden Phase Anomalies (SPA). To observe this effect, the phase of the sky-wave of a VLF transmission is measured against some reliable reference phase, such as might be received from the distant transmitter over a telephone line. The phase is observed to advance as the effective altitude of reflection is reduced by the flare effect.

4. Short-wave Fadeouts (SWF). This is an absorption effect of HF radio transmissions. These are reflected at ionospheric levels above the D region.

As the electron density below the reflection point increases, more of the radio signal is absorbed in crossing the D region, in both the upward and downward directions. This was the first flare effect discovered (reported in Dellinger, 1937) and it continues to plague HF communication. It is perhaps the easiest to monitor, but as the recieved radio signal usually decreases to zero early in the flare, it is not possible to use most SWF observations to find the size or the time of maximum of the effect.

5. Sudden Cosmic Noise Absorption (SCNA). This effect is due to changes in ionospheric absorption of radio noise from galactic sources of radio noise. Because of the way in which the complex index of refraction of a plasma depends on the plasma collision frequency, most absorption takes place in the D region. Changes in cosmic radio noise are small, and observations of SCNAs are best performed with a sensitive device called a riometer. This measure of D-region absorption is superior to SWFs in that the absorption is unlikely to be complete, allowing determination of the time and the size of the maximum of the event.

6. Sudden Increase in f_{min} (SIF). The parameter f_{min} is the minimum frequency of echo detectable in an ionosonde scan. The dependence of f_{min} on D-region absorption is complex, making the analysis of SIF events difficult.

One other variety of SID is a Sudden Frequency Deviation (SFD) in an HF radio link. This primarily measures electron density enhancements above the D region, either at an E- or F-region altitude. This effect is not influenced appreciably by D-region changes; in fact, it is not even due to the same region of the spectrum of solar radiation as the D-region effects. However, the occurrence of SFDs is highly correlated with D-region effects, because flares usually produce some enhancement in the wavelengths affecting the upper ionosphere as well as those affecting the lower regions. Thus

SFDs are useful as indicators: where they are observed, we should particularly look for D-region effects as well.

The information from SID observations has several limitations. The methods which depend on the effective altitude of reflection--SEA/SDAs, SFAs, and SPAs-- have two problems in common. First, they indicate only relative changes in altitude; the initial effective height cannot be determined precisely. Second, information about changes in effective height of reflection does not translate directly to changes in electron density at a constant altitude, nor to an electron density vs. altitude profile at a given time. In fact, the concept of an effective height of reflection proves to be too rough an approximation to the true situation; a tedious numerical method is required even to predict the reflection characteristics of a known electron density profile, and to invert this process to obtain such a profile from the reflected signal in a changing environment is even more difficult. In addition, SEA/SDAs and SFAs may be due to a variety of transmission mode effects, so that it is often impossible to model which ionospheric parameters account for the change observed.

The absorption methods--SWFs, SCNAs, and SIFs--are limited in other ways. As noted above, there are problems associated with the usual drop of signal strength to zero for SWFs, and the complex dependency of f_{min} on absorption. Also, all these effects are due to changes in total integrated absorption through the entire D region; thus no altitude resolution is available.

However, several results have been obtained by painstaking analysis of SID observations. Of particular relevance to the study of D-region effects are works detailing the relative frequency of joint occurrences of SIDs and solar X-ray events of differing characteristics, since these are believed to

be in a direct cause and effect relationship. Outstanding works of this sort are an early study by Kreplin et al. (1962) and a more exhaustive analysis by Deshpande et al. (1972a). Kreplin et al. deduce a threshold in 0-0.8 nm X-ray flux (of 2×10^{-6} W m^{-2}) which must be exceeded in order for an SID to occur. Deshpande et al. detail some of the dependences of SID occurrence on the spectral shape of X-ray emissions. A correlation is found to exist between an SID occurrence and the ratio of 0-0.3 nm flux to 0-0.8 nm flux, called the hardening ratio. Flares which produce SIDs nearly always have hardening ratios in excess of 1.5×10^{-2}. Flares with 0-0.8 nm flux below usual for SID occurrence yet which in fact do produce SIDs usually have high hardening ratios.

Other works have examined the time history curves of SIDs. There are several types of analyses which have been attempted; the more successful ones are described by Mitra (1974). One type of analysis attempts to reconstruct an electron density profile from several types of SID observations at several different frequencies for a single event. Other methods examine the time lag between the SID and the presumed causal solar radiation, and the time of recovery to normal after the maximum of the SID. These provide some insights into the chemical electron loss processes in the D region, but for a single event are of more dubious accuracy than the more sophisticated techniques described below. Since the simple methods are in more widespread use, their chief advantage over the more sophisticated methods is the huge amount of data which has been collected in these ways.

2.2 Sophisticated methods

Mitra (1974) also describes several of the sophisticated techniques. The three described below can produce electron density profiles of the D region with adequate time resolution to observe flare effects, as well as

sufficient altitude resolution to distinguish subregions which may show different responses to a solar flare. These techniques are:

1. Wave Interaction, in which a section of the ionosphere is heated by pulses of a powerful disturbing wave, and effects are observed from reception of a second transmitted radio signal which has a path through the disturbed region. Electron density profiles are obtained either by finding a catalog profile consistent with the data, or by inverting a large system of integral equations.

2. Partial Reflection, in which the ratio of amplitudes of ordinary and extraordinary waves scattered from refractive index irregularities in the D region are taken as a measure of integrated absorption up to the altitude sampled. Electron density profiles are obtained from the derivative of this integrated absorption.

3. Incoherent Scatter Radar, in which radio waves are scattered from thermodynamic irregularities in refractive index, and the power, autocorrelation and polarization of the received signal are measured. Electron density and other quantities may be deduced from this data.

Electron density profiles from the D region during solar flares in 1968 have been published by Montbriand and Belrose (1972) using partial reflection (Figure 2.2) and Rowe et al. (1970), using wave interaction (Figure 2.3). The ion-chemical implications of these profiles are discussed by Mitra (1974). Improvements in the incoherent-scatter technique have produced reliable electron density profiles in the D region. Profiles for the flare event of January 5, 1981 are given by Mathews (1984) and shown in Figure 2.4.

A fourth method, not described by Mitra, is coherent scatter, the subject of this work. Miller et al. (1978) point out the existence of

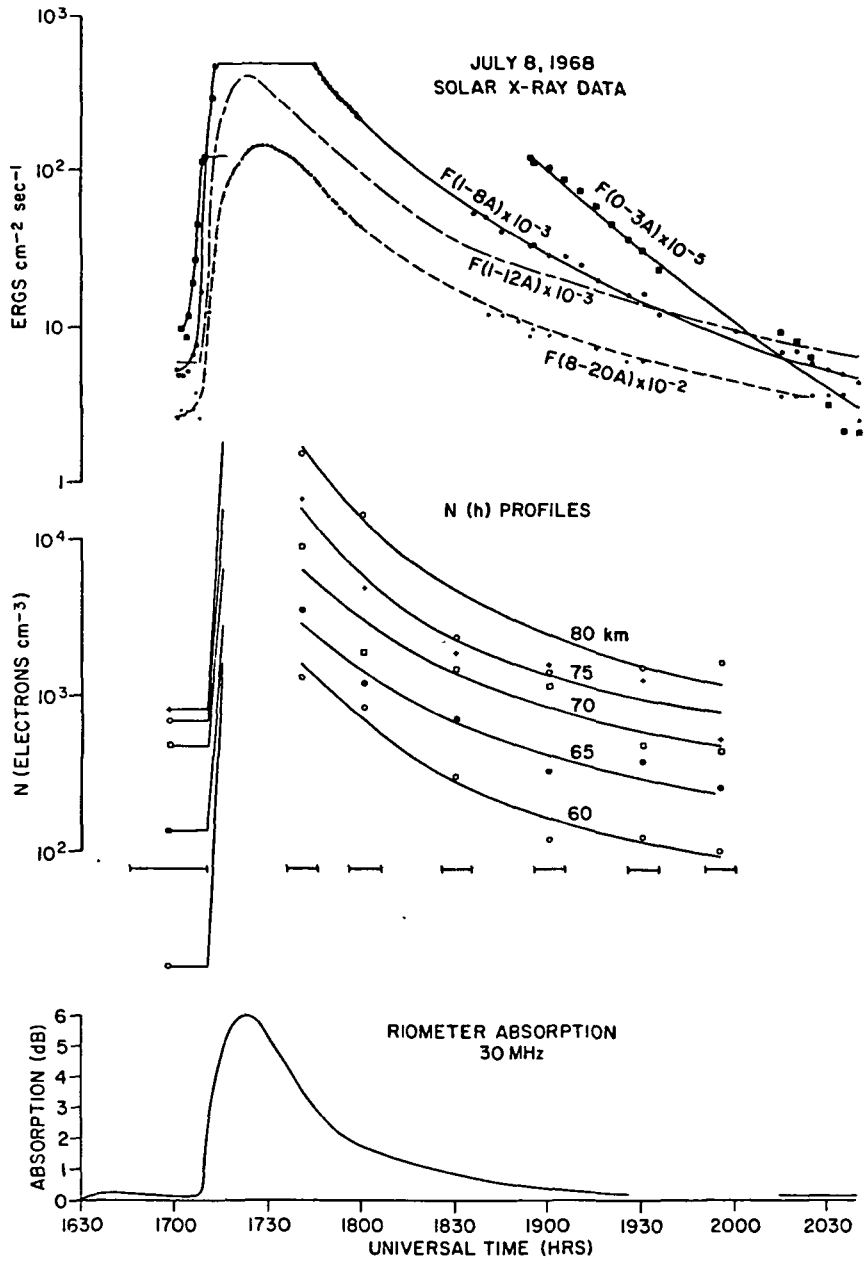

Figure 2.2 Flare event of July 8, 1969. Top: satellite X-ray flux, Middle: electron density profiles deduced from partial reflection experiment at Ottawa, Bottom: SCNA measurement (Montbriand and Belrose, 1970).

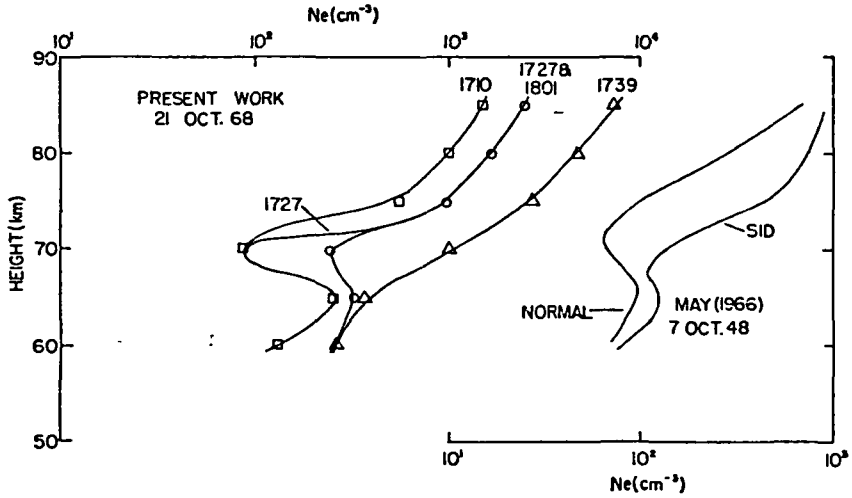

Figure 2.3 Left: Electron density vertical profiles for flare event of October 21, 1968 deduced from wave interaction experiment. Right: profiles deduced from event of October 7, 1942 by May (1968) from SID data (Rowe et al., 1970).

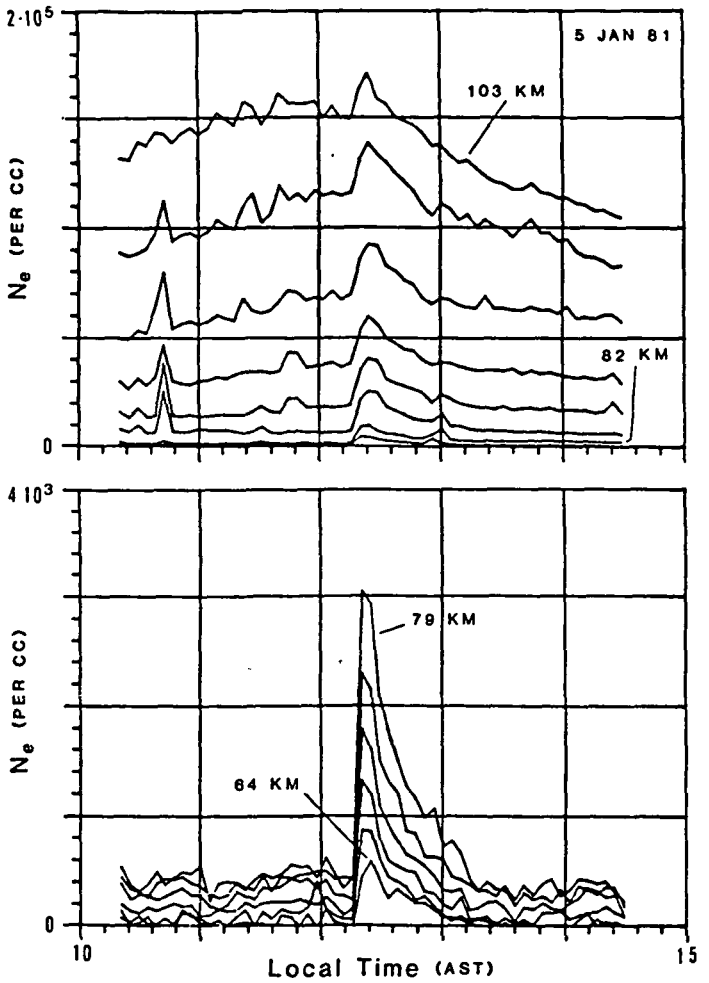

Figure 2.4 Electron density profiles for flare event of January 5, 1981 deduced from incoherent scatter experiment at Arecibo (Mathews, 1984).

additional scattered power allowing more complete velocity measurements for the mesosphere during the flare of April 11, 1978. An increase in coherent scatter coinciding with a flare event has also been reported by Rottger (1983). Figure 2.5 shows a contour plot of coherent scatter during the January 5, 1981 event, and clearly shows an enhancement in the scatter from several altitudes.

A description of the coherent-scatter technique is given in Chapter 4. Recent Urbana coherent-scatter radar observations of flare effects are presented in Chapter 5.

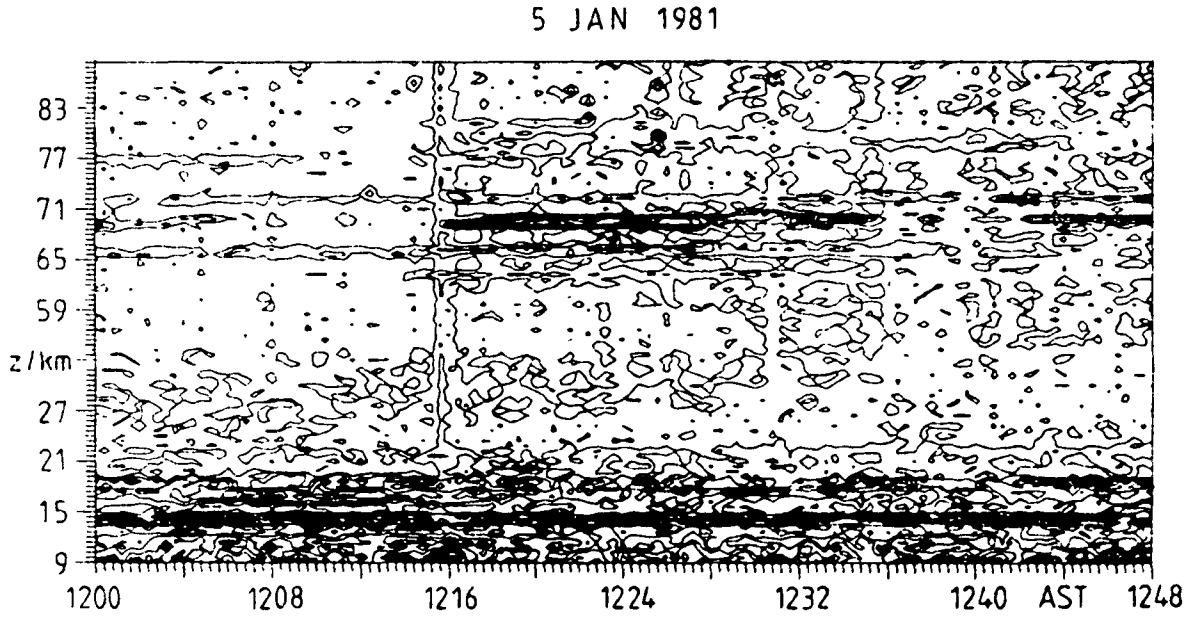

Figure 2.5 Contour plot of coherent scattered power during flare event of January 5, 1981 over Arecibo (Rottger, 1983).

3. THEORY OF D-REGION FLARE EFFECTS

3.1 The nonflare D region

The production of ion-electron pairs in the ionosphere is chiefly due to solar radiation, and at any altitude depends on the amount of radiation I at each wavelength λ reaching that point, the density of each ionizable species $[n_i]$, the photoionization cross section of each species at that wavelength σ_i, and the ionization efficiency η according to

$$q(\lambda) = \eta(\lambda)\sigma_i(\lambda)[n_i]I(\lambda) \tag{3.1}$$

(Hargreaves, 1979). According to Chapman theory, each of these wavelength contributions at altitude z may be calculated given the flux at the top of the atmosphere $I_\infty(\lambda)$, and the solar zenith angle χ,

$$q(\lambda,z,\chi) = \eta\sigma_i[n_i]I_\infty \exp(-\tau(\chi,z)) \tag{3.2}$$

where τ is the optical depth factor at that wavelength, given by

$$\tau(\chi,z) = [n_a]\, H\, \sigma_a \sec(\chi). \tag{3.3}$$

Here $[n_a]$ is the number density of one species which absorbs photons at the wavelength λ, H is the local scale height, and σ_a is the absorbtion cross section of the absorbing species. The factor $\sec(\chi)$ must be modified for zenith angles greater than about 70°. If more than one absorbing species is significant, τ is the sum of τs as defined above, over all such species. The actual value of the ion-pair production rate $q(z,\chi)$ is the sum of the above $q(\lambda,z,\chi)$ over all relevant wavelengths.

Other sources of ionization, such as galactic cosmic rays, may also be computed and their ion-pair production rates added to the above q under appropriate circumstances.

The significant sources of ionization in the D and lower E regions are shown in Figure 3.1 (Ratnasiri, 1975). In the D region below 85 km, the

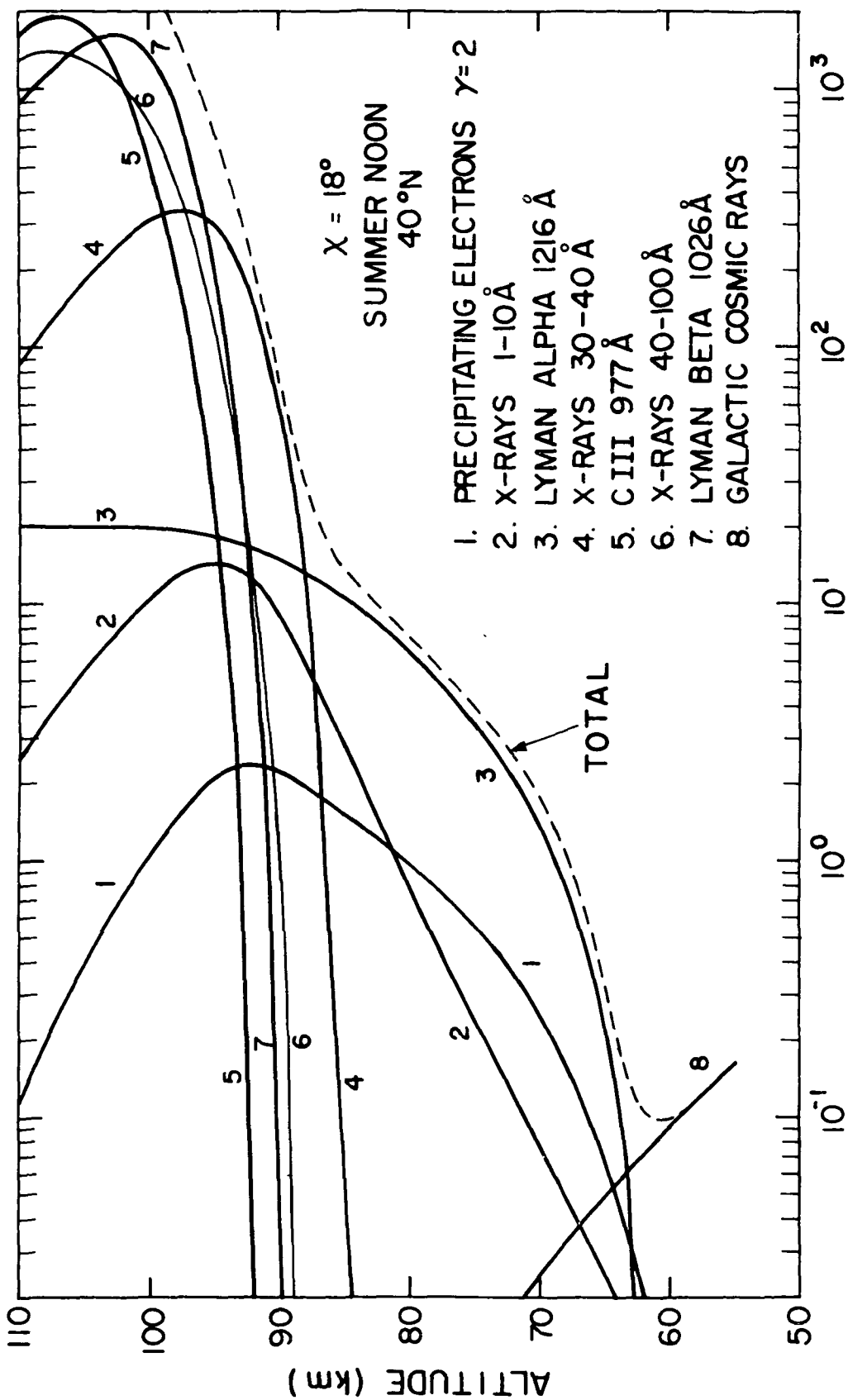

Figure 3.1 Sources of ionization in the D and lower E regions above the summer daytime midlatitudes (Ratnasiri, 1975).

chief source is the Lyman-α line of the solar spectrum, which at 121.6 nm is energetic enough to ionize only NO (Hargreaves, 1979). X-rays in the band 0.1-1 nm contribute a fraction of the total. In fact, this curve is based on X-ray data for July 24, 1968, near the maximum of the 11-year solar sunspot cycle. The contribution of these nonflare X-rays to D-region ionization may be more than a factor of one hundred less at solar sunspot minimum (Hargreaves, 1979).

The density of electrons may be deduced from the ion-pair production rate and electron loss reactions. The electron continuity equation for a motionless atmosphere is

$$dN_e/dt = q(t)-L(t) \tag{3.4}$$

where L is the rate of electron loss. For equilibrium, which may be assumed valid at least during most nonflare conditions, we may set the time derivative to zero, and thus

$$q(t) = L(t). \tag{3.5}$$

The D region may be subdivided into several different layers, each with a characteristic set of dominant ions and reaction schemes, and therefore different electron loss rates. In the region from 70 to 90 km, the loss reaction type is dissociative recombination, of the form

$$AX^+ + e \text{ --> } A + X \tag{3.6}$$

(Hargreaves, 1979). If the species AX^+ is the dominant ion, and if it is produced quickly compared to this loss reaction, we may derive a loss rate quadratic with N_e, as follows. The loss rate implied by reaction above is

$$L = \alpha_D[AX^+]N_e \tag{3.7}$$

where α_D is usually a known reaction rate constant. Charge neutrality implies

$$[AX^+] = N_e. \tag{3.8}$$

Thus the loss rate is

$$L = \alpha_D N_e^2. \tag{3.9}$$

Usually, several ionic species contribute to the loss of electrons via dissociative recombination. In this case, the α_D for each species may be combined in a weighted average:

$$\alpha_D = \sum [AX^+]\alpha_{D(AX)} / \sum [AX^+]. \tag{3.10}$$

The loss rate remains quadratic in N_e, since charge neutrality now says

$$\sum [AX^+] = N_e \tag{3.11}$$

and thus

$$\begin{aligned} L &= \sum \alpha_{D(AX)} [AX^+] N_e \qquad (3.12) \\ &= N_e (\sum \alpha_{D(AX)} [AX^+]) (\sum [AX^+]) / \sum [AX^+] \\ &= N_e^2 \sum \alpha_{D(AX)} [AX^+] / \sum [AX^+] = \alpha_D N_e^2. \end{aligned}$$

In the region from about 82 to 90 km, the dominant ions are NO^+ and O_2^+. These have similar values of α_D, of about 2×10^{-6} $cm^3 s^{-1}$ (Mitra, 1974). There is a transition region at about 82 km (the altitude varies with temperature), with the composition of the region below dominated by hydrated proton ions, $H^+(H_2O)_n$, for n=1,2,3,.... The distribution of each hydration order and the maximum size are unknown; orders up to 5 have been detected by rocket-borne mass spectrometers (Narcisi et al., 1972), but higher order hydrates are believed to fragment in the capture and detection process. However, it is not necessary to know the distribution of hydrates among the possible orders; most of these hydrates have a much greater recombination rate with electrons than the ordinary diatomic ions, on the order of 10^{-5} $cm^3 s^{-1}$. The electron loss process is still dissociative recombination, and the rate is

$$L = \alpha_D N_e^2 \tag{3.13}$$

but now with a much larger α_D. This accounts for a frequently observed

feature of electron density profiles (see Figure 3.2) in the range 82–85 km. There is a particularly steep electron density gradient in that range, because hydrated cluster ions below the ledge consume electrons more rapidly than the diatomic ions above it. Turbulent mixing acting on this gradient accounts for some of the regions of high scattered power observed by the MST radar technique.

The region below 70 km contains significant negative ions during the day, including O_2^- and $NO_3^-(H_2O)_n$. Here the reaction scheme is complicated, and many of the reaction rates are unknown. However, a simple model may be discussed. In this region, dissociative recombination, ion-ion recombination, electron attachment, and detachment all occur, with rates α_D, α_i, β, and γ, respectively. These are average coefficients for all such reactions of positive ions, negative ions, and electrons, derived in the fashion of α_D above. Each is a weighted average of the coefficients for the individual reactions of the corresponding type, weighted by the proportions of the ions involved. In this way we may speak of average continuity equations for ions and electrons in terms of total ion densities and these coefficients. Charge neutrality may be assumed, thus

$$N^+ = N^- + N_e \tag{3.14}$$

where N^+ is the total positive ion concentration, and N^- is the total negative ion concentration. Defining λ as the ratio of negative ions to electrons, we follow Mitra (1974) in using the following electron continuity equation:

$$(1+\lambda)dN_e/dt + N_e d\lambda/dt = q - (\lambda\alpha_i+\alpha_D)(1+\lambda)N_e^2 \tag{3.15}$$

When equilibrium may be assumed, the left-hand side of this reduces to zero. Note that this requires equilibrium in both N_e and λ. When this is the case we may define an effective recombination coefficient α_{eff}:

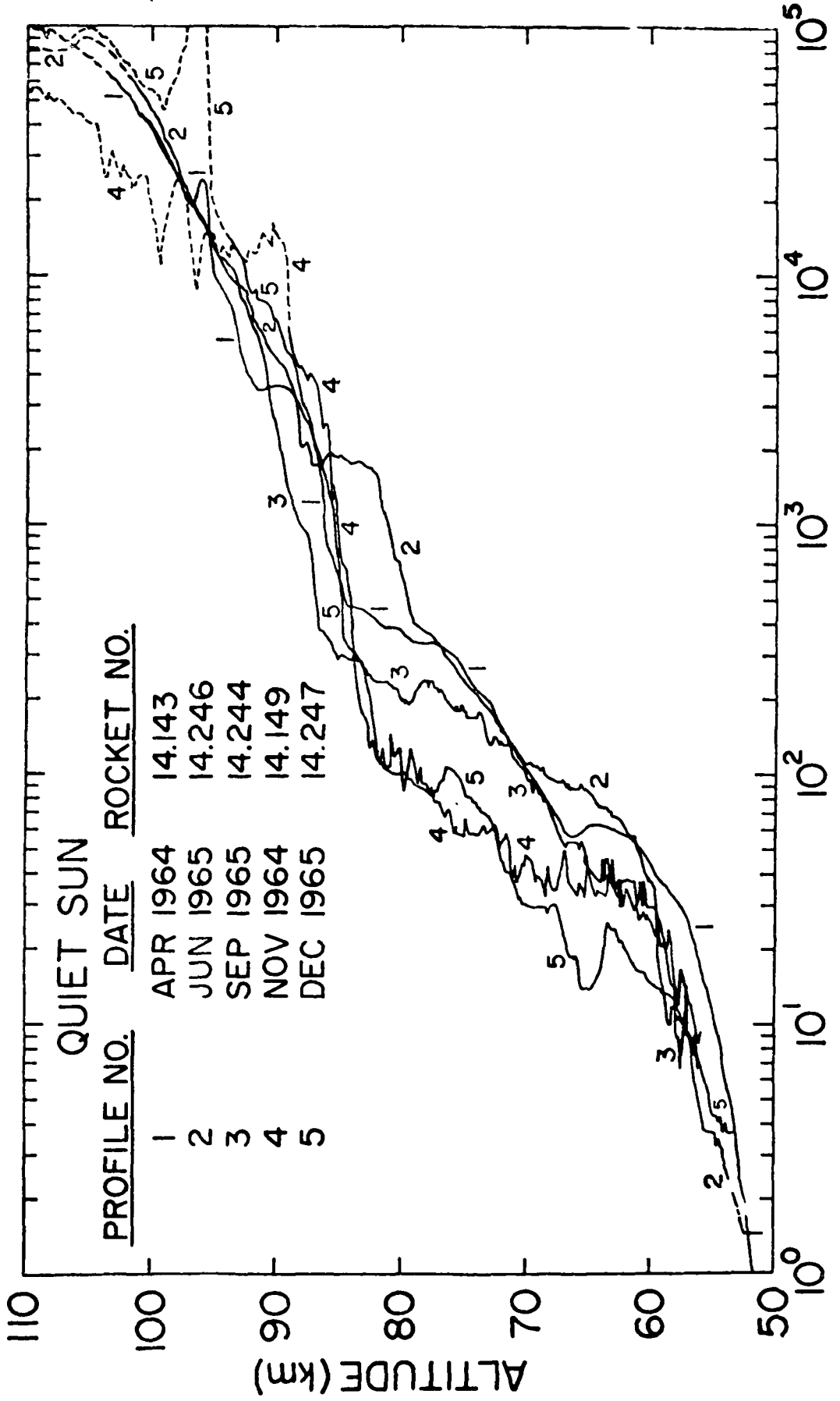

Figure 3.2 Electron concentration profiles in the lower ionosphere for quiet sun conditions (Mechtly et al., 1972).

$$\alpha_{eff}=(\lambda\alpha_i+\alpha_D)(1+\lambda) \tag{3.16}$$

such that

$$q = \alpha_{eff}N_e^2 \tag{3.17}$$

with α_{eff} constant when α_D, λ and α_i are constant. We may be able to determine if q and N_e are quadratically related, even if we cannot predict the constant of proportionality, α_{eff}.

3.2 Solar flare disturbances in the D region

A solar flare is an explosive release of energy from a localized portion of the solar atmosphere. Energies can be in excess of 10^{32} ergs, and emissions take the form of high-energy protons, plasma, and electromagnetic radiation, in frequency bands ranging from X-rays to radio emissions (Hargreaves, 1979).

The immediate observable D-region effect is an increase in the production of electrons due to photoionization by enhanced emission in those wavelengths energetic enough to ionize the atmosphere, and not absorbed in the layers above the D region, particularly X-rays and the hydrogen Lyman-α line. The radiation from the sun is currently monitored continuously by instruments on satellites in only a few spectral ranges, and typically only by broad-band detectors. Two of the difficulties in analyzing the problem are the variability of the spectrum of the solar disturbance as a function of time, and the meager amount of data availible on spectral shape. However, it is shown below that a simple model of the spectrum as a function of time may be constructed from data from two broad-band X-ray detectors. This spectral model is combined with atmospheric models to predict significant features of D-region effects.

The significant contributors to D-region ionization are solar Lyman-α (121.6 nm), solar X-rays in the range 0-1 nm, galactic cosmic rays below

about 63 km, and possibly the solar Carbon VI line at 3.37 nm in the range 85-90 km. Lyman-α radiation is dominant over most of the range 60-90 km under nonflare conditions. During a flare, Lyman-α radiation increases from the small area of the solar disk affected, but this increase is relatively small compared to the huge normal solar Lyman-α emission. For example, broad-band sensors on the Nimbus 3 satellite observed quite a large flare in 1969, yet indicated a Lyman-α flux increase of only about 16% (Heath, 1973). By contrast, observations of solar X-rays from GOES satellites show huge increases during flares (see Figure 3.3). The 0-0.8 nm flux increases by factors of eight for smaller flares, and well over a hundred for large flares. Since nonflare X-ray flux in this band near the sunspot cycle maximum accounts for at least 1/8 of the total ionization production between 62 and 85 km (Ratnasiri, 1975), the increased ionization due to X-rays during a moderate to large flare dominates the increase in ionization due to enhanced Lyman-α .

Other sources of ionization can be either easily incorporated or else neglected. Galactic cosmic ray effects are assumed not to change during a solar flare. The Carbon VI line emission certainly changes, but has not been accurately measured during a flare. However, Ratnasiri (1975), choosing a value of 7×10^{-3} erg cm^{-2} s^{-1}, which is a factor of 3.5 greater than the active but nonflare day value of the line measured by Manson (1972) for the 3.37 nm line, indicates the contribution to electron production below 85 km is well under a factor of 500 below that of Lyman-α (Figure 3.1). Also, by the Chapman Theory, the contribution from a wavelength decreases as $\exp(-e^{-(z_0-z)/H})$, where z_0 is the altitude of unit optical depth. As this altitude is about 95 km for 3.37 nm radiation, it seems unlikely that even a flare enhancement of this line would contribute significantly to

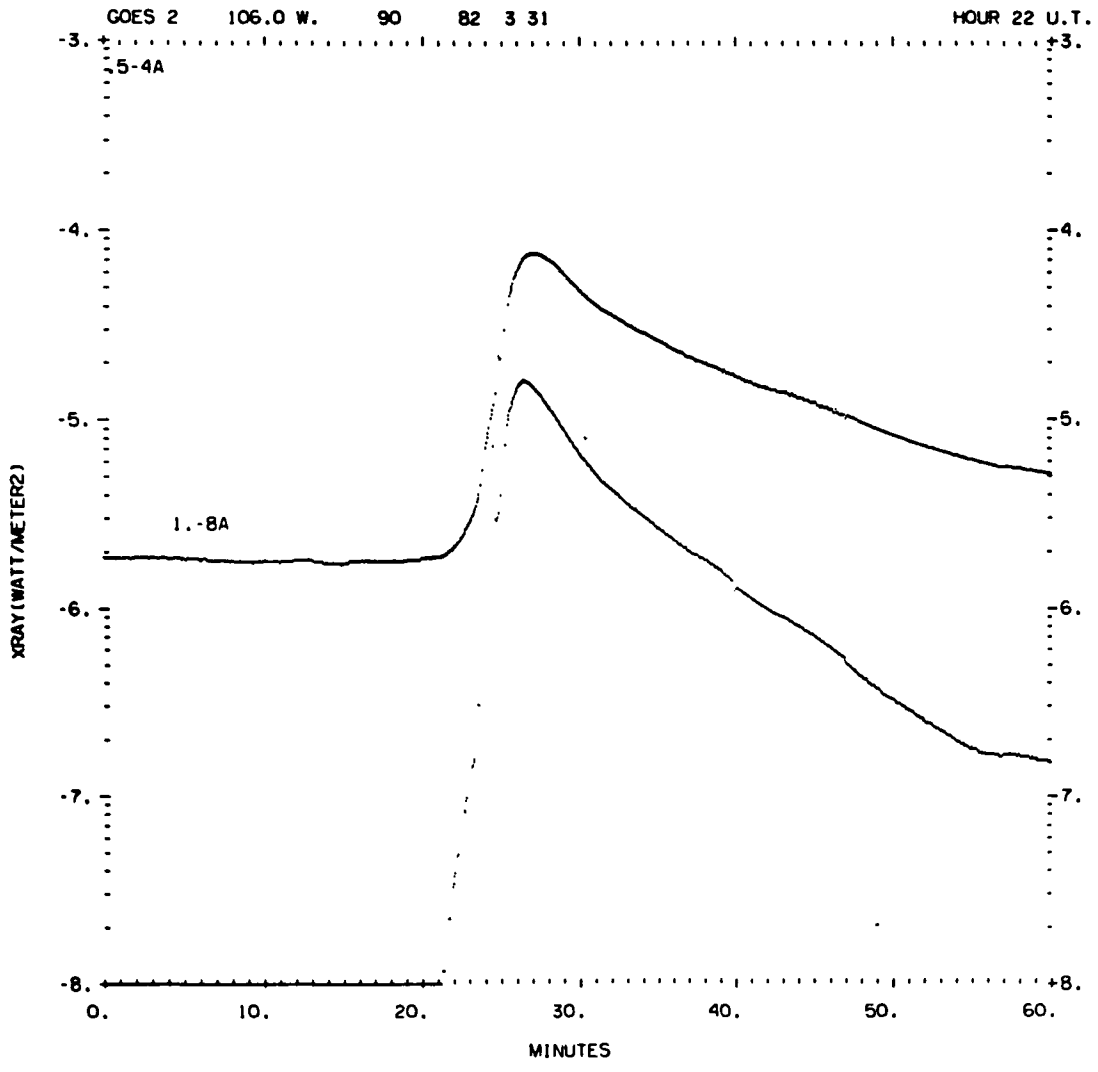

Figure 3.3 X-ray flux in 0.1-0.8 nm and 0.05-0.4 nm bands for flare event of March 31, 1982, measured by GOES 2 satellite (courtesy of the National Geophysical Data Center).

D-region ionization production, especially below about 85 km.

We conclude that we may model the atmospheric electron production function q at a given altitude, and a brief period of time (on the order of an hour) as a constant q_0 due to Lyman-α radiation and galactic cosmic rays, plus a variable $q_x(t)$ due to 0-0.8 nm flare X-rays. We further develop this model below.

The satellite-borne detectors of X-ray energy detect only relatively broad-band integrated fluxes. Fortunately, in the X-ray band of interest, most of the energy is believed to reside in the continuum rather than in discrete lines. Thus, a modest attempt at modeling the continuum spectrum from the X-ray data is adequate for predicting ionization rates due to the flare in the atmospheric regions of interest (Donnelly, 1977).

Although the sun normally has a spectrum near the visible wavelengths similar to a black body at 5900 K, the existing (somewhat meager) high-resolution X-ray spectral data do not match a black-body curve during flares (Donnelly, 1977). Theories of bremsstrahlung and radiative recombination processes occurring in a high-temperature ($T > 10^6$ K), low density plasma have been applied to the solar corona by Tucker and Koren (1971). They arrived at a likely exponential model. However, to gain an adequate match to existing data, two or more such curves must be linearly combined, which indicates regions of the corona at different distinct temperatures (Deshpande and Mitra, 1972). A simpler approach is to use a semiempirical curve which seems to have a rough fit to the few high resolution spectra. A spectrum of the power law form

$$I(\lambda) = A(\lambda)^B, \tag{3,18}$$

has been adequate for past studies (Rowe 1970, Ratnasiri 1975), and is employed in this work. Mitra (1974) asserts such a form corresponds to a

temperature gradient in the corona; such a condition is likely during a flare.

The wavelength response of the ion chambers used in the SMS/GOES satellites is shown in Figure 3.4 (Donnelly, 1977). These response curves allow us to determine a unique value for A and B for each instant of recorded data, according to the formulas below. We may conceptually form the integrals of the ion chamber response functions with the power law spectrum:

$$D1 = \int G(\lambda) A(\lambda)^B \, d\lambda / \overline{G} \tag{3.19}$$

where $\overline{G}$ is a normalizing constant for the chamber response. Dividing the response of the 0.1-0.8 nm chamber (D2) by the response of the 0.05-0.4 nm chamber (D1) yields a ratio which is a function of B:

$$R = D2/D1 = \int (G2(\lambda)/\overline{G2})(\lambda)^B \, d\lambda / \int (G1(\lambda)/\overline{G1})(\lambda)^B \, d\lambda. \tag{3.20}$$

Evaluating this function over a range of values of B yields, implicitly, the power index B as a function of the ratio R of the observed detector responses (Figure 3.5). Similarly, we can evaluate A as:

$$A = D2 / \int (G2(\lambda)/\overline{G2})(\lambda)^B \, d\lambda \tag{3.21}$$

yielding a complete spectral model. Thus, at any time instant, D1 and D2 can be taken directly from the GOES data, and these values used in the above formulas to compute A and B, which are used in the power law formula for $I(\lambda)$. Typical histories of the quantities A and B are shown in Figure 3.6.

3.3 D-region ionization by X-rays

The photoionization rate for a single wavelength, λ, has been derived above to be

$$q_x(\lambda, z, \chi) = I_\infty(\lambda) \sigma_i [m] \exp(-\sigma_a [m] H \sec(\chi)) \tag{3.22}$$

where χ is the solar zenith angle, [m] is the total number density of air (implicitly a function of altitude), H as the scale height (also implicitly a function of altitude, although slowly varying), σ_a and σ_i are the

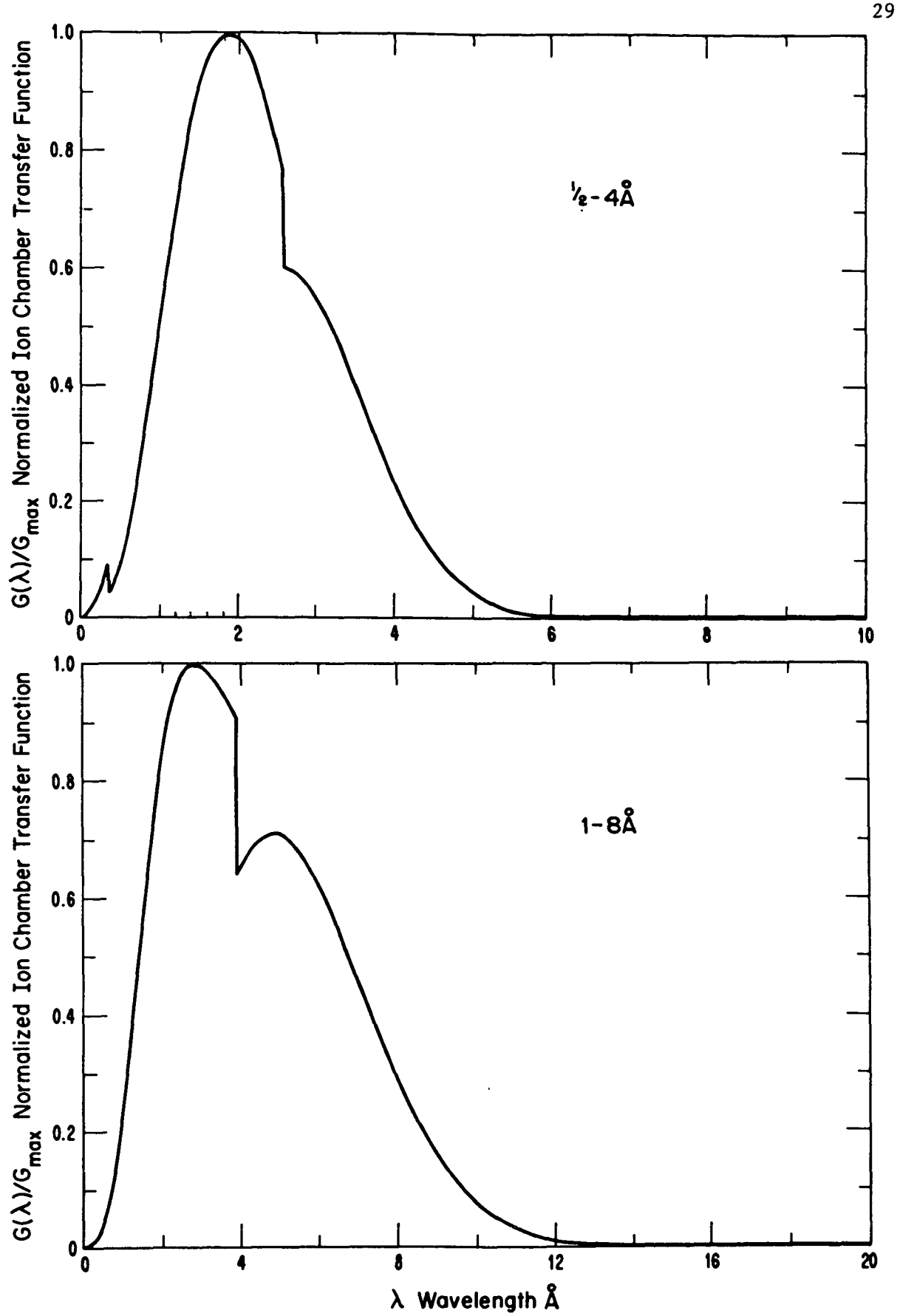

Figure 3.4 Relative wavelength dependence of SMS-GOES X-ray detectors (Donnelly, 1977).

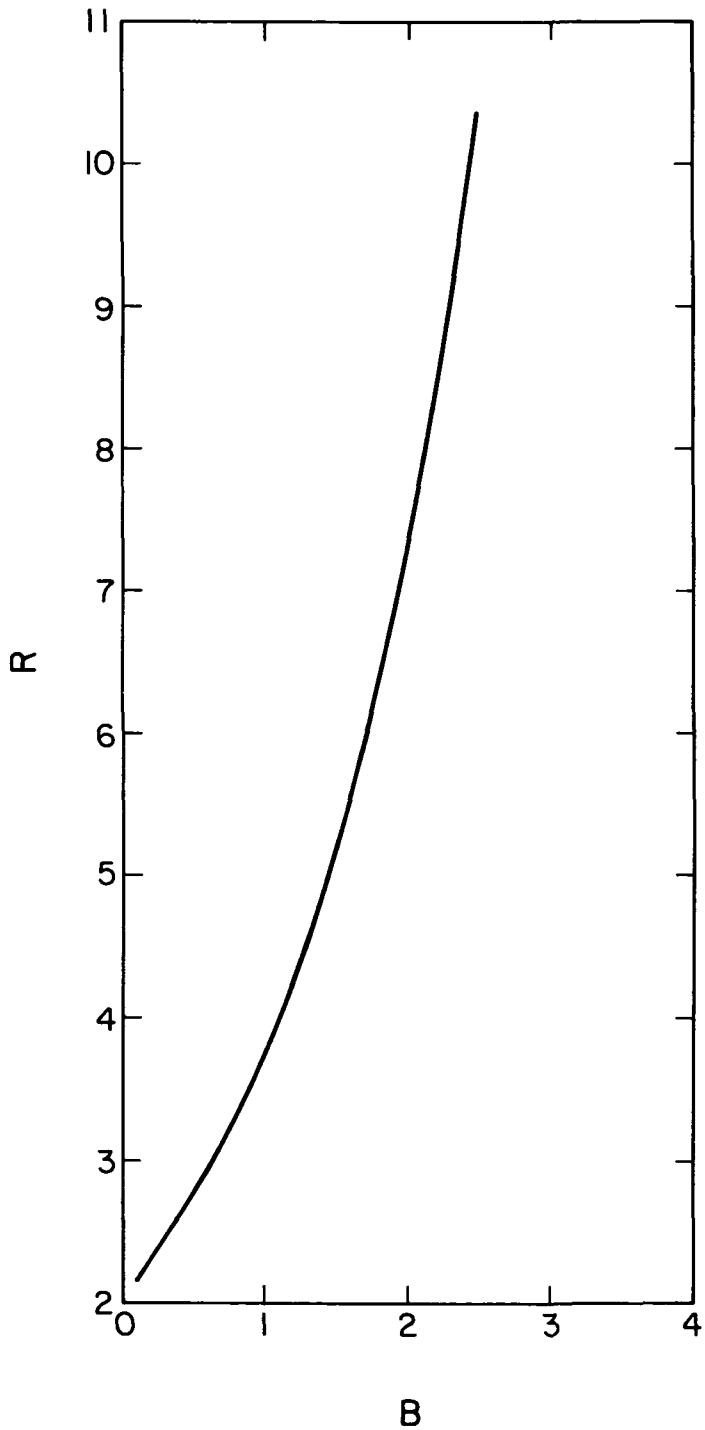

Figure 3.5 Power law index B as function of ratio R of X-ray detector outputs.

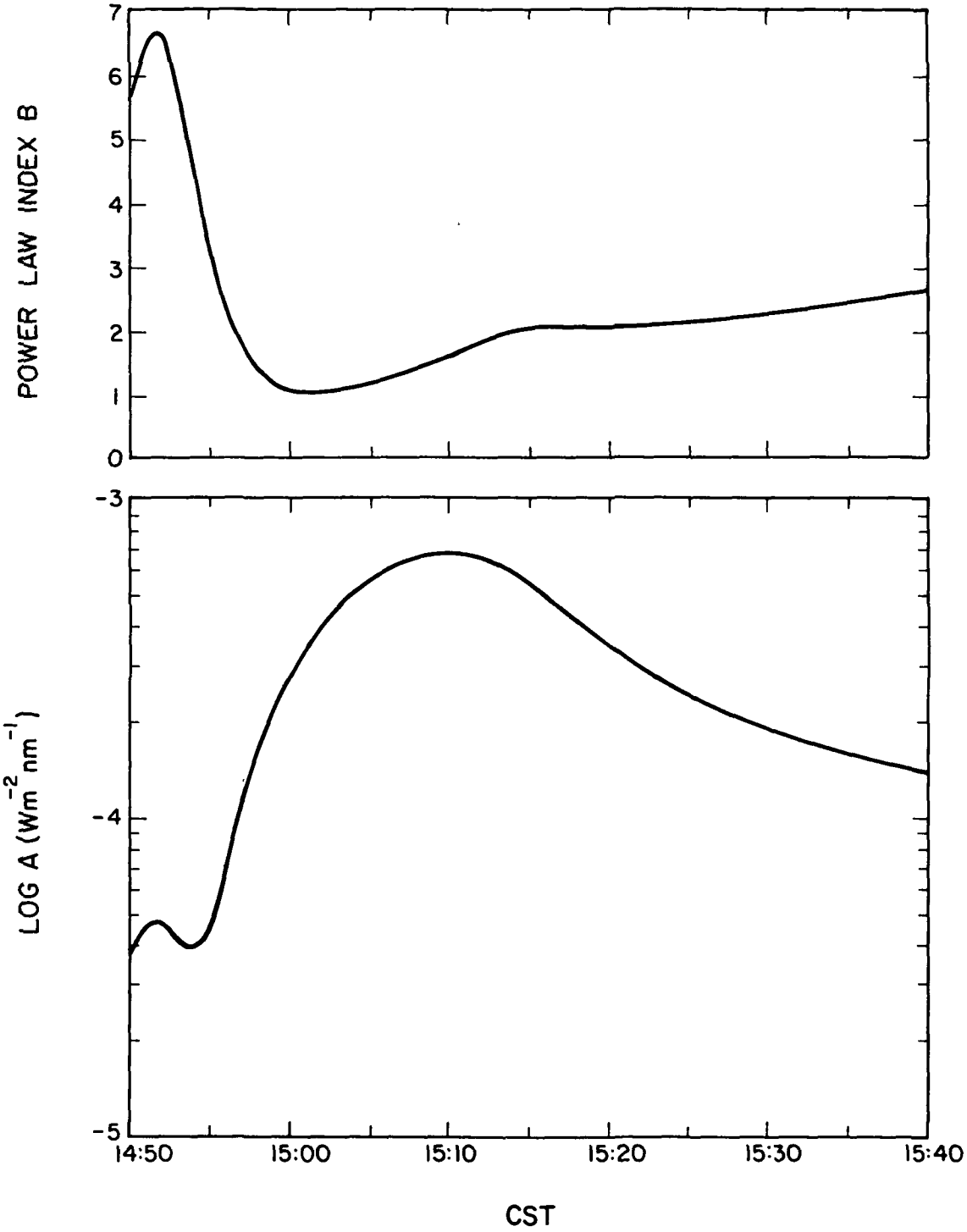

Figure 3.6 Time curves of A (coefficient) and B (power law index) during flare event of May 21, 1980.

average absorption and ionization cross sections for air (implicitly a function of λ), and $I_\infty(\lambda)$ is the photon flux at the top of the atmosphere. It is related to the energy flux obtained by satellite measurements by

$$I(\text{photons m}^{-2}\ \text{s}^{-1}) = I(\text{w m}^{-2})\lambda/(hc) \tag{3.23}$$

where care is taken to insure λ (wavelength), h (Planck's constant) and c (speed of light) are expressed in compatible units.

From Figure 3.7 (Banks and Kockarts, 1973) we see that σ_a can be adequately represented in the range 0.05 to 2.2 nm by the empirical formula

$$\sigma_a = C(\lambda)^D \tag{3.24}$$

where $C = 9.5\text{x}10^{-20}$ (cm^2), $D = 2.8$, and λ is given in nm. Further, σ_i is related to σ_a by the ionization efficiency η:

$$\sigma_i = \eta\sigma_a \tag{3.25}$$

where η is greater than unity due to the production of ionizing photoelectrons from the initial photoionization. The energy of the original photon is used up at a rate of 35 eV per ion pair produced (Banks and Kockarts, 1973), so

$$\eta = 1.23\text{x}10^3 / (35 \text{ x } \lambda) = 35.4/\lambda \tag{3.26}$$

The actual ionization rate due to X-rays is given by the integral of $q_x(\lambda,h)$ over all wavelengths. This integral is of the form

$$q_x(z) = a \int \lambda^b W(\lambda) \exp(-c\,\lambda^d)\, d\lambda \tag{3.27}$$

where a, b, c and d and are constants at a given altitude, given by the above derivation to be

$$a = A \text{ x } 35.4 \text{ x } C \text{ x } [m] \text{ x } 10^{-4} \text{ x } 10^{-9} / (hc)$$

$$= 1.69\text{x}10^{-6} \text{ x } A[m]$$

$$b = B + D = B + 2.8$$

$$c = C \text{ x } [m] \text{ x } H \text{ x } 10^{-4} \text{ x } \sec(\chi) = 9.5\text{x}10^{-24} \text{ x } [m]H\sec(\chi)$$

$$d = D = 2.8$$

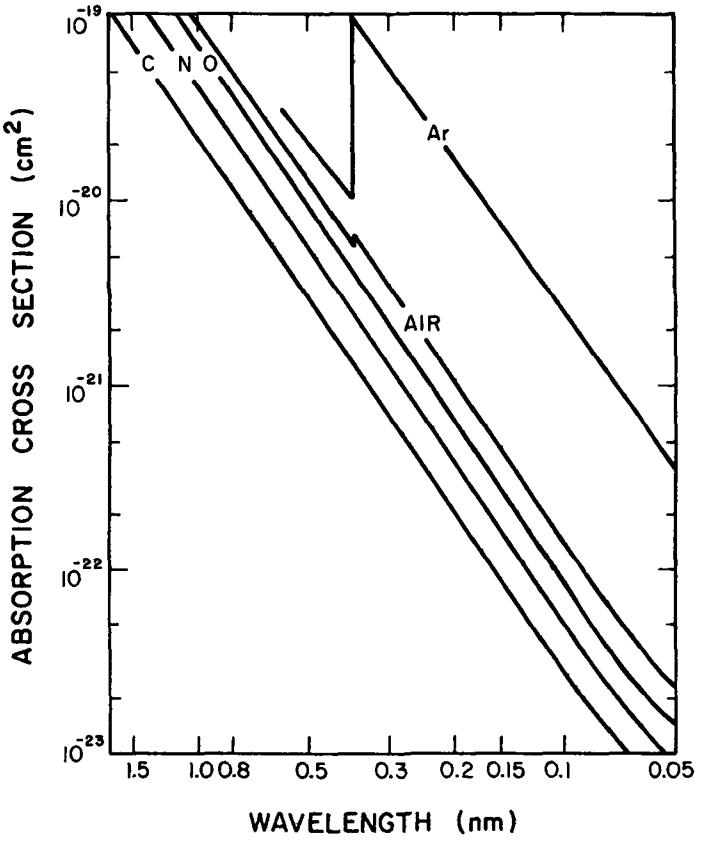

Figure 3.7 Absorption cross sections of air (average) and the principal atmospheric constituents between .05 and 1.5 nm (Banks and Kockarts, 1973).

(units are mks, except for the variable λ, which is retained in nm so it can easily be integrated out below). $W(\lambda)$ is a weighting function, equal to unity in the range 0.05 to 2.33 nm, but momentarily unspecified elsewhere; W expresses the deviations from the linear and power laws in the model which occur outside the bounds of the model. Solving first for W unity everywhere, we obtain

$$q_x = c^{-(b+1)/d} \Gamma((b+1)/d)\ a/d \qquad (3.28)$$

(Gradshteyn and Ryzhik, 1965, integral 3.478) where Γ is the gamma function. In the range 0 to 0.05 nm, the power-law form of the flux for the range of power indices obtained from flare events considered in this work are so small that deviations from the model in this region do not affect the integral appreciably above 60 km. Further, deviations from the model at long wavelengths do not affect ionization at altitudes below about 100 km. Thus, the formula above can be taken as valid in the range 60-90 km without significant degredation of the estimate of q_x. Typical profiles of this model q_x for quiet conditions and flare maximum are shown in Figure 3.8.

3.4 Electron loss reactions

The change in concentration of electrons at a given altitude due to a solar flare depends on both changes in the production of ion pairs and possibly changes in the electron loss processes. If the loss reactions are much faster than the changes in production rate during a flare, a steady state may be assumed at each instant during a flare, in which case

$$q(t) = L(t) \qquad (3.29)$$

If we can obtain an explicit form for L in terms of N_e, we can predict N_e from the estimate of q derived from the solar spectral model derived above. We showed above that the most simple model predicts

$$q \propto N_e^2, \qquad (3.30)$$

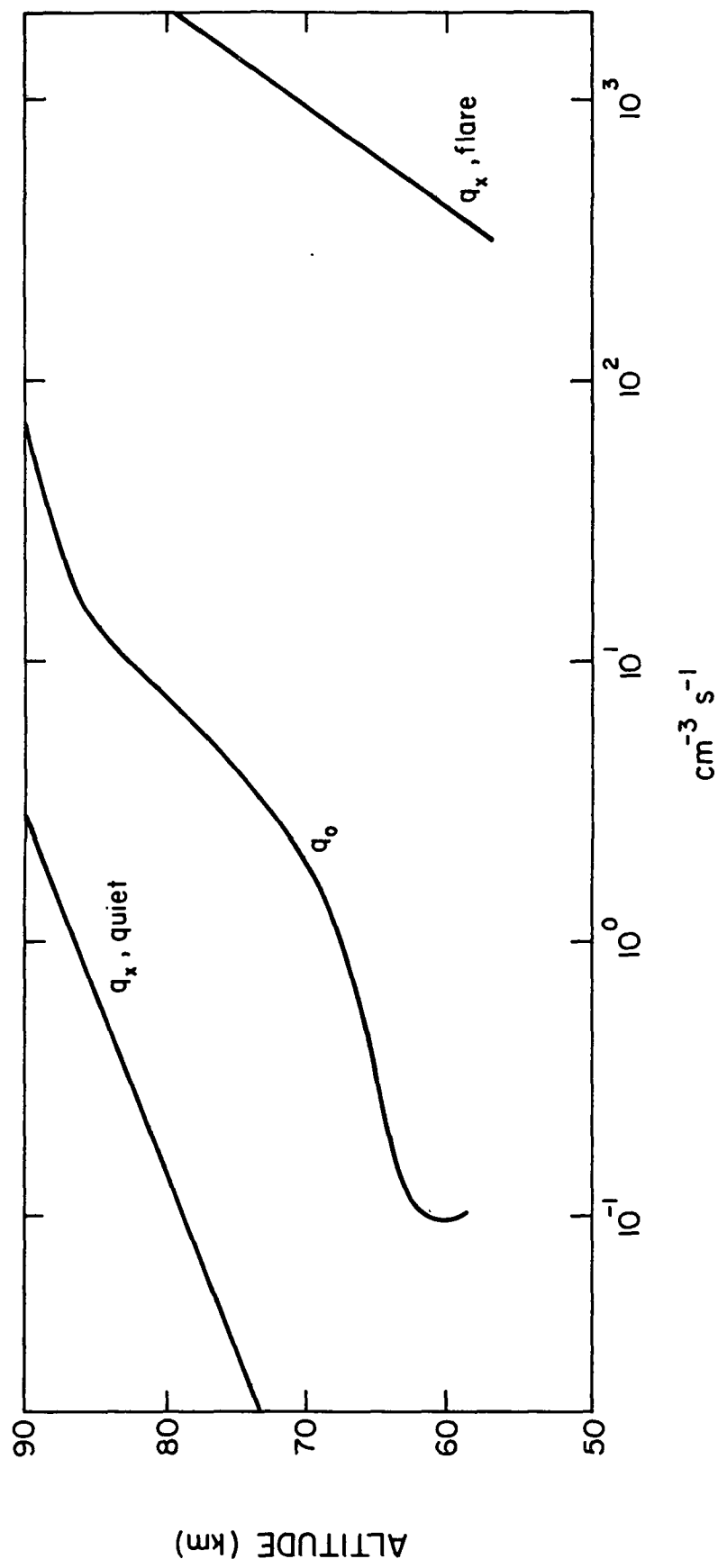

Figure 3.8 The electron production functions in the D region due to X-rays under nonflare conditions (q_x, quiet), total for quiet conditions (q_o, from Figure 3.1) and due to a large flare X-ray enhancement (q_x, flare).

a quadratic relation. We present flare-time chemical models below, which at some altitudes predict roughly

$$q \propto N_e, \tag{3.31}$$

a linear law. Since the Urbana radar gives an estimate of $\Delta N_e/N_e$ at each time and altitude, while GOES X-ray data yield a measure of the increase in $I(\lambda)$ and therefore $q(z,t)$, these models may be empirically distinguished. This is done in Chapter 5.

Although the above theory predicts a quadratic law in this region, several observations of flares before this study have indicated that N_e during a flare increases faster than the square root of q (Mitra, 1974). Although we may continue to represent the relationship as

$$q = \alpha_{eff} N_e^2 \tag{3.32}$$

α_{eff} may be a function of time throughout the flare.

A simple semiempirical model was developed by Mitra (1974) to account for such effects. This scheme is shown in Figure 3.9. In the region near 80 km, this model accounts for a change in α by showing α_D to be sensitive to the type of radiation producing the ions. Nonflare ion production in this region is the photoionization of NO by Lyman-α; the resulting NO^+ ions cluster rapidly with water vapor, finally switching with an H^+ ion to form the common hydrates. Additional production due to a flare ionizes all species, and therefore predominantly produces N_2^+ and O_2^+. The molecular nitrogen ion disappears almost immediately due to a very fast switching reaction which exchanges an electron with O_2, producing yet more O_2^+. This ion also begins a chain of reactions via O_4^+, which lead to hydrated protons, but which can also regress back to simple ions rather than forming hydrates. The rate of production of hydrates from O_2^+ depends on the ratio $[H_2O]/[O]$. Simulations by Mitra show a decrease in proportion of hydrates,

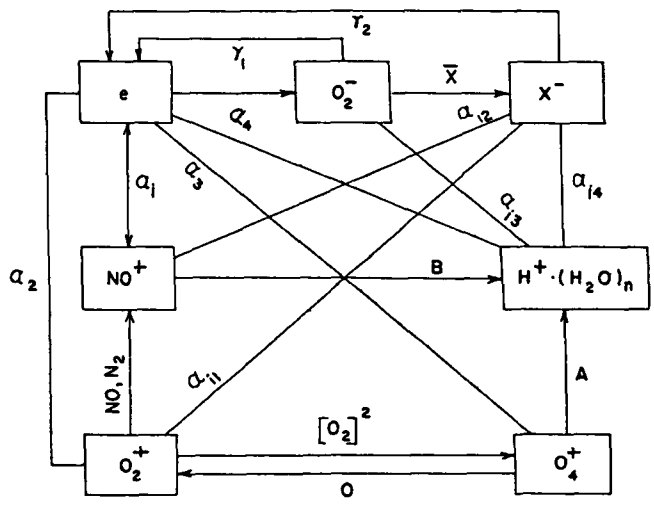

Figure 3.9 Simplified ion chemical model for the D region. (Mitra, 1974).

and therefore a decrease in α_{eff} with increasing q over the ranges $10^8 < [H_2O] < 10^{10}$ cm^{-3} and $10^9 < [O] < 10^{11}$ cm^{-3}, at 80 km. His model (Figure 3.10) predicts a rough inverse proportionality of α with N_e for all these values of [O] and $[H_2O]$, yielding

$$q = \alpha_{eff}(N_e)N_e^2 = \beta N_e, \tag{3.33}$$

a linear law. Insight into the cause of this may be gained by recalling that α_D is defined to be a weighted average,

$$\alpha_D = (\alpha_D(AX^+)[AX^+] + \alpha_D(HP)[HP]) \; / \; ([AX^+]+[HP^+]) \tag{3.34}$$

where AX^+ represents the diatomic ions, and HP^+ represents the hydrated proton cluster ions. The reduction in α_D with increasing q is due to a reduction in the proportion of hydrated ions, shifting the weighted average α_D gradually toward $\alpha_D(AX^+)$. This is in turn due to the substitution of O_2^+ for NO^+ as the dominant cluster precursor, implying a slower reaction path to hydrated ions.

This model also predicts that the proportion of hydrated ions will decline to nearly zero for the largest flares, resulting in a value of α_{eff} which is nearly constant during the most intense part of the flare. This implies a brief regime of quadratic behavior, but with α_{eff} at the (lower) diatomic ion level (Mitra, 1974).

In the region where negative ions become significant, below about 70 km, the reactions leading to a changed α_D at 80 km no longer operate. The above model showed only a few percent change in the proportion of hydrated clusters. However, we now must deal with the more complicated expression for α_{eff}:

$$\alpha_{eff}=(1+\lambda)(\alpha_D+\lambda\alpha_i). \tag{3.35}$$

λ may or may not change during a flare; if not, we recover a quadratic relation as before:

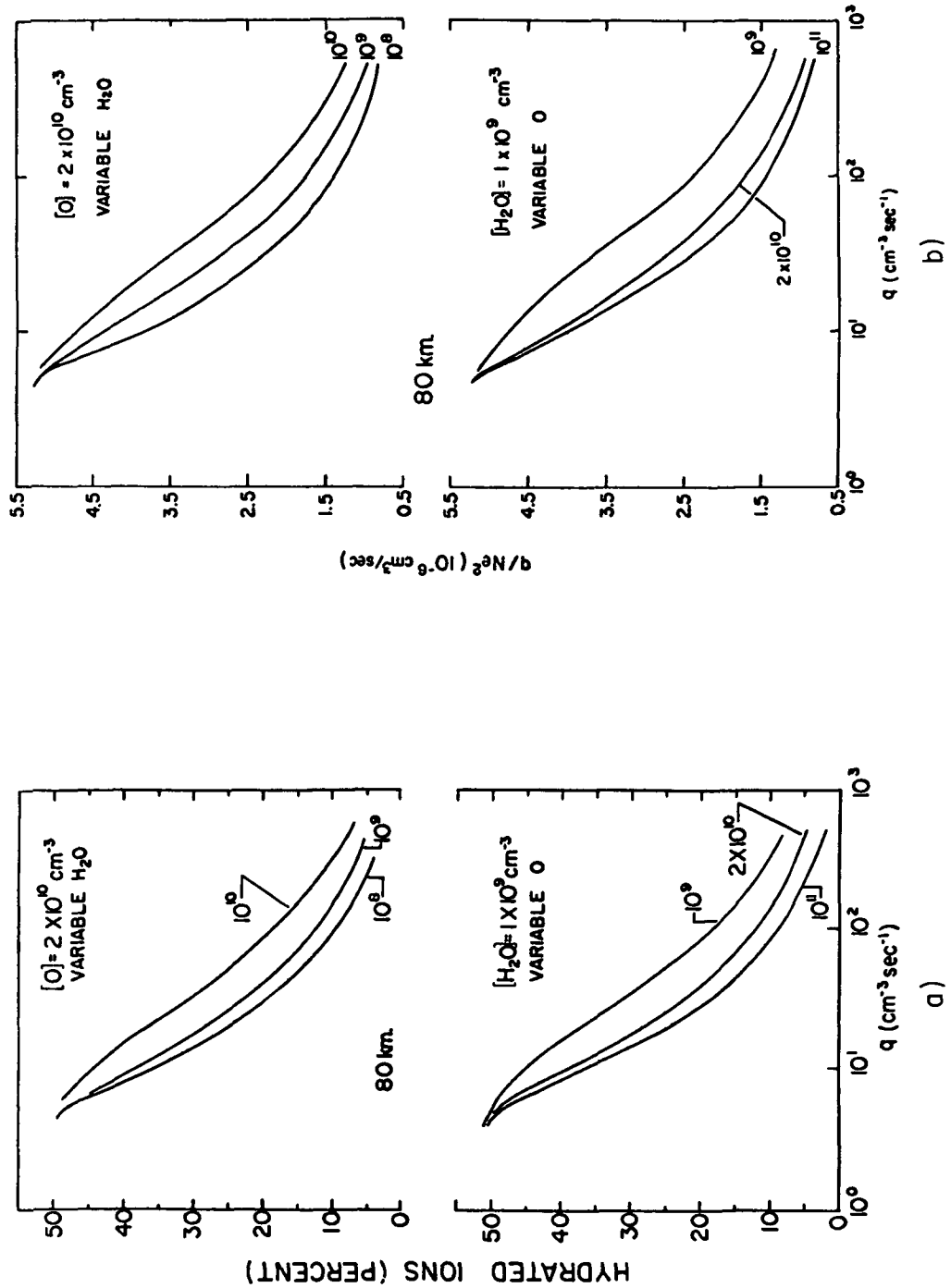

Figure 3.10. Percentage of water cluster ions and ratio q/N_e^2 calculated from chemical scheme of Figure 3.9 as function of q (Mitra, 1974).

$$q = \alpha_{eff} N_e^2 \tag{3.36}$$

Mitra also suggests the possibility of the relation

$$q = (\beta - \gamma N^-/N_e + \alpha_D N^+) N_e = B' N_e \tag{3.37}$$

which could lead to a nearly linear law if the bracket term happens to be about constant during an increase in q and N_e. Any data showing a linear law below 70 km probably are accounted for by this, as Mitra's models demonstrate negligible reduction in hydrate proportion as radiation is increased in this region. Models by Thomas et al. (1973) show a reduction in α_{eff} for increased radiation in this region, but also a significant lagging of the ionization profile behind the electron production function, on the order of 14 minutes. This suggests the possibility of a roughly linear law in the negative ion region, as well as deviation from the equilibrium assumption. If data show no such delay, it is unclear whether a linear law must hold; it appears quite possible that equilibrium flare effects may still produce a constant α_{eff}, and thus a quadratic law. Empirical evidence for a quadratic law in this altitude range will be discussed in Chapter 5.

4. OBSERVING D-REGION FLARE EFFECTS WITH MST RADAR

4.1 The Urbana MST radar system

The mode of electromagnetic scatter from the atmosphere which arises from fluctuations in the index of refractivity due to turbulence is termed "coherent scatter," in contrast with incoherent or Thomson scatter, which arises from refractive index fluctuations due to thermodynamic molecular motions. Coherent scatter has been actively investigated since the early 1970s. In the stratosphere and troposphere, the fluctuations in refractive index are directly due to turbulent mixing of clear air density, while in the mesosphere the turbulent air produces electron density fluctuations and therefore refractive index fluctuations. A radar system designed to detect such scatter from the mesosphere, stratosphere and troposphere is termed an "MST radar."

The Urbana MST radar has been collecting reliable data since 1978 (Miller et al., 1978). The system is monostatic, with a 1008 dipole array antenna. The transmitter operates at a frequency of 40.92 MHz. The system parameters during the time period discussed in this study are: peak pulse output power of about 1 MW, pulse width of 20 μs, and pulse repetition frequency 400 Hz. The received scatter is sampled every 10 μs, corresponding to a 1.5 km spacing in altitude samples. For mesospheric studies, 20 samples are taken for each pulse, typically corresponding to the altitude range 60 to 90 km. Due to a data processing bottleneck, the real and imaginary phase detector outputs are sampled for alternate pulses, resulting in an effective pulse rate of 200 Hz.

The quantities to be estimated from these samples are scattered power, Doppler velocity, and correlation time, all of which may be calculated from

an estimate of the autocorrelation at each altitude over an appropriate time period, as described in Miller et al. (1978) and briefly summarized below. The SNR of a single pulse is insufficient for such estimation, but the quantities under investigation are believed to change slowly, while the noise is assumed uncorrelated from pulse to pulse. Therefore, the SNR can be improved by averaging, and this is done in two stages. First, 25 succesive complex samples from each altitude are summed, corresponding to a 125 ms integration time. Next, three autocorrelation lag estimates are calculated for each altitude from these 125 ms complex integrated samples. Finally, these autocorrelations are averaged by summing for one minute. These stages of data processing are performed in real time by the collection computer, which is either a DEC PDP-15 or an Apple II. The autocorrelation estimates are stored on disk for off-line postprocessing. This study is concerned with the scattered power estimates, so the postprocessing required for the estimate of scattered power is described further below.

The autocorrelation function at lag zero is a measure of total power received, signal plus noise. Noise power is assumed constant over altitudes and times of the order of at least an hour. Therefore we may deduce fluctuations in power over both altitude and time. It is expected that the minimum scattered power from any altitude in a typical two hour data set is a reasonable estimate of the noise power (as in Gibbs and Bowhill, 1983), although this is clearly an upper bound, and thus biased upward.

Power at each altitude and minute is written to an Apple disk file as 100 times the log of the power. This allows any received power in the range encountered to be stored as an integer, typically between 600 and 1000. The date, time, number of minutes, maximum, minimum, and average power, and base altitude are stored in a header file, in a standard fashion (see Roth, 1982

for details).

After postprocessing, power data are plotted for the 20 altitudes over the two-hour observing period. Plots are in the form of standard 8 1/2" x 11" pages, created via an HP-9830 pen-plotter. Data in this form exist and are bound in notebooks for several hundred hours of observation time, typically in two hour time periods near local noon, plus several extended time periods. Data were colected irregularly during 1978, on only one day in 1979, approximately weekly from April 1980 to March 1983, and nearly daily from March 1983 to the present. This was the database searched for flare effects.

4.2 Observing solar flare effects with MST radar

With the records of scattered power collected by the Urbana MST radar and the known time of a major flare, an analysis of the effects of the flare on the level of scattered power at each time and altitude may be undertaken. Discussion of the relation of flare-time X-rays to electron density has been related in Chapter 3 above. Relating electron density to scattered power is the subject of this section.

The scattered power is proportional to the mean square fluctuation of the refractive index μ, $\langle \delta\mu^2 \rangle$ (Hocking, 1983). At VHF, effects of the earth's magnetic field may be neglected, so μ is related to the electron density N by

$$\mu^2 = 1 - Ne^2/\varepsilon_o m\omega^2 \qquad (4.1)$$

(Hocking, 1983) where e and m are the charge and mass of the electron, ε_o the permittivity of free space, and ω the angular frequency of the impinging wave. The term on the right is small compared to unity, so that

$$\mu = 1 - Ne^2/2\varepsilon_o m\omega^2 \qquad (4.2)$$

Thus fluctuations in μ and N are proportional, and so are their mean

squares. Therefore, scattered power is proportional to the square of the fluctuations in electron density, i. e.,

$$P \propto \langle \delta N^2 \rangle. \tag{4.3}$$

This mean-square electron fluctuation is caused by turbulence acting on a vertical gradient N' of the background electron density. From Rastogi (1975), we have

$$\langle \delta N^2 \rangle \propto N'^2 \tag{4.4}$$

for a given constant turbulent velocity field. Now, let us suppose a solar flare increases the electron production function q, and that ion chemistry produces a corresponding increase in N. If N increases by a constant factor over the altitude range of interest, N' will as well. Leaving aside for a moment the time scales involved, this simple analysis predicts

$$P \propto N^2. \tag{4.5}$$

As in the question of electron loss rates in the previous chapter, the question of equilibrium now becomes important. If the turbulent mixing were instantaneous, or at least fast with respect to the changing of electron production, we would expect $\langle \delta N^2 \rangle$ to be proportional to N'^2. However, if turbulent mixing is slower than the ionization increase, we would expect to see a time lag between the electron production function and the rise in scattered power.

It is also possible that the concentrations of ionizable constituents or electron loss reactants are advected by the turbulence in such a way that a region of highly varying electron concentration is created instantaneously, without need of further turbulent advection for an increase in scattered power. In this case no significant delay between q and P is expected.

Therefore, flare events may be analyzed as a function of time at each

altitude, comparing the local increase in N with q estimated for that altitude by the methods of Chapter 3. This is the subject of the next section.

4.3 Methods of analysis

At a given altitude, our ability to observe the immediate effects of the flare may be hampered by a number of problems. Some of these relate to the chemistry at that altitude, and some are due to differences in the behavior of turbulence. Both types of features may be roughly associated with different altitude ranges, but the actual situation on a given day is at present impossible to predict in advance. Rather than imposing static methods of analysis on any given altitude, a flexible approach is taken. Preliminary analysis is performed at a given altitude for a given flare, and when that shows favorable features of turbulent scatter, further analyses may be performed. Further, the coherent scatter data are used to distinguish between possible types of chemical schemes which may be operating at that altitude. When regions of like chemical scheme are identified, some of the turbulent effects may be averaged out, and the quantity q_0 may be estimated. We now describe this entire process in greater detail.

At some altitudes, no significant increase in scattered power may be observed during the flare. This lack of increase may have two causes. First, there may be insufficient turbulence at that altitude to create coherent scatter, even with an increase in electron density. Second, the strength of turbulence in a layer may fluctuate considerably; simply by chance, there could be a hiatus in turbulence strength near the time of the flare. The altitudes which show no effect are different for each flare event, and do not yield useful data, although their locations may be of interest.

At other altitudes, there may actually be a decrease in scattered

power, due to incident power absorption at lower altitudes. This is rare, and is not studied in this work.

The strength of turbulence in the antenna beam and one sampled range interval may change at a given altitude by several dB over a few minutes. This sort of behavior is probably due to instabilities which generate bursts of turbulence, with one or more intermittent layers dominating the range received during the times of high scatter. The power may increase as much as 20 dB in a few minutes, remain high for ten minutes or so, then decrease to near or below the noise level.

Enhancements of ionization due to flares are hard to analyze in this case. One or two approaches might be suggested. Perhaps the flare will happen to occur at the time of a turbulent peak, in which case the resulting peak could be further enhanced, and so rise above the fluctuating levels for the entire day. Such an occurrence could be analyzed in a tentative manner, comparing a very rough estimate of the power enhancement with the estimated increase in q. Alternatively, one could construct a method in which the effects of several different flares are analyzed together in a statistical manner to obtain some sort of mean effect. This procedure requires a database containing many flare enhancements, and a method for averaging effects of flares of different sizes. The diversity of possible conditions probably makes this procedure impossible, at least with a moderate-sized database, and we do not attempt it in this study.

At some altitudes, temporally constant scattering layers dominate the altitude range sampled. In this case, the average turbulence strength over the volume stays fairly constant. Thus, the relationship $P \propto N^2$ may be valid. If either the turbulent mixing acts fast compared to the flare effect, or the fluctuations in electron density are due to previously mixed

constituents ionized immediately by the flare, the curves for estimated q and P will be observed to coincide. This has in fact been observed for several flares, which are analyzed in Chapter 5.

When this is the case, we may do a datailed analysis of a single flare event in a narrow altitude range. We make the following assumptions.

1. If

$$P = EN^2 \tag{4.6}$$

and a chemical model of the sort described in Chapter 3 allows the use of an effective recombination coefficient α_{eff} as

$$q = \alpha_{eff} N^2 \tag{4.7}$$

we may conclude

$$P = Eq/\alpha. \tag{4.8}$$

2. If E is the same before the flare as during, we may factor its effects out of the analysis as shown below.

3. If α_{eff} doesn't change, we may use the ratio of flare-time scattered power to the preflare average scattered power, as follows. Choose a time period before the beginning of the flare, when the power scattered is due to an undisturbed electron density profile advected by turbulence. Average the scattered power over this time; call this quantity P_0. Thus, during the undisturbed time,

$$q_0 = P_0 \alpha / E. \tag{4.9}$$

During the time of the flare, the total electron production function is

$$q = q_x + q_0 = R\alpha/E. \tag{4.10}$$

Therefore,

$$(q_x + q_0)/q_0 = P/P_0 \tag{4.11}$$

(factoring out the presumed constants α and E). Thus

$$q_x/q_0 = P/P_0 - 1. \tag{4.12}$$

This quantity may be computed for each minute of the flare at the altitude range in question, and it may then be compared to the estimate of q_x obtained from the satellite X-ray data described in Chapter 3. If all the assumptions are met, we may plot this estimate of q_x/q_0 (from the scattered power) on a log-log plot against q_x, and the result will roughly approximate a straight line of slope one, since the two should be proportional by the constant q_0. Further, the intercept of this line with the line

$$\log(q_x/q_0) = 0 \tag{4.13}$$

is an estimate of the value of q_0. These estimates of q_0 may be plotted for several altitudes, or compared for different zenith angles or times of year, to gain insights into the nonflare ion-pair production processes, which in the D-region typically involve the density of NO, the column abundance of O_2 above the altitude observed, and the intensity of Lyman-α radiation.

If the result of the q_x/q_0 vs. q_x plot is not a straight line of slope one, one may try assuming an effective attachment coefficient, β, and repeat the above analysis with a linear relation between q and N. The resulting estimate of q_x/q_0 is

$$q_x/q_0 = \sqrt{P/P_0} - 1. \tag{4.14}$$

Again, the intercept yields q_0. Further, we may map out which altitudes have effective attachment rates, and which have effective recombination coefficients, which may yield insights concerning electron loss processes.

4.4 Problems of analysis

There are problems in the assumptions behind the analysis techniques above. Especially troubling are the assumptions of equilibrium and the temporal constancy of the turbulent layers.

First, we are performing an analysis relating the flare-induced X-ray flux at a given instant to the coherent scattered power at that same instant, ignoring the possible effects of past electron production and density. This sort of analysis requires two kinds of equilibria: the change in electron density on a large spatial scale must be small compared to the production and loss terms, and the change of electron density fluctuation on the smaller scale detected by the radar must be small compared to the production and disappearance of such irregularities. Our knowledge of the relative sizes of these terms is insufficient to decide the validity of these equilibrium assumptions in advance. However, we are studying a phenomenon (solar flares) which produces a time-dependent q_x with a well-defined peak. If either of the equilibrium assumptions above are violated severely, we would expect a noticeable delay between this peak and the time of peak electron density.

Similarly, there is no way to be certain that the turbulent mixing contribution to the scattered power is constant during the flare, even in some average sense. However, several altitudes for several flare events show many minutes of near-constant power before the flare event, and a reasonably smooth increase during the flare, sometimes closely paralleling the estimated q_x time curve. We take this as sufficient evidence for the assumption of a constant turbulent layer.

However, it will be seen in the results in Chapter 5 that, for example, the spread of the data about a line of unit slope for a quadratic q vs. N relation, is fairly wide. This demonstrates the limits of the assumption of the constancy of the turbulent layer.

5. RESULTS OF THE ANALYSIS OF FLARE EFFECTS

5.1 Criteria for choosing flares for study

The procedure for selecting flares for study was the examination of the records in Solar-Geophysical Data, compiling a list of events which could cause observable effects, and comparing the list with the days of available coherent-scatter data. Reports of events detected by three observational methods are considered before a final criterion for flare selection is chosen.

First, we consider Hα events. These are recorded in Solar-Geophysical Data, published one month after observation. Although these are observed in a wavelength (656.3 nm) quite different than those causing ionization in the atmosphere, these events are known to be highly correlated with ionospheric effects (Dasgupta et al., 1973). However, small Hα events are frequent, and sometimes occur at the time of a large flare ionization event. Thus these records are inconvenient for a search of coherent-scatter effects, as many small events would have to be checked against radar data, with very few yielding observable effects.

Second, there is a network of radio link observers which reports the occurrence of SIDs. These reports are recorded in Solar-Geophysical Data, in the publication two months after the event. These reports seem to be ideal for this work, since these observations are of the same ionization effect that concerns this study. They are reported with indices indicating the magnitude of the events (from 1- to 3+, a 9 level scale), and the degree of unanimity among reporting stations on the sunlit hemisphere as to whether the event was in fact an SID.

However, this work discovered a deficiency in the reporting of SIDs. We

do not believe this has been discussed in the literature. The reporting of SIDs is drastically nonuniform in different parts of the world, as is now demonstrated.

Figure 5.1 shows the distribution of reported SIDs of magnitude 3-, 3, and 3+ for the period July 1980 to July 1983, according to time of occurrence (UT). Theoretically, if reporting on SIDs were uniform around the globe, this should be a sample from a uniform distribution, since flares are solar phenomena, not influenced by terrestrial rotation. Yet the distribution does not seem remotely uniform. This impression is confirmed by performing a chi-squared test with the sample. The times of events are, for computational convenience, placed in bins of 2-hour duration. A total of 153 events are recorded, so the expected value for each bin is 12.75. The chi-square sum is formed:

$$\chi^2 = \sum (x-12.75)^2/12.75. \qquad (5.1)$$

The result is found to be 75.16. This result is compared with a table of chi-square probabilities, with 11 degrees of freedom (from Abramowitz and Stegun, 1964), and the result indicates a probability of occurrence below 10^{-5}. The asymptotic form of the probability integral may be used (Abramowitz and Stegun, 1964, Eq. 26.4.12), yielding a result of about 1.3×10^{-11}. In short, the chances of obtaining a sample from a uniform distribution which deviates at least as much from the expected mean as the one in Figure 5.1 are less than one in ten billion.

Since SIDs should affect an entire hemisphere, the distribution of stations in Figure 5.2 should yield a nearly uniform time distribution, but this is not the case. It is concluded that the network of observing stations is biased in some respect. Either events of large magnitude are erroneously reported, or large events are missed or underestimated much of the time.

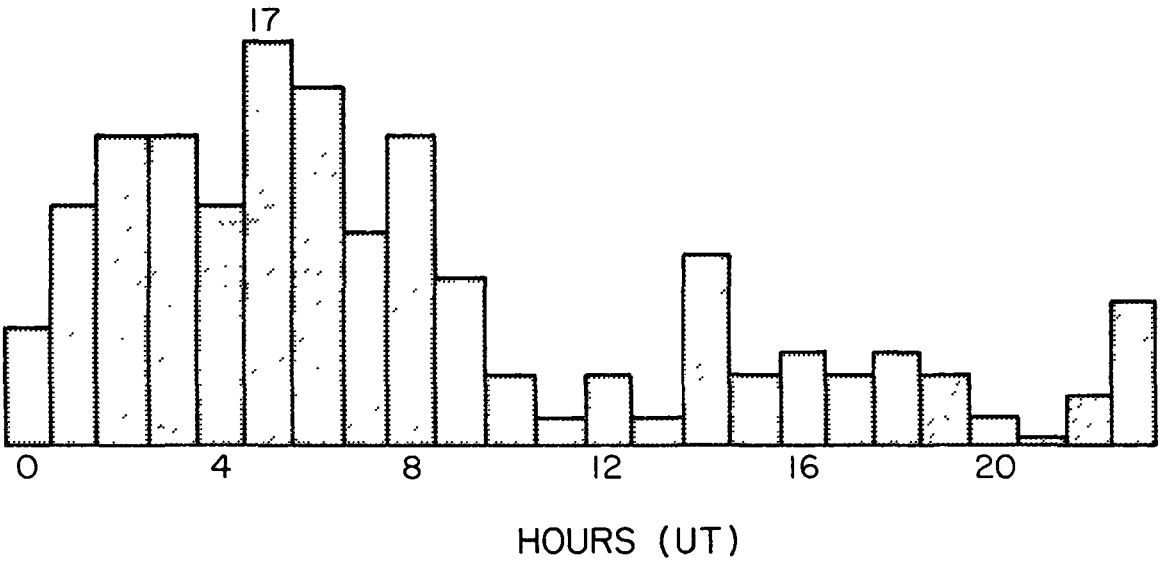

Figure 5.1 Distribution of SIDS of importance 3-, 3, or 3+, from July 1980 to July 1983.

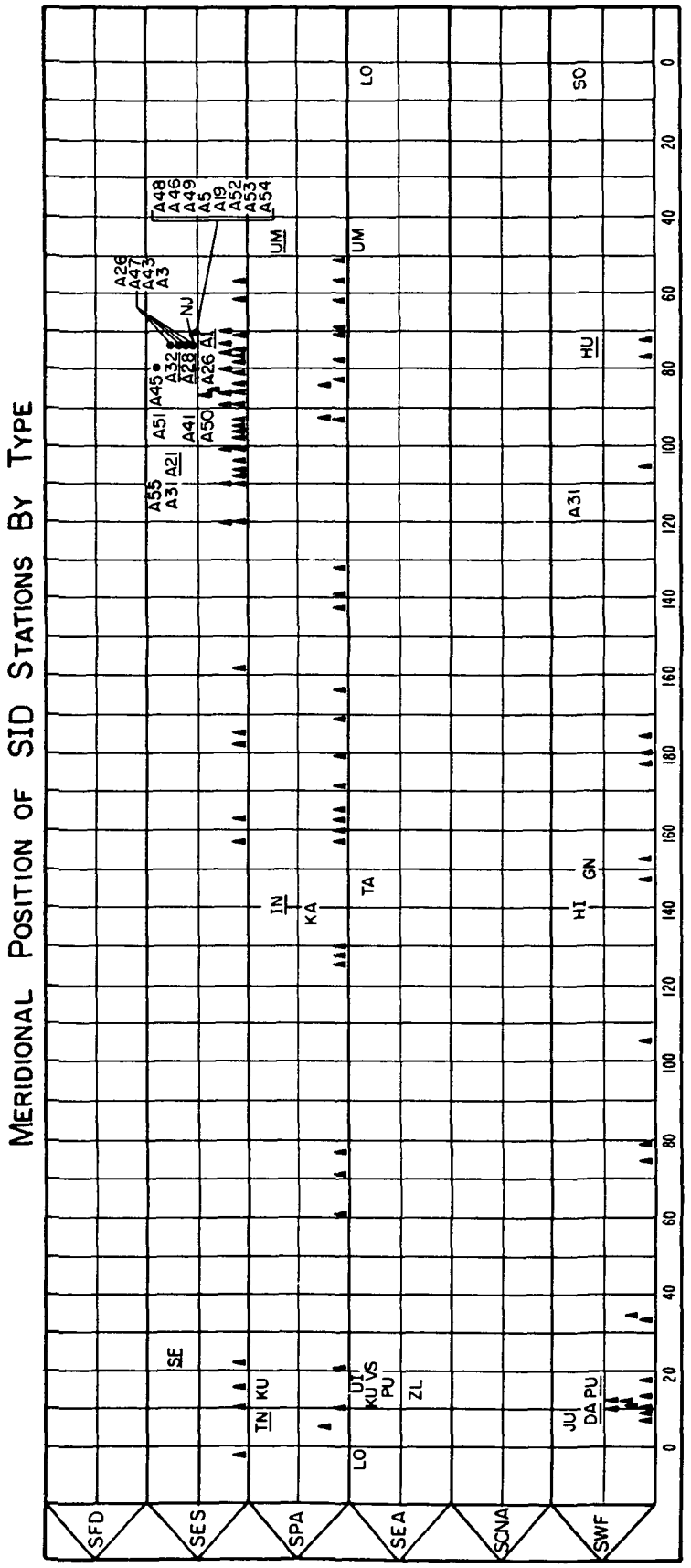

Figure 5.2 Geographical distribution of SID observing stations (NOAA, 1981).

Either way, the use of reported SIDs to identify likely coherent-scatter effects is not as good as one might expect.

The third sort of record in Solar-Geophysical Data, and the one found to be of most help to this work, is the plots of X-ray intensities from the GOES satellite detectors. These are published six months after the time of the records in the form shown in Figure 5.3. The spikes above the background X-ray level indicate solar flare enhancements. Note the diversity in size: the many small events are unlikely to cause a noticeable D-region effect. In order to obtain a list of times of probable D-region ionization enhancements to compare with the existing Urbana coherent-scatter records one must establish a criterion to limit the selection of X-ray events. A very simple criterion is used: a threshold of 2×10^{-5} watts/meter^2 for the 0.1-0.8 nm flux must be exceeded in order for a flare to be included in this study. This procedure produced an adequate number of events which caused observed scattered power enhancements for this work. A more exhaustive study might use a lower threshold and perhaps an additional hardening ratio criterion. Since one event which barely met the criterion above produced quite a substantial effect, it is likely that more D-region flare effects may be found in the Urbana data in future work.

As a check on the advantage of using X-ray events as a criterion, the distribution of events exceeding the threshold during the period from July 1980 to January 1983 was examined (Figure 5.4). This is a substantial subset of the time period checked for SID uniformity. This distribution appears to be more uniform, and this impression is confirmed by a chi-square test: the expected number of events in each two-hour bin is 8.92, the χ^2 sum is 7.95, and the probability of getting this value or greater is about 0.71. Thus we have found no evidence that this sample is not from a uniform

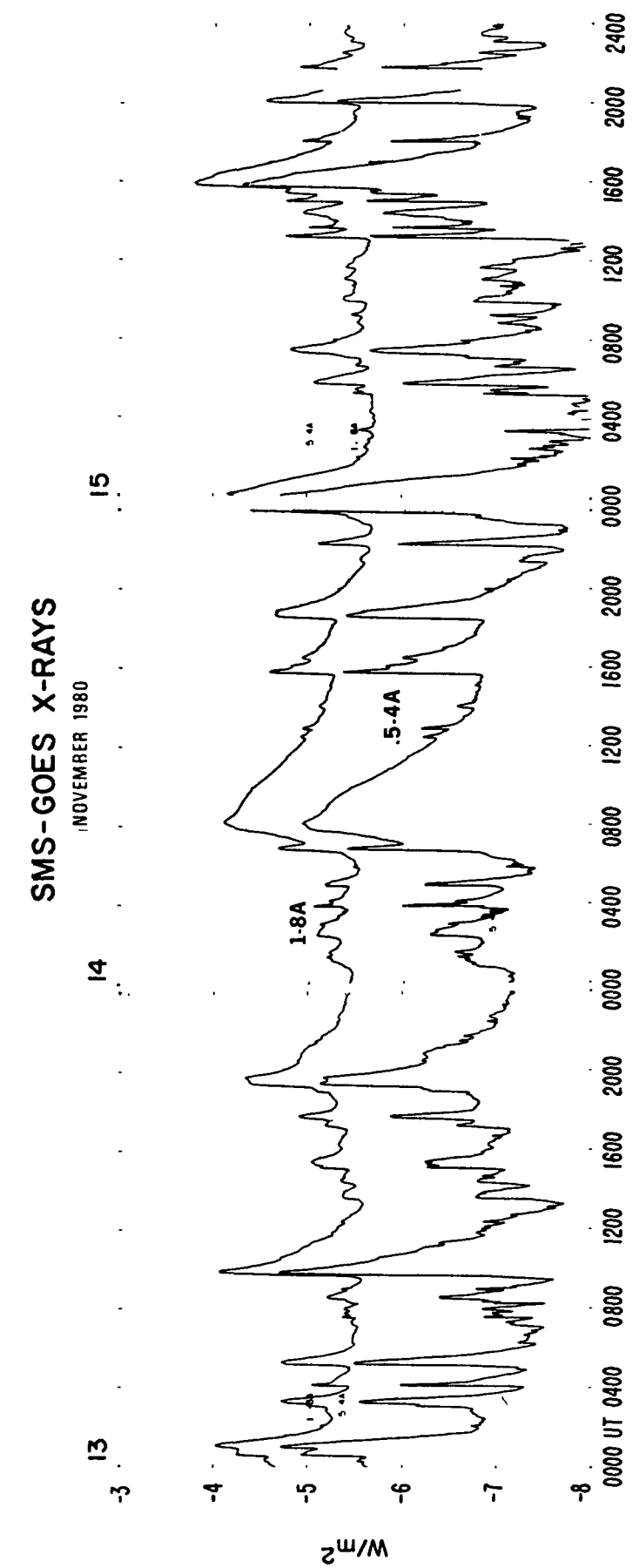

Figure 5.3 Example of Solar-Geophysical Data plot of GOES X-ray detector data for three days in November 1980.

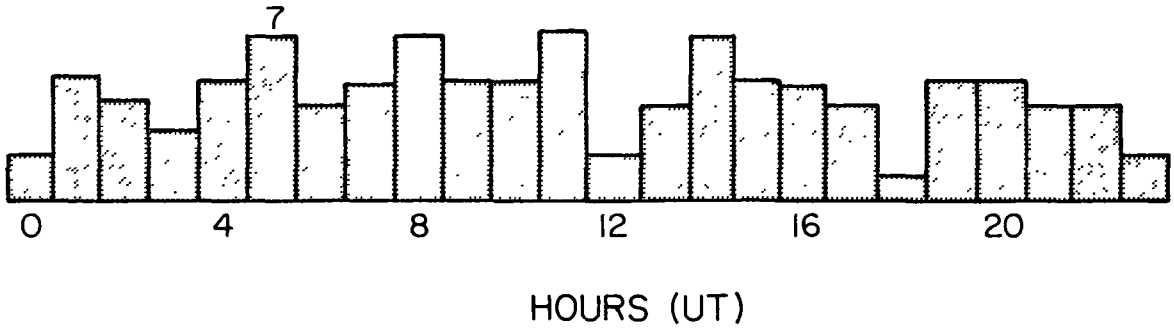

Figure 5.4 Distribution of X-ray events with 0.1-0.8 nm flux exceeding 2×10^{-5} W/m^2, from July 1980 to January 1983.

distribution, as expected.

Once likely candidates from the X-ray data are chosen, the following criteria are applied to the coherent-scatter data to establish the occurrence of a flare effect.

1. The existence of unusual power enhancement, at the time of the X-ray event, for at least one altitude is found by visual inspection of the archived HP-9830A plots of scattered power (described in Chapter 4).

2. More subtle power enhancements at the time of the flare are detected by a visual inspection of the coherent-scatter velocity plots. Slight increases in scattered power often allow determination of velocities at altitudes which do not usually have an adequate signal-to-noise ratio for such determinations. The plotting system does not record velocities at such altitudes. Thus the sudden appearance of velocity data on these plots at the time of a flare, at several altitudes, is evidence of a flare-time ionization enhancement.

Events which met all the above criteria, during the period from April 1978 to December 1983 are listed in Table 5.1.

5.2 Comparisons of X-ray electron production and scattered power

One event with particularly favorable results is presented first, and the analysis is discussed in some detail. Additional events are discussed more briefly in the latter part of this section.

The flare at 1250 CST on November 14, 1980, was reported as a class 2+ SID and a 1B Hα flare. The GOES X-ray detector plots were obtained from the National Data Center, Boulder Colorado, and are shown in Figure 5.5. The values of flux for each detector have been reduced by hand from these plots and entered in an Apple II text file for automated analysis. The scattered power from the mesosphere is shown in Figure 5.6. The data are stored in an

Table 5.1 X-ray flare events producing measurable coherent-scatter radar power enhancements between April, 1978 and December, 1983.

yr	mo	da	cst	SID	Hα	pk flux x10^{-5} w/m^2 0.1-0.8nm	pk flux x10^{-5} w/m^2 0.05-0.4nm	61.5-75 km pk CS power dB above P_0	χ
78	04	11	0820	3+	NA	20	3.5	7.7	60.7
80	05	21	1510	3	3B	14	3.2	29.8	45.1
80	05	28	1354	2+	2B	12	2.0	3.5	45.9
80	11	13	1324	2+	1N	4.2	0.7	11.2	63.8
80	11	14	1239	2+	1B	2.4	0.4	13.8	60.5
81	01	27	0947	2	1B	4.6	1.3	6.1	63.8
81	05	05	0809	3	3B	12	3.3	2.8	53.1
81	08	03	1425	2+	1N	7.1	1.8	10.1	38.5
81	10	14	1111	2+	1B	30	11	7.4	49.1
82	03	31	1626	2+	NA	7.5	1.7	4.9	70.7
82	06	02	0953	3+	NA	10	2.9	17.4	29.5
83	08	13	1215	1	2B	5.2	0.9	3.7	25.3
83	08	21	1159	1	2B	2.2	0.3	6.8	28.1

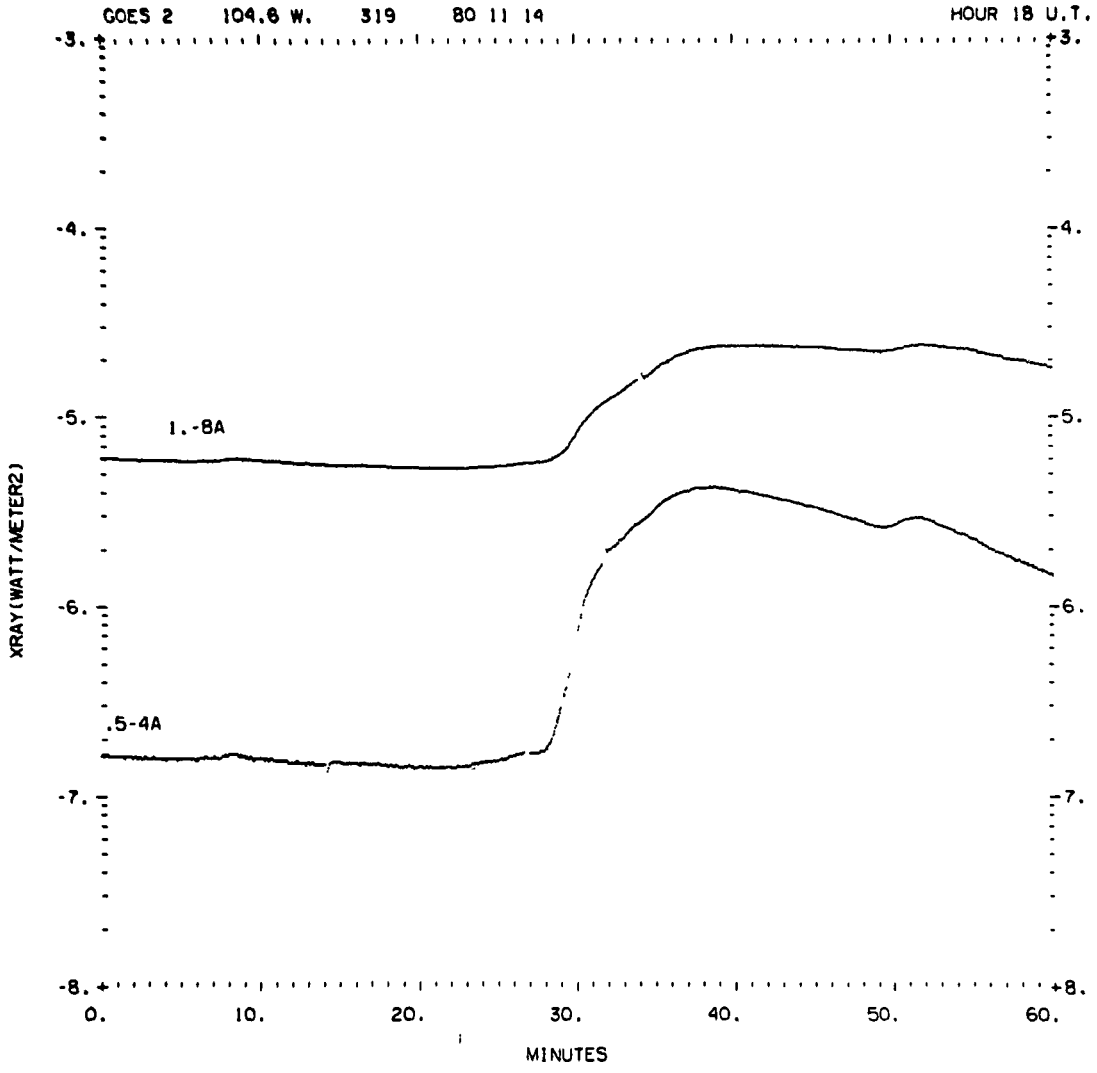

Figure 5.5 GOES X-ray data for 1800 UT, November 14, 1980 (courtesy of the National Geophysical Data Center).

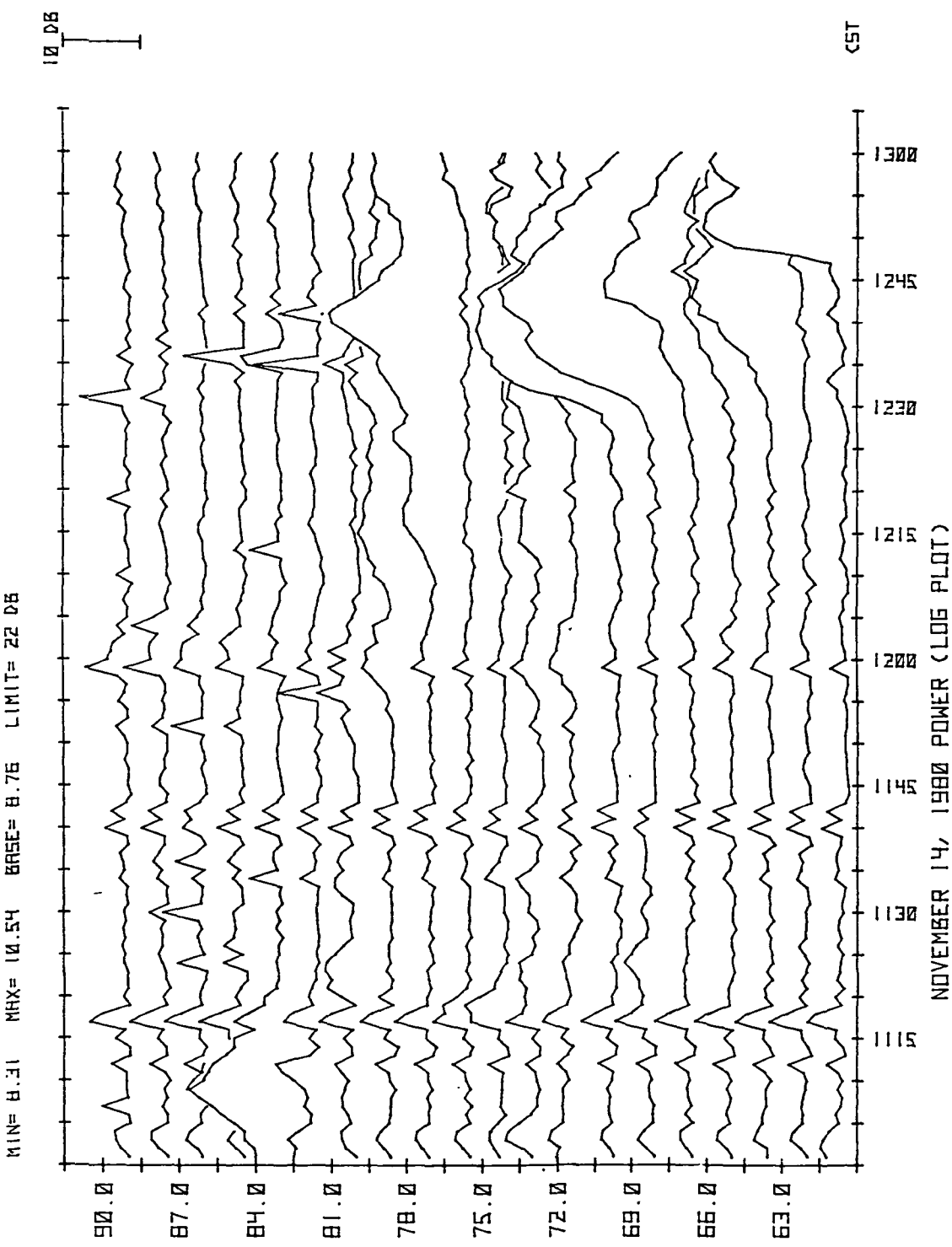

Figure 5.6 Coherent scattered power from 60 - 90 km over Urbana, beginning at 1101 CST, November 14, 1980.

Apple II text file directly from the data collection and processing programs of the Urbana radar system.

A BASIC program, FLAREMASTER5, has been written to carry out the sort of analysis described in Chapters 3 and 4 of this work. The program appears in the appendix. FLAREMASTER5 reads from the Apple text files the values of X-ray flux and coherent-scattered power, and then calculates and writes to another text file the following quantities:

1. the moment-by-moment average power from a range of altitudes specified by the user,

2. the total preflare average power at those altitudes at a specified range of times, and

3. estimates of the X-ray induced additional electron production function q_x at the midpoint of the altitude range specified, according to Equation 3.28. The program prompts the user for the values of the zenith angle χ, scale height H, and air number density [m]. In this work χ was computed by

$$\chi = \arccos(\cos(\theta_u - \theta_s)\cos(\phi_s)\cos(\phi_u) + \sin(\phi_s)\sin(\phi_u)) \qquad (5.2)$$

where θ_u and ϕ_u are the latitude and longitude of the transmitter, and θ_s and ϕ_s are the latitude and longitude of the point on earth which has the sun directly overhead, computed from the Grenwich hour angle of the equinox, the universal time, and the right ascension and declination of the sun taken from the American Ephemeris and Nautical Almanac for the year 1978 (USNO, 1976). The values of H and [m] are taken directly from the U. S. Standard Atmosphere (NOAA, 1976).

The calculation of the estimate of q_x involves modelling the X-ray spectrum as the power law form

$$I = A\lambda^B \qquad (5.3)$$

where A and B are calculated from the X-ray chamber wavelength response according to Equations 3.20 and 3.21. Note the closeness of the relationship of R and B shown in Figure 3.5 to the function

$$R = 2^{B+1}. \tag{5.4}$$

It is adequate to use the inverse function, $B = \log_2 R - 1$, in the program to calculate B, and this is done to save computation time. The value of A cannot be so simply estimated; therefore Equation 3.21 is used directly, with the integral performed as two 6-point Gaussian quadrature sums.

The file containing the estimates of q_x and the average scattered power is transferred to an HP 9830A computer for plotting, producing three varieties of diagrams. The HP computer subtracts the estimated noise power (see Chapter 4) from each scattered power point, and performs the final computations for plotting.

The first two plots are on log-log scale plots of q_x vs. an estimate of q_x/q_0 from the scattered power values at each of the moments of the flare event. The first diagram assumes the total electron production function q ($= q_x+q_0$) is proportional to the square of the electron density, i. e.,

$$q = \alpha_{eff} N^2. \tag{5.5}$$

Therefore the estimate of q_x/q_0 is

$$q_x/q_0 = P/P_0 - 1. \tag{5.6}$$

The second diagram assumes a linear relationship between q and N, and thus uses the estimate

$$q_x/q_0 = \sqrt{P/P_0} - 1. \tag{5.7}$$

The diagram which most resembles a line of slope 1 represents the assumption regarding q and N which is probably correct. On that diagram we may estimate the value of q_0 from the point where the slope 1 line crosses the

$$\log(q_x/q_0) = 0$$

line, as desribed in Chapter 4.

These diagrams are shown at the top of Figure 5.7 for the altitude 70.5. Clearly the first diagram does not represent a line of slope 1; the second is very nearly so.

Note that the points which are nearest to the top right corner are the time of maximum flare enhancement, and so are of greatest significance. Most of the diagrams of this type in this work include a few points farther to the left, whose accuracies are dubious at best. Therefore some caution is needed when examining these diagrams: a wide scatter of points toward the left part of the diagram should not disqualify the hypothesis which requires a slope 1 linear fit.

The third diagram, spanning the bottom of Figure 5.7, contains two plots, each a function of time. The first is the log of the ratio of the scattered power to the average preflare scattered power, and always takes the form of a jagged curve spanning the diagram. The second is the log of the estimate of q_x, which only appears during the time of the flare, since it is otherwise below the minimum value which shows on the plot. The juxtaposition of the two allows quick evaluation of the coincidence between the onset, peak and termination of the X-ray and scattered power enhancements.

For the flare of November 14 at 70.5 km, there is no discernible delay between $q_x(t)$ and the scattered power enhancement; the onset and peak occur at about the same times (1229 and 1240 CST, respectively). Further, the other two plots at the top of Figure 5.7 show points on the rise curve and points on the decay along the same line. Therefore we may conclude all equilibrium assumptions of Chapter 4 are valid. In addition, from the slopes

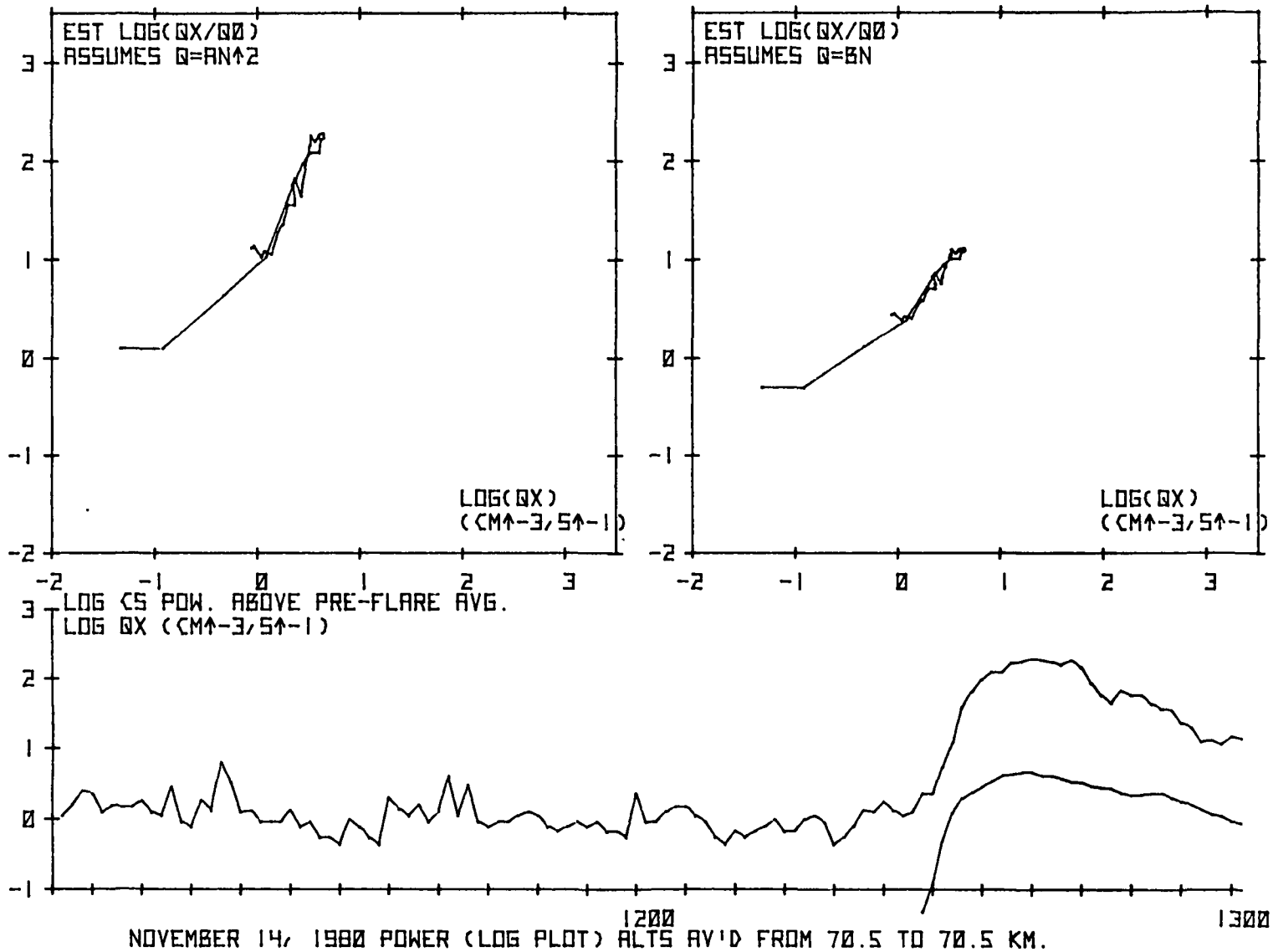

Figure 5.7 Flare-time scattered power enhancement and estimated electron production rate q_x due to flare X-rays at 70.5 km for the November 14, 1980 event.

of the first two diagrams, we may conclude that altitude displayed a linear relationship between q and N with an unknown effective attachment coefficient β, and from the intercept of the $\log(q_x/q_0) = 0$ line we may judge the value of q_0 to be about 1/2 cm^{-3} s^{-1}.

As can be seen from a glance at Figure 5.6, the other altitudes sampled for scattered power do not show such an ideal, immediate, linear response. Altitudes above 81 km show no apparent increase whatsoever. The return from 78 km shows an immediate response, but the relationship between q_x and scattered power seems to be neither proportional nor quadratic as can be seen from Figure 5.8. The altitudes below 70.5 km show a large enhancement of scattered power during the times close to the flare event, but all show some delay. In agreement with the model of ion recombination presented by Thomas (1973), these show increasing delay for lower altitudes. However, there is no way to determine if the lag is due to chemical nonequilibrium or turbulent mixing delay.

Other flare events which show either a linear or quadratic relationship between q and N are those of May 21, 1980; November 13, 1980; January 27, 1981; October 14, 1981; and possibly June 2, 1982.

The November 13 flare occurred on the day previous to the one discussed above. It was observed as a 1N Hα flare, with peak intensity at 1335 CST. Also, there is a recorded class 2+ SID at the same time. The peak X-ray flux was nearly 5×10^{-5} w/m^2 in the 0.1-0.8 nm band. The scattered power is shown in Figures 5.9 and 5.10; the flare event begins at the end of Figure 5.9, and decays at the beginning of Figure 5.10. The altitudes showing nearly simultaneous enhancements are 61.5-63 km, and 69-72 km. Sample altitudes in these ranges are analyzed as above, and the results are shown in Figures 5.11 and 5.12. The q_x curve shows two peaks, which may indicate

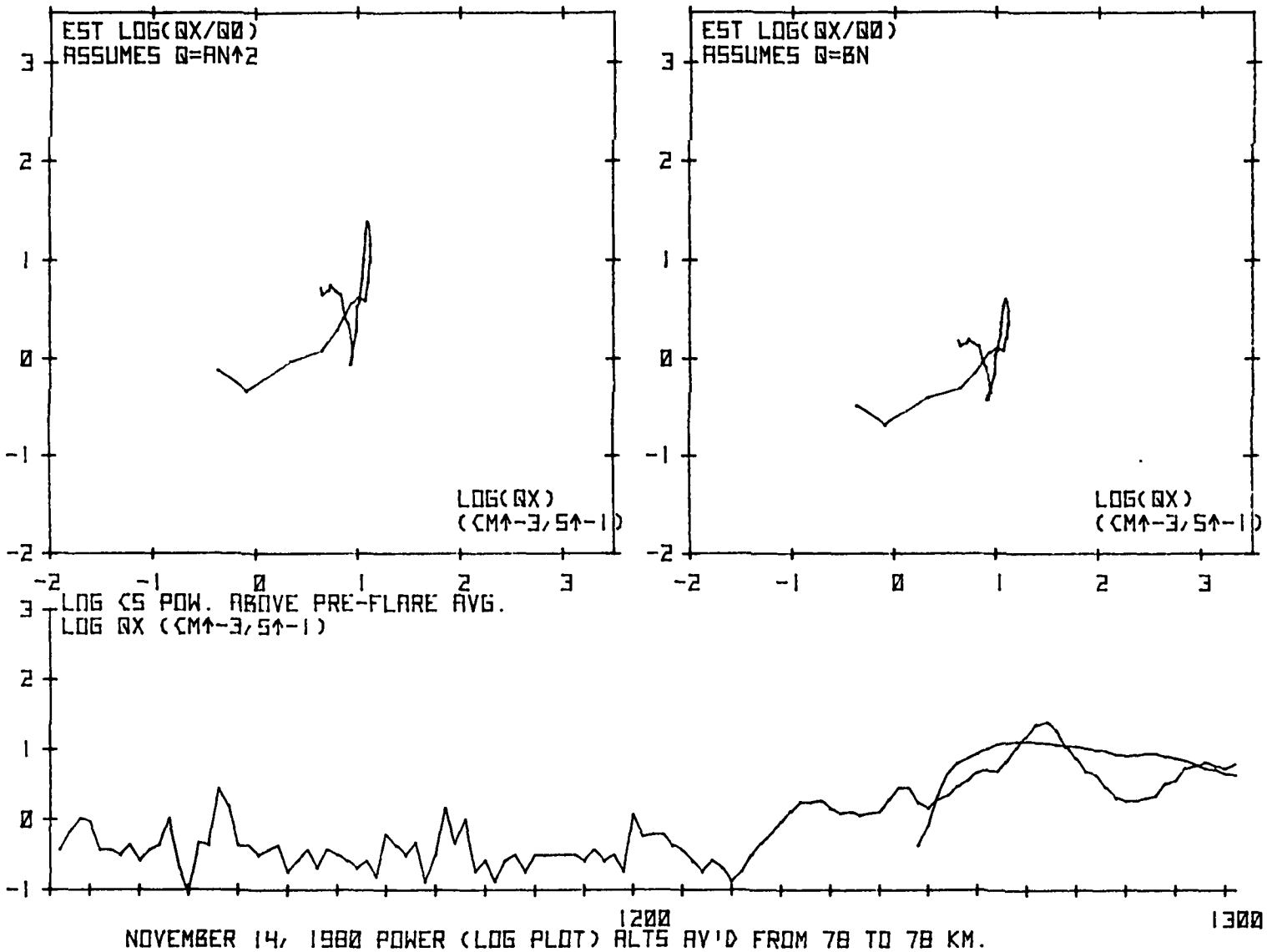

Figure 5.8 Flare-time scattered power enhancement and estimated electron production rate q_x due to flare X-rays at 78 km for the November 14, 1980 event.

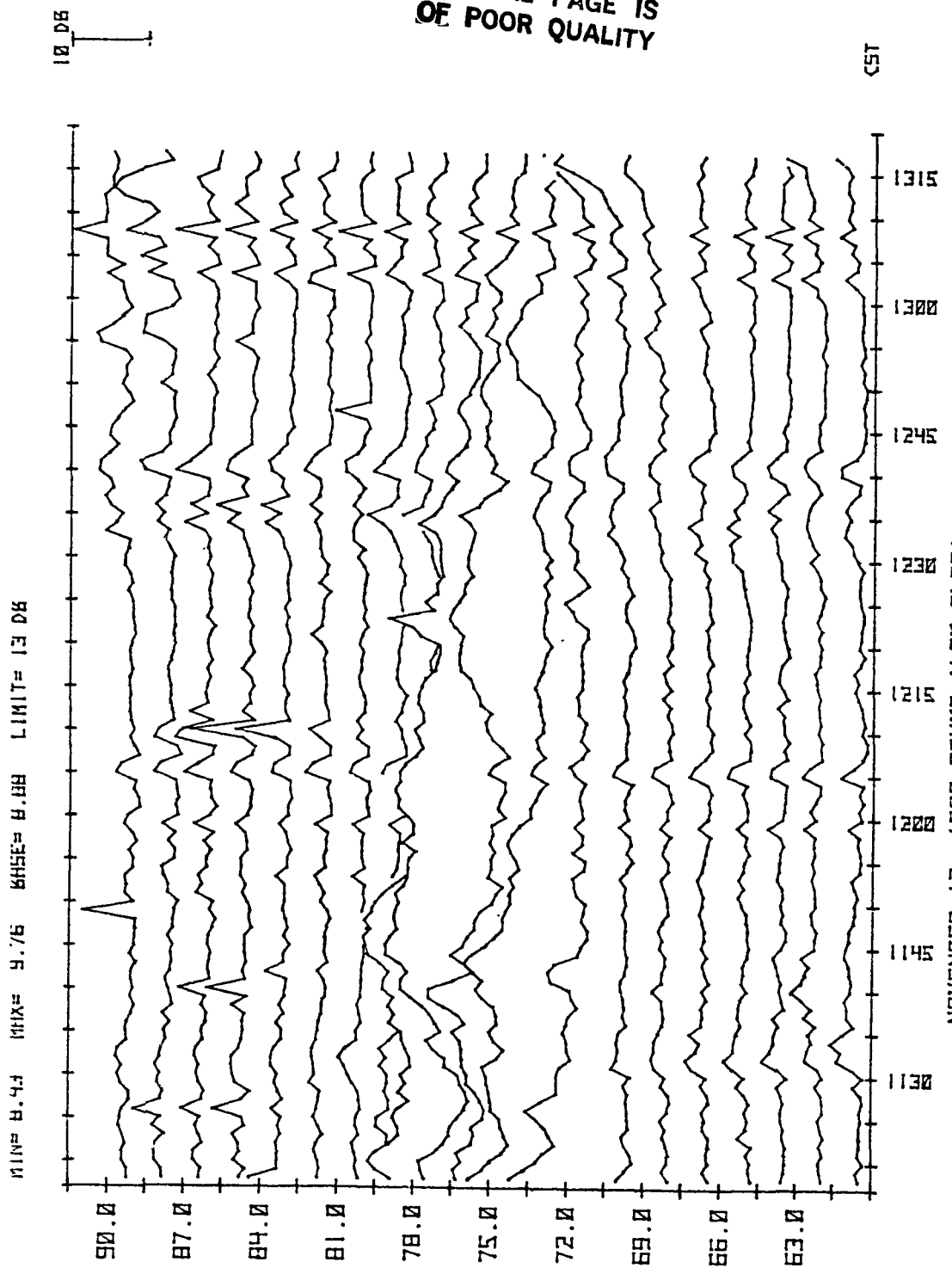

Figure 5.9 Coherent scattered power from 60-90 km over Urbana, beginning at 1118 CST, November 13, 1900.

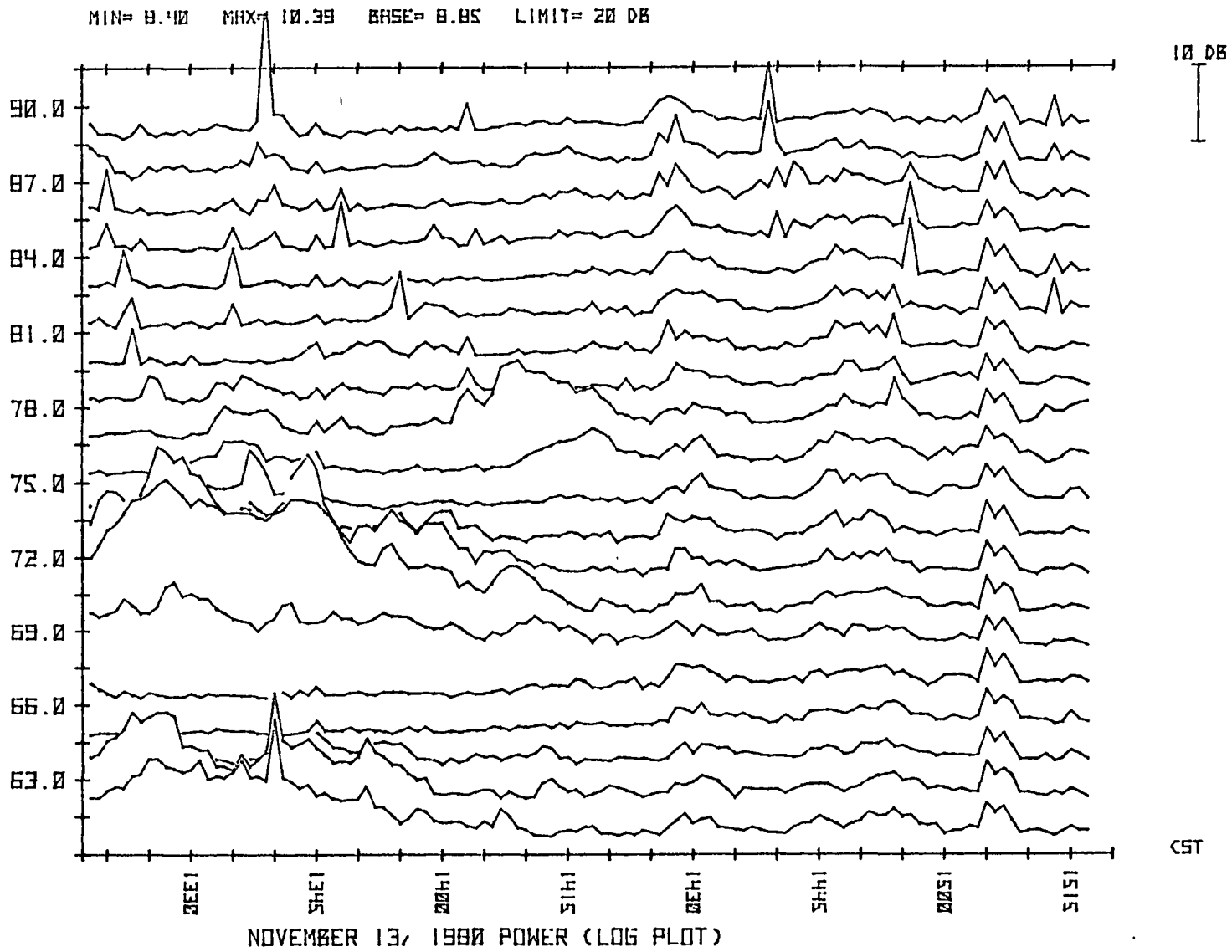

Figure 5.10 Coherent scattered power from 60-90 km over Urbana, beginning at 1318 CST, November 13, 1980.

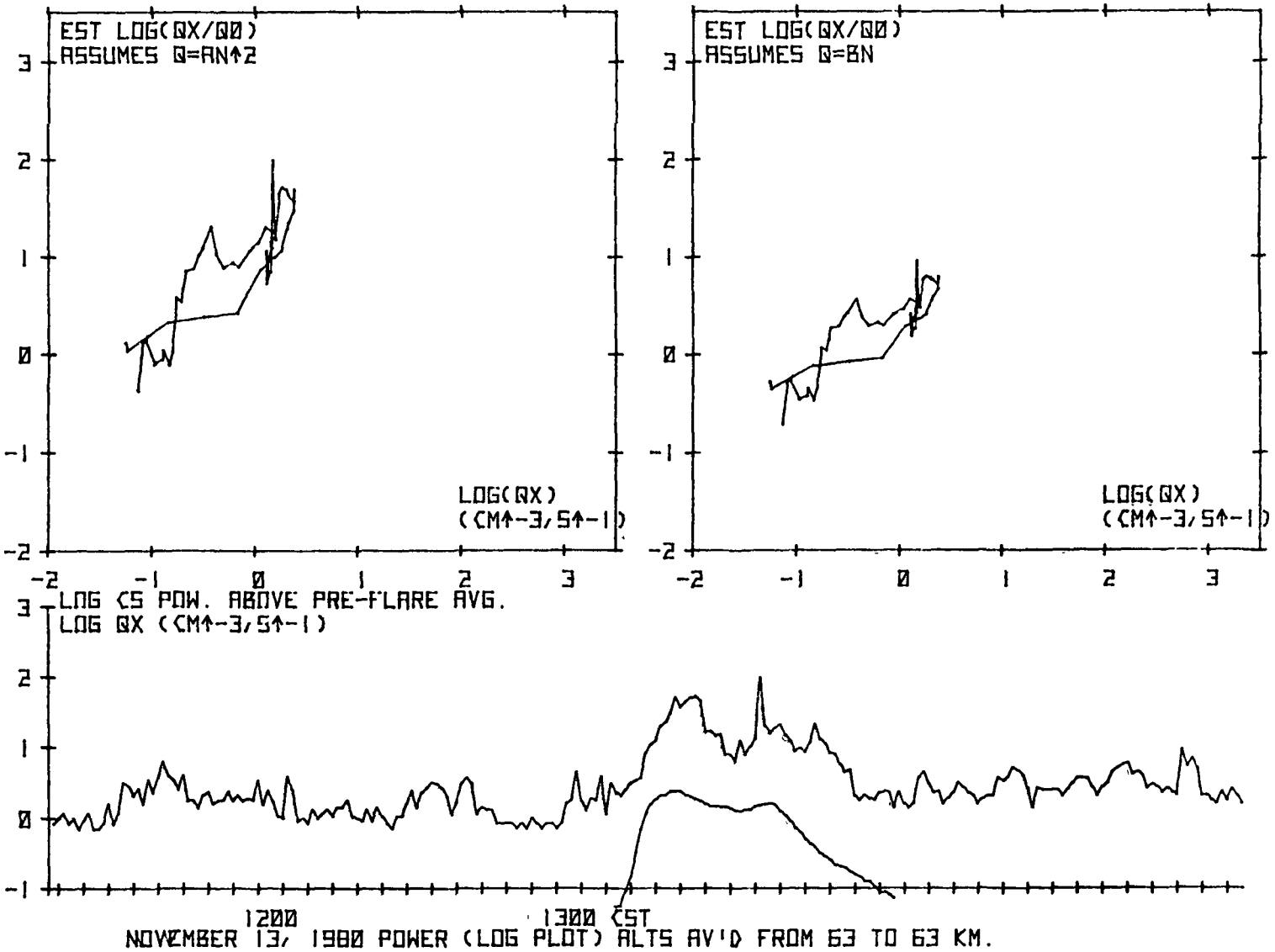

Figure 5.11 Flare-time scattered power enhancement and estimated electron production rate q_x due to flare X-rays at 63 km for the November 13, 1980 event.

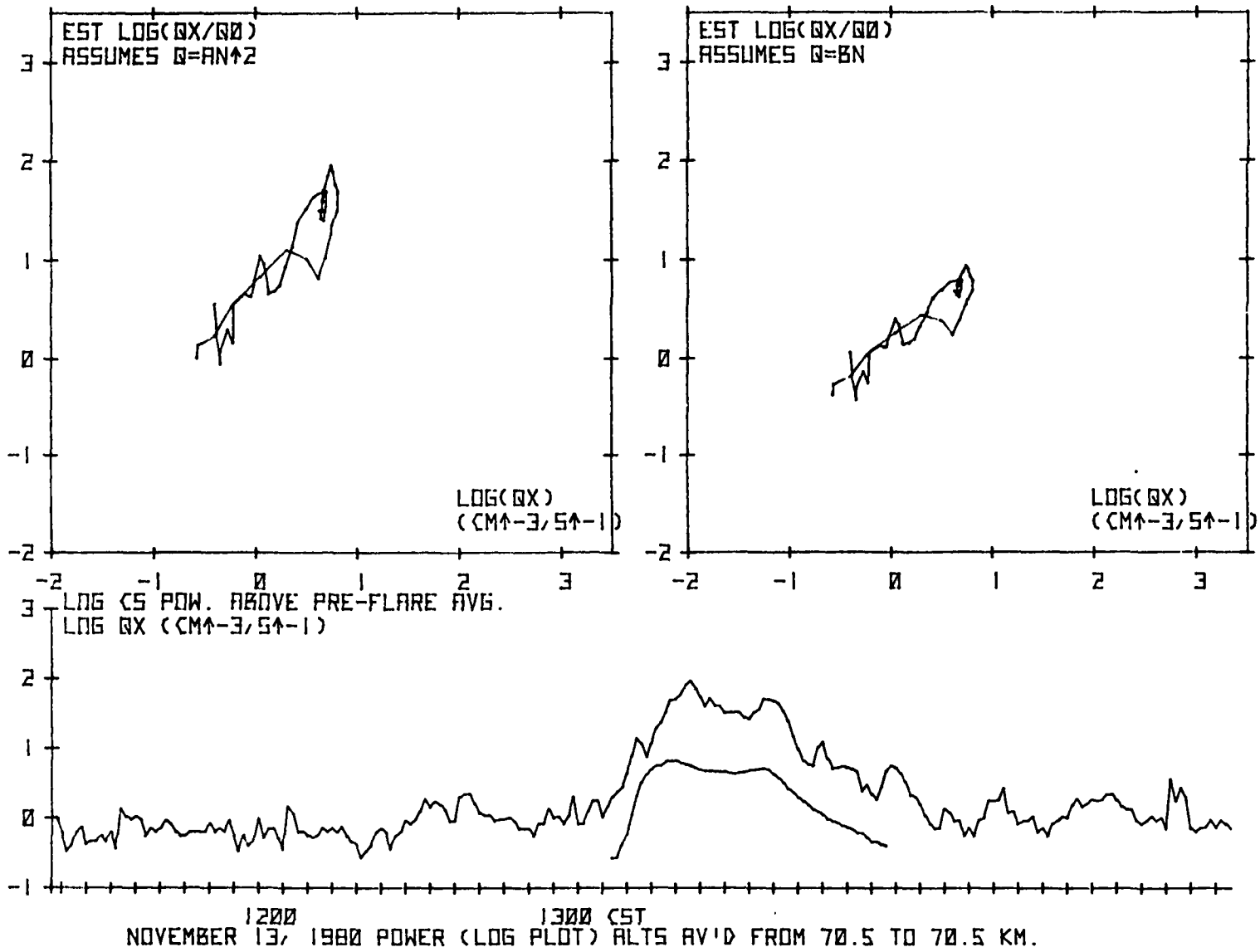

Figure 5.12 Flare-time scattered power enhancement and estimated electron production rate q_x due to flare X-rays at 70.5 km for the November 13, 1980 event.

two separate closely timed flares on the sun. It is particularly noteworthy that the scattered power also shows two major peaks at some altitudes.

The scatter from 69 km and 63 km may show delayed enhancements, but if so, only on the order of three minutes at 63 km, considerably less than the 14 minutes predicted by the model by Thomas et al. (1973). Altitudes from 66 to 67.5 km, and altitudes above 75 km show no no significant enhancement.

The flare of May 21, 1980 is much larger than the November flares: the 0.1-0.8 nm flux maximum is about 1.4×10^{-4} watts/meter^2, the Hα flare is of importance 2B, and the SID is reported to be of importance 3. The scattered power is shown in Figure 5.13. Altitudes showing a linear or quadratic relationship between q and N are 63-66 km, and possibly 75 km. The q_x response plots for those altitudes are shown in Figures 5.14, 5.15, and 5.16. In addition, altitudes 69-72 show what appears to be an unusually strong response, which peaks at about the same time as q_x, but starts later and ends sooner. A typical altitude, 72 km, is shown in Figure 5.17. None of the chemical schemes discussed in Chapter 3 account for such behavior: if we are actually seeing scattered power proportional to N^2, the electron density is increasing faster than either q or $\sqrt{q}$.

The intense enhancement of scatter at 69 km shows a delay of about eight minutes, but that from 66 km shows no delay. Nearly all altitudes show some increase in scattered power at about the time of the flare, but at altitudes above 72 km these are either dubious at any given altitude because of the existence of nonflare enhancements of similar magnitude, or not amenable to this form of analysis due to the erratic behavior of the increase (e.g., the scatter from 85.5 km, Figure 5.13).

The flare of January 27, 1981 is medium sized: the 0.1-0.8 nm flux is about 5×10^{-5} w/m^2. The enhancement is clearly seen scattered power in

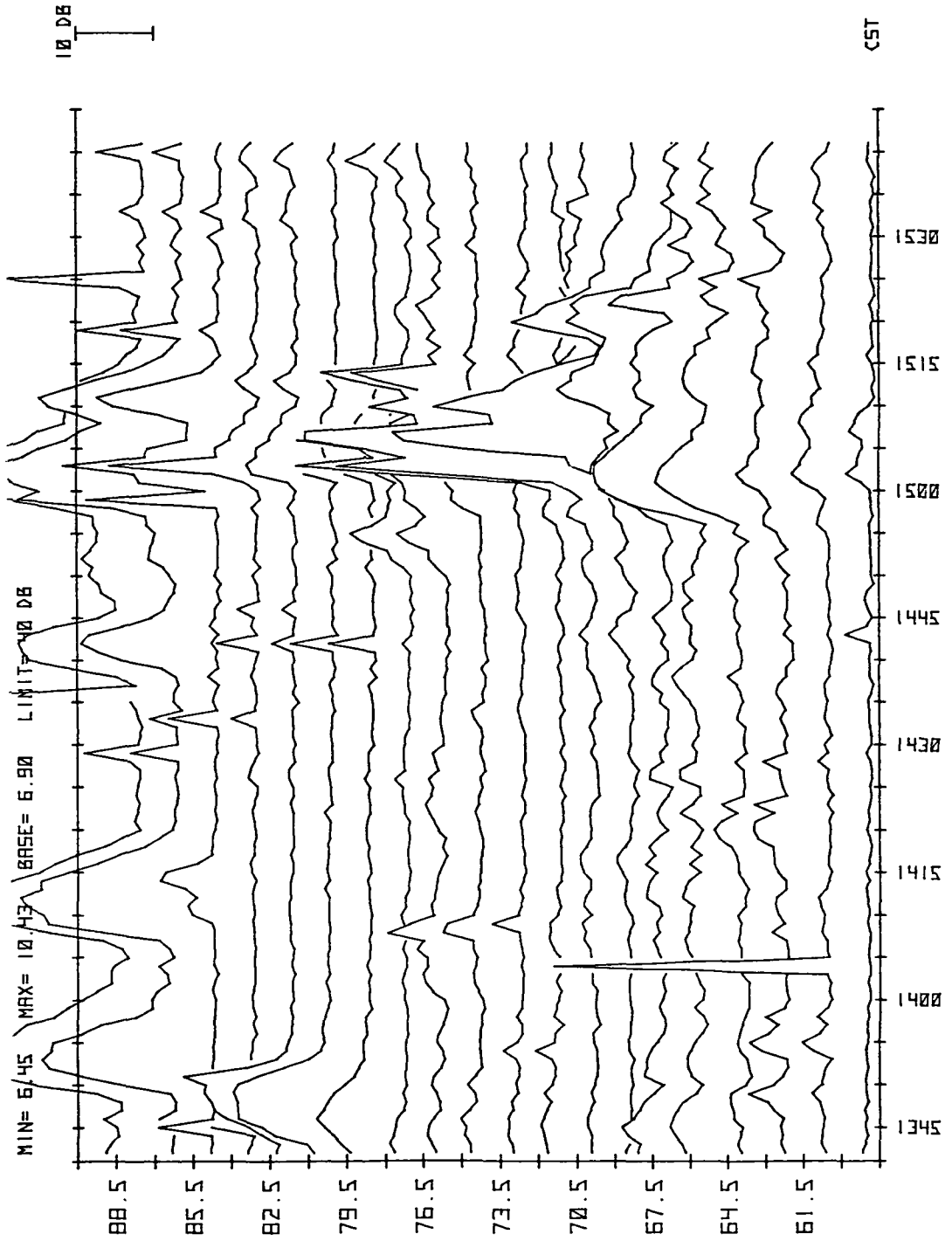

Figure 5.13 Coherent scattered power from 60-90 km over Urbana, beginning at 1342 CST, May 21, 1980.

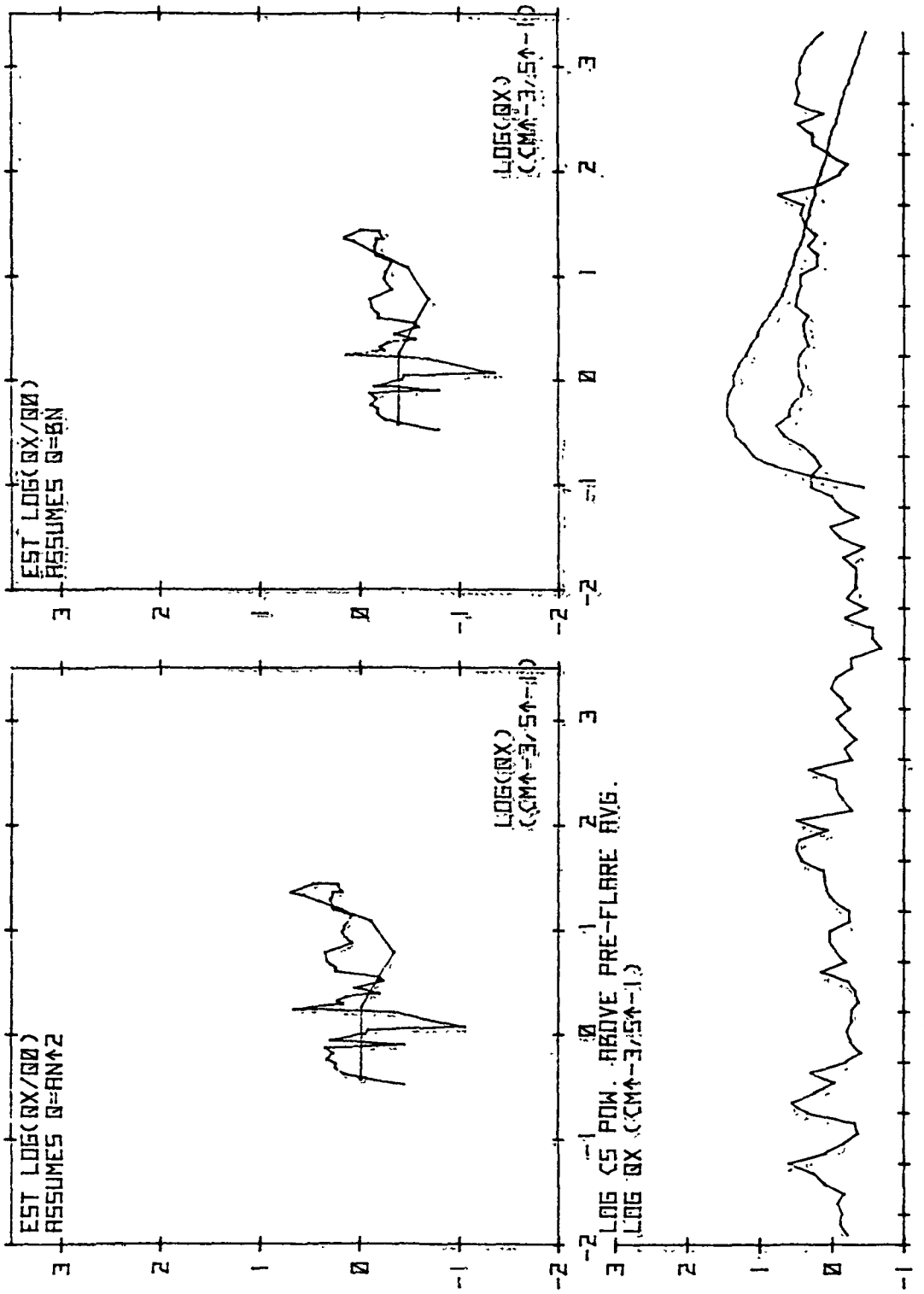

Figure 5.14 Flare-time scattered power enhancement and estimated electron production rate q_x due to flare X-rays at 63 km for the May 21, 1980 event.

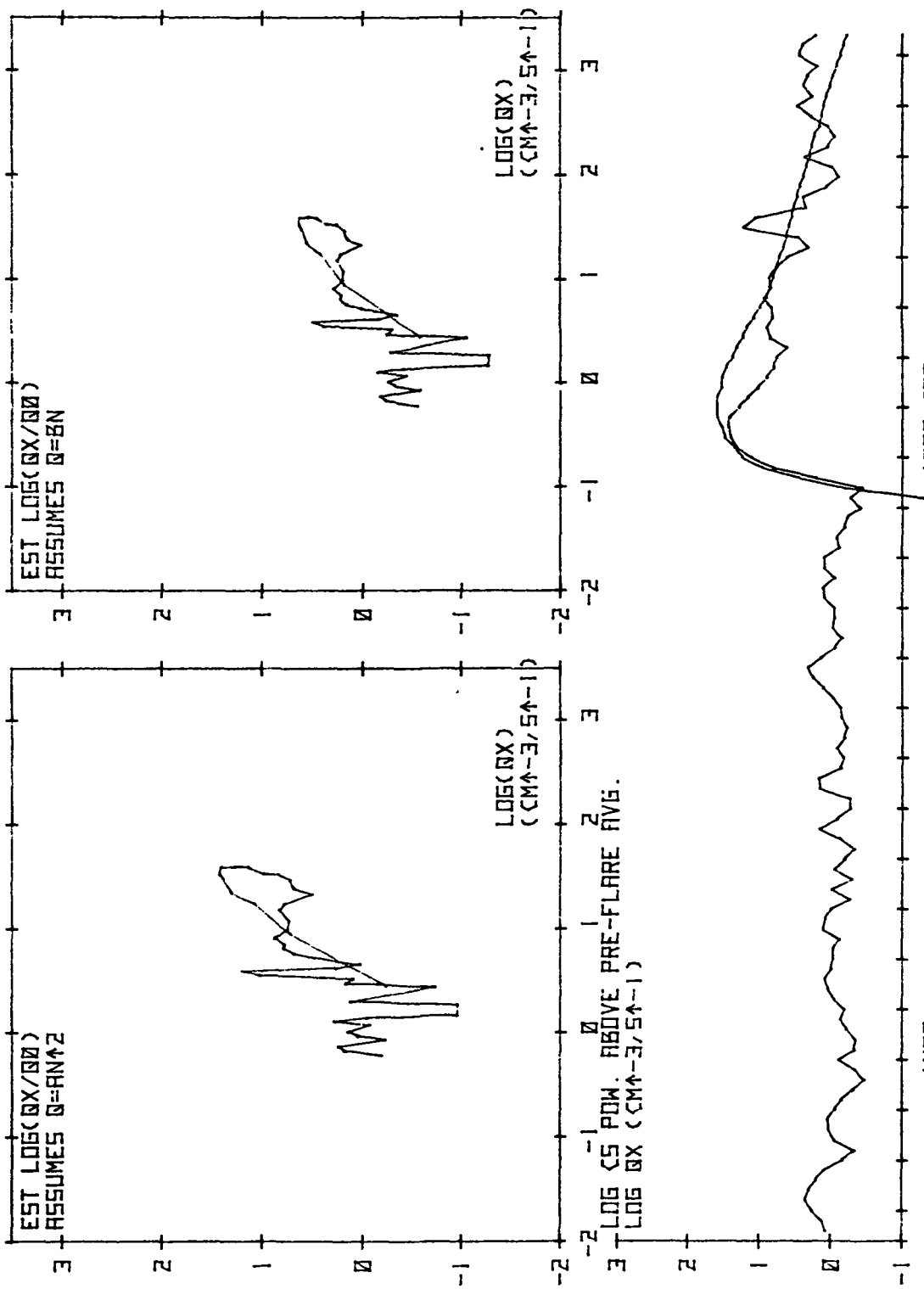

Figure 5.15 Flare-time scattered power enhancement and estimated electron production rate q_x due to flare X-rays at 66 km for the May 21, 1980 event.

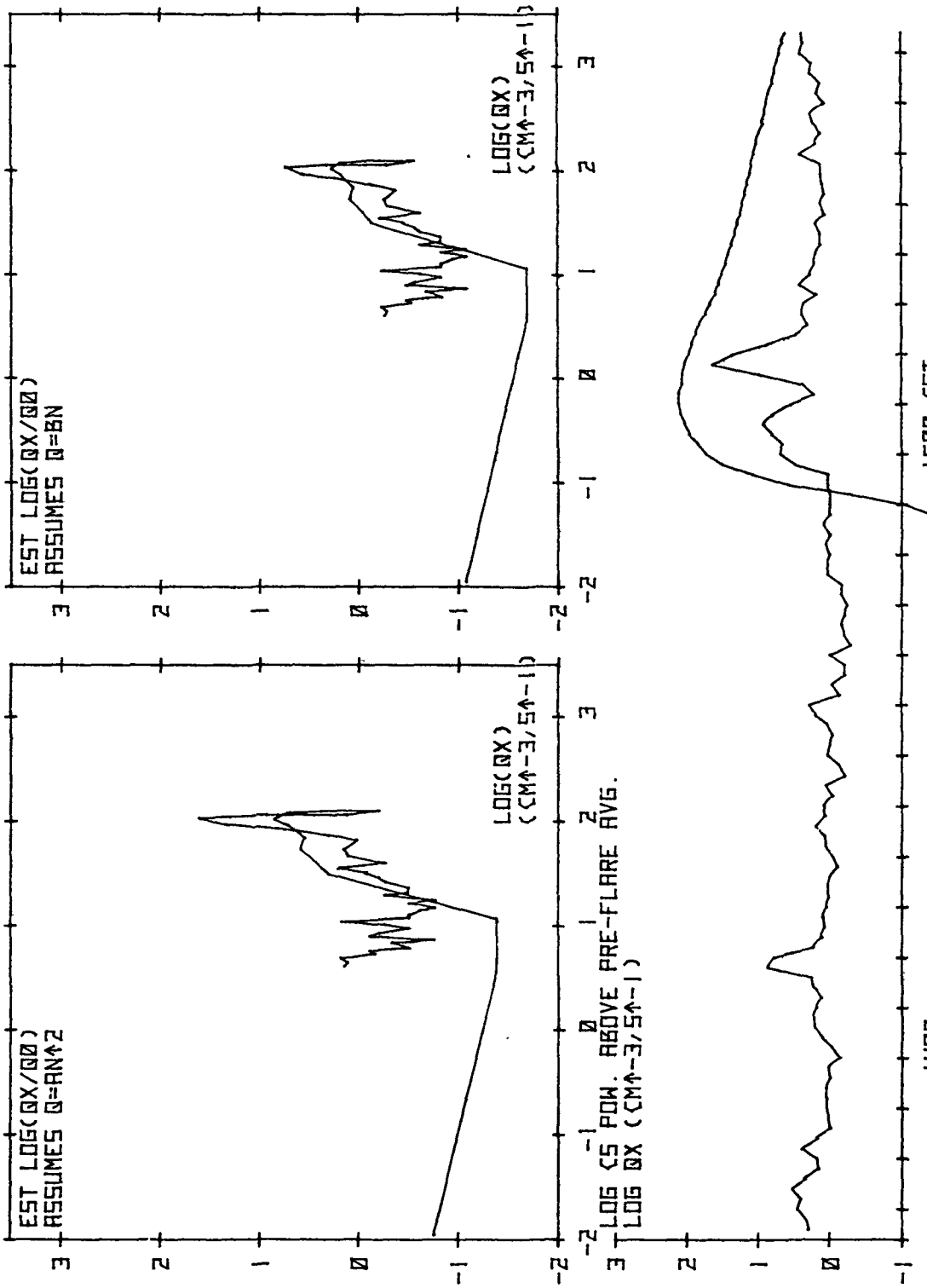

Figure 5.16 Flare-time scattered power enhancement and estimated electron production rate q_x due to flare X-rays at 75 km for the May 21, 1980 event.

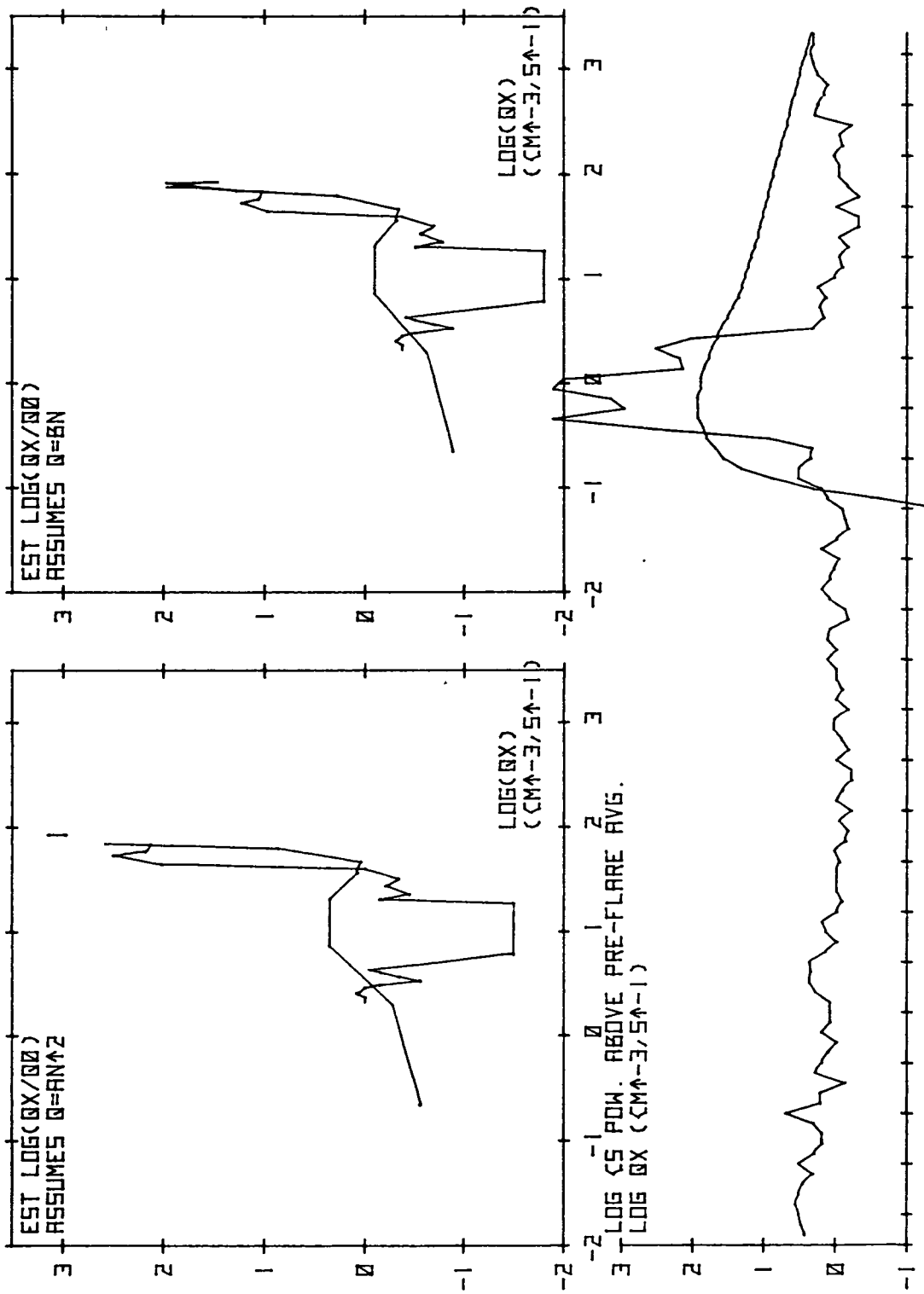

Figure 5.17 Flare-time scattered power enhancement and estimated electron production rate q_x due to flare X-rays at 72 km for the May 21, 1980 event.

Figure 5.18, but there is a problem. There seems to be an additional source of background noise beginning at about the middle of the flare to the end of the record. The astronomical radio source Cygnus A crosses the meridian at about 1120 CST on January 27, and is known to pass through the beam of the Urbana radar; this may account for the additional noise. Since the noise appears to exist at all altitudes, we may estimate its strength by the minimum power received at any given time; this is a much less reliable estimate of noise than the estimate of constant background noise which we usually subtract from data, since it is estimated for only one minute. However, with this modification, the analysis seems to work: the plots of q_x enhancements are shown in Figures 5.19 and 5.20. The relationship between q and N appears to be quadratic at 64.5 km, either quadratic or linear at 61.5 km. Altitudes showing delayed effects are 67.5-69 km; altitudes showing no effect are 70.5-72 km, and altitudes above about 78 km.

The flare of June 2, 1982 was large (0.1-0.8 nm flux of $1x10^{-4}$ watts/meters^2), and occurs at the beginning of a data record. Therefore, a period after the flare, from about 55 to 70 minutes after the start of the record, was chosen for the average base power P_0. Some form of interference corrupts the data from a few minutes at all altitudes, but the response is clearly seen, and large; the enhancements of scattered power at atitudes 70.5-76.5 are very strong, and start after the q_x enhancement, and end much sooner, similar to the response on May 21, 1980, from 69-72 km. A rough $q = \alpha N^2$ relationship may be responsible for the enhancements found at 61.5 km and 67.5 km (see Figures 5.22 and 5.23).

October 14, 1981 (Figure 5.24) shows a quadratic q vs N relationship at 76.5-79.5 km (Figure 5.25). The scattered power from around 69 km peaks earlier and decays more sharply than the estimated $q_x(t)$ (Figure 5.26).

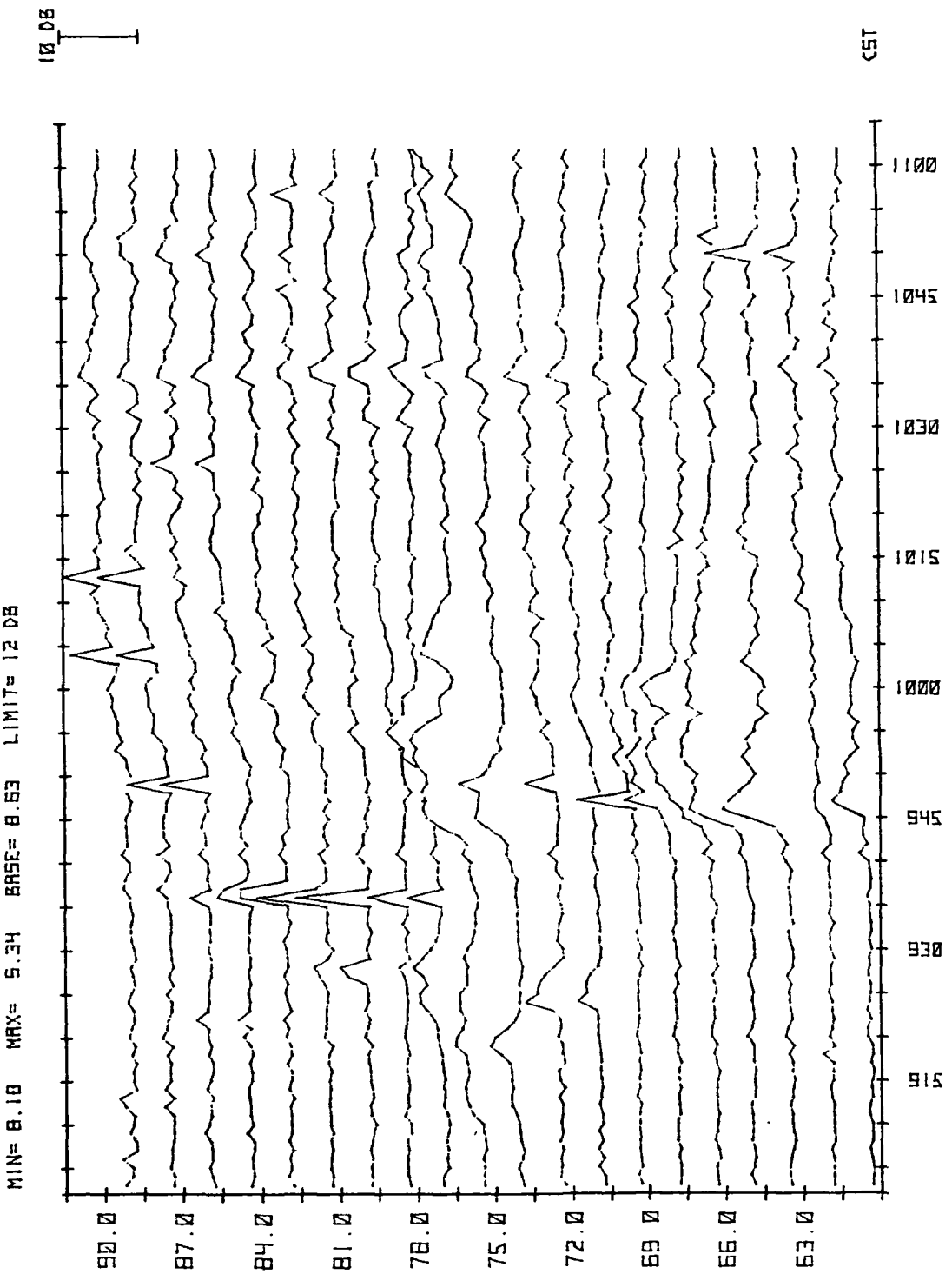

Figure 5.18 Coherent scattered power from 60-90 km over Urbana, beginning at 0903 CST, January 27, 1981.

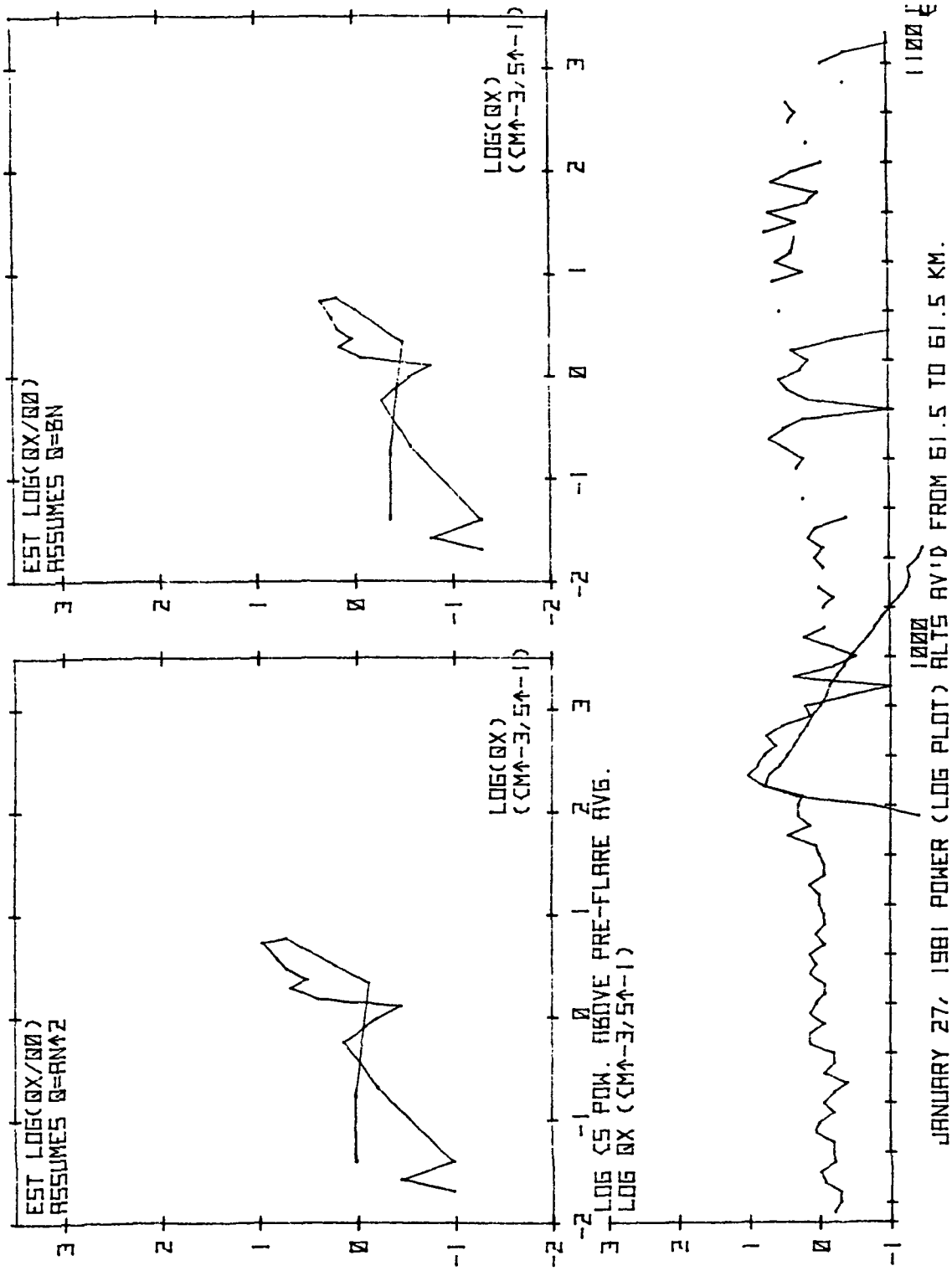

Figure 5.19 Noise-corrected flare-time scattered power enhancement and estimated electron production rate q_X due to flare X-rays at 61.5 km for the January 27, 1981 event.

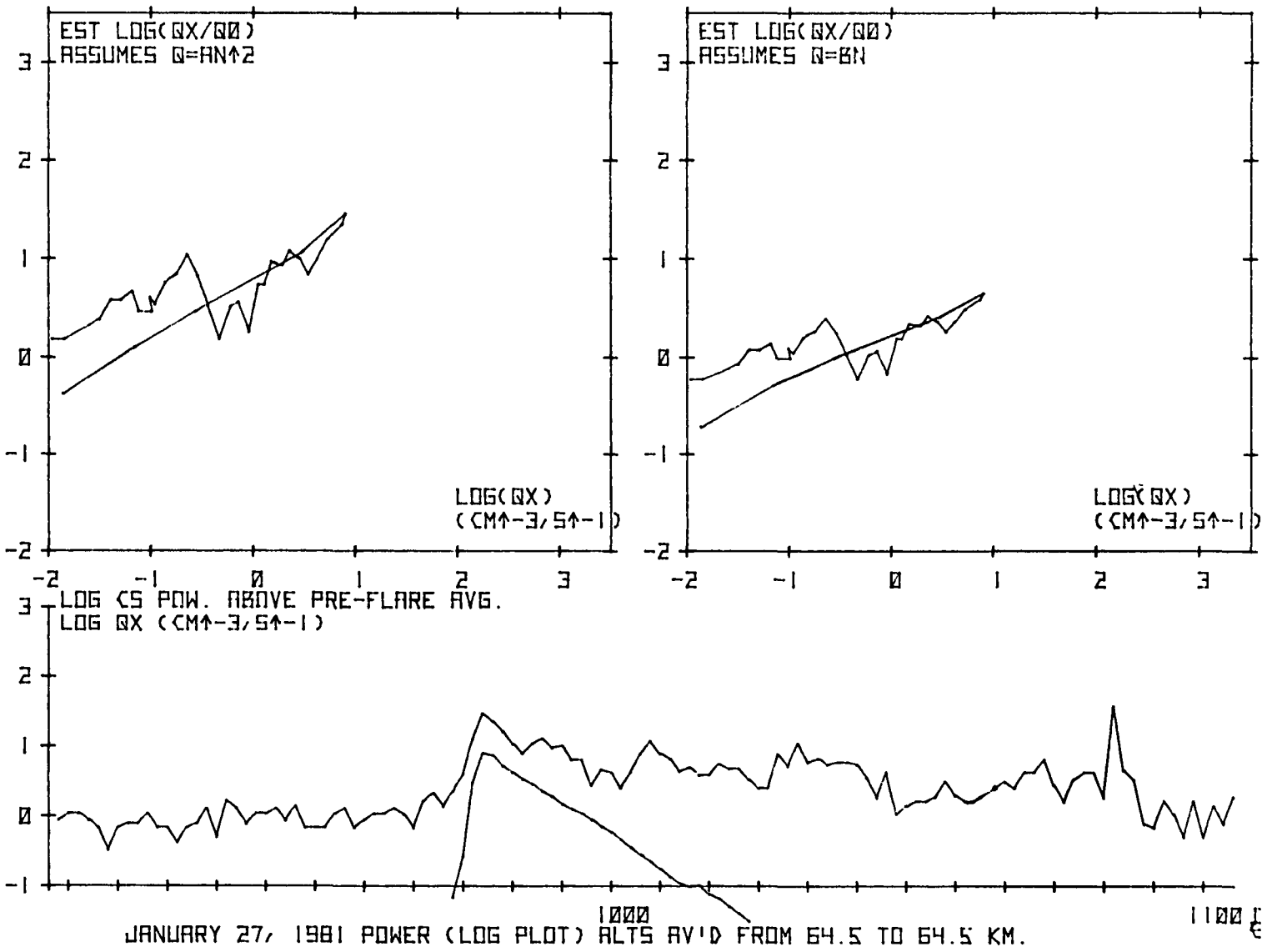

Figure 5.20 Noise-corrected flare-time scattered power enhancement and estimated electron production rate q_x due to flare X-rays at 64.5 km for the January 27, 1981 event.

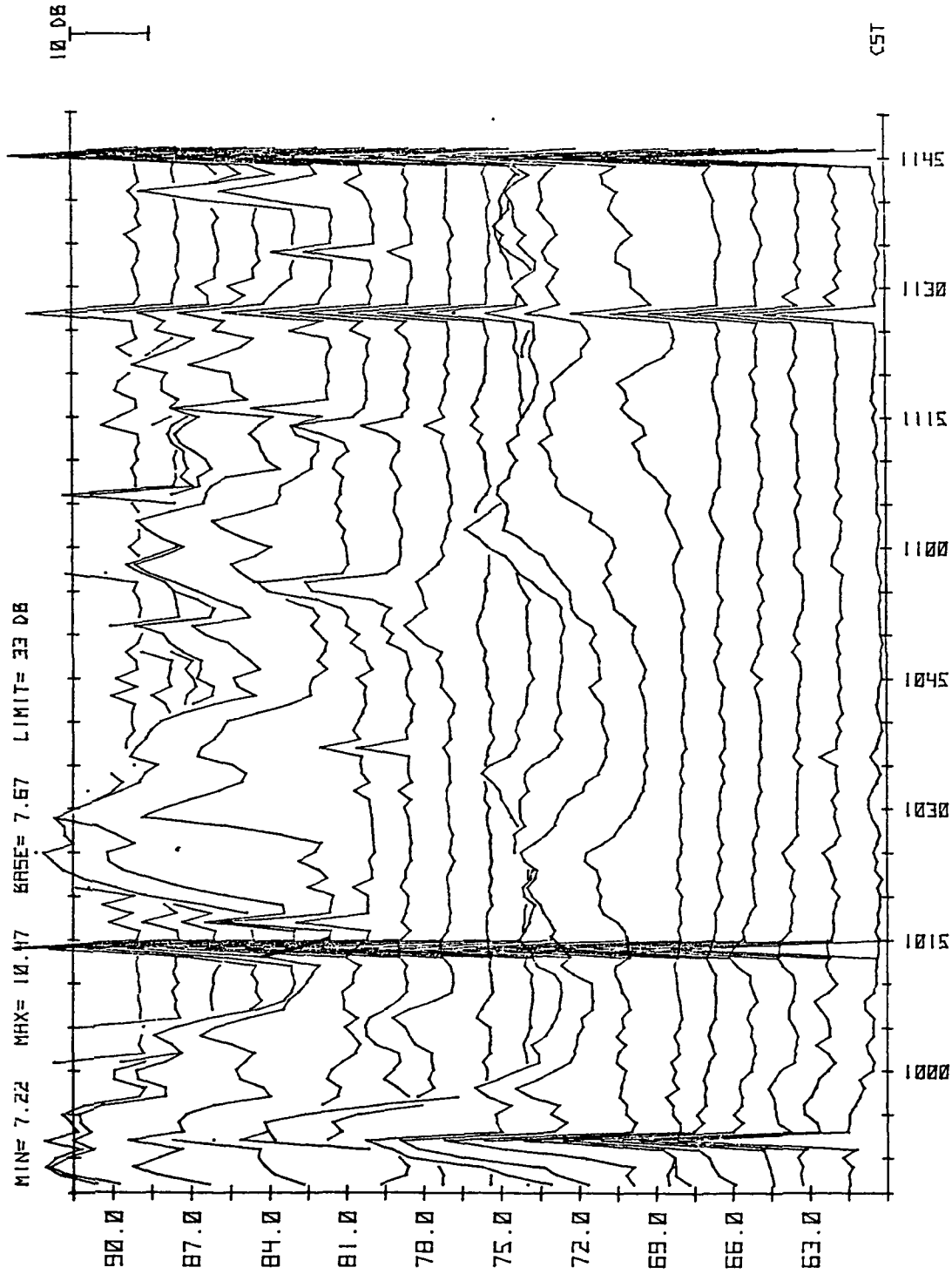

Figure 5.21 Coherent scattered power from 60-90 km over Urbana, beginning at 0917 CST, June 2, 1982.

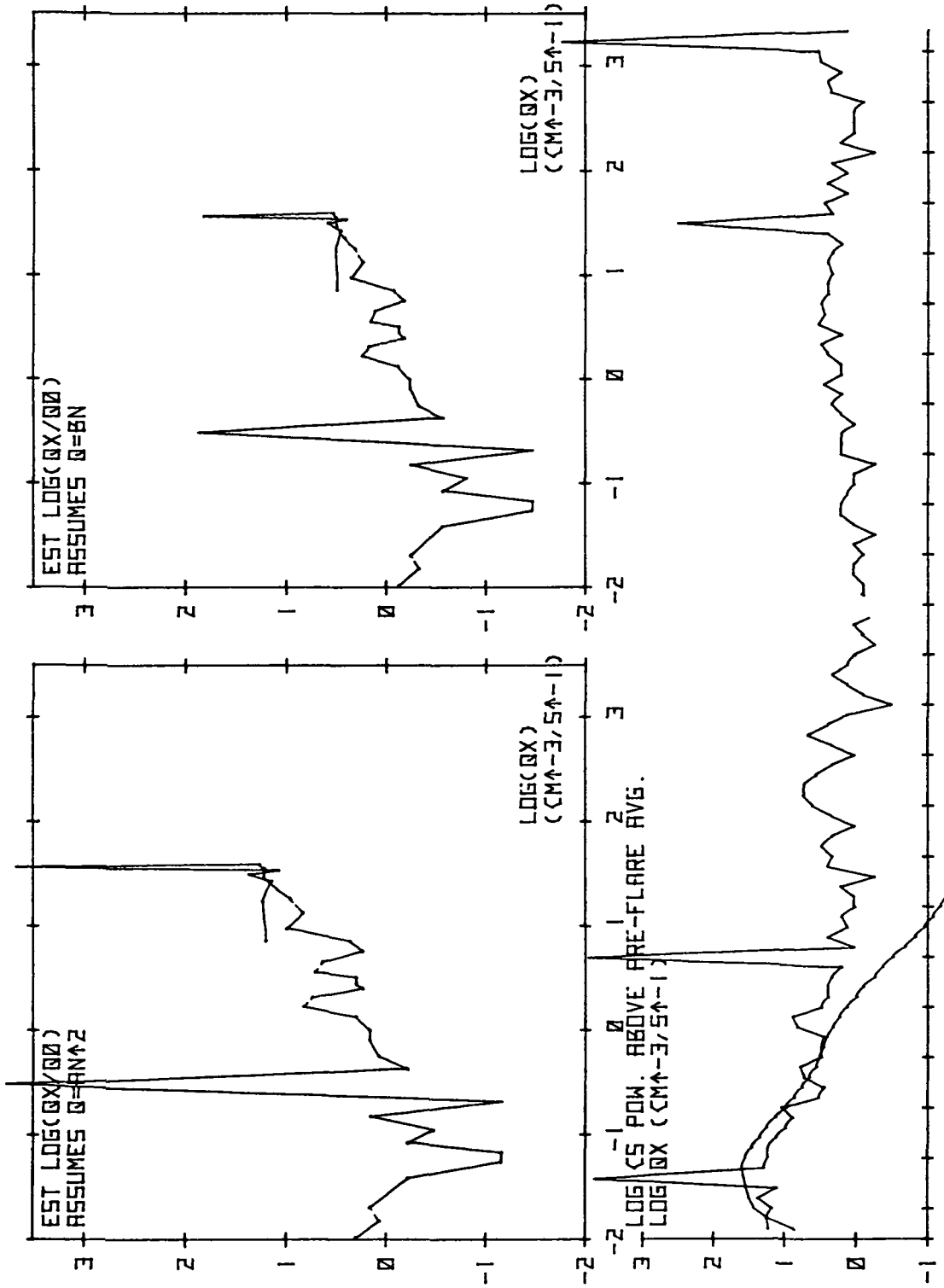

Figure 5.22 Flare-time scattered power enhancement and estimated electron production rate q_x due to flare X-rays at 61.5 km for the June 2, 1982 event.

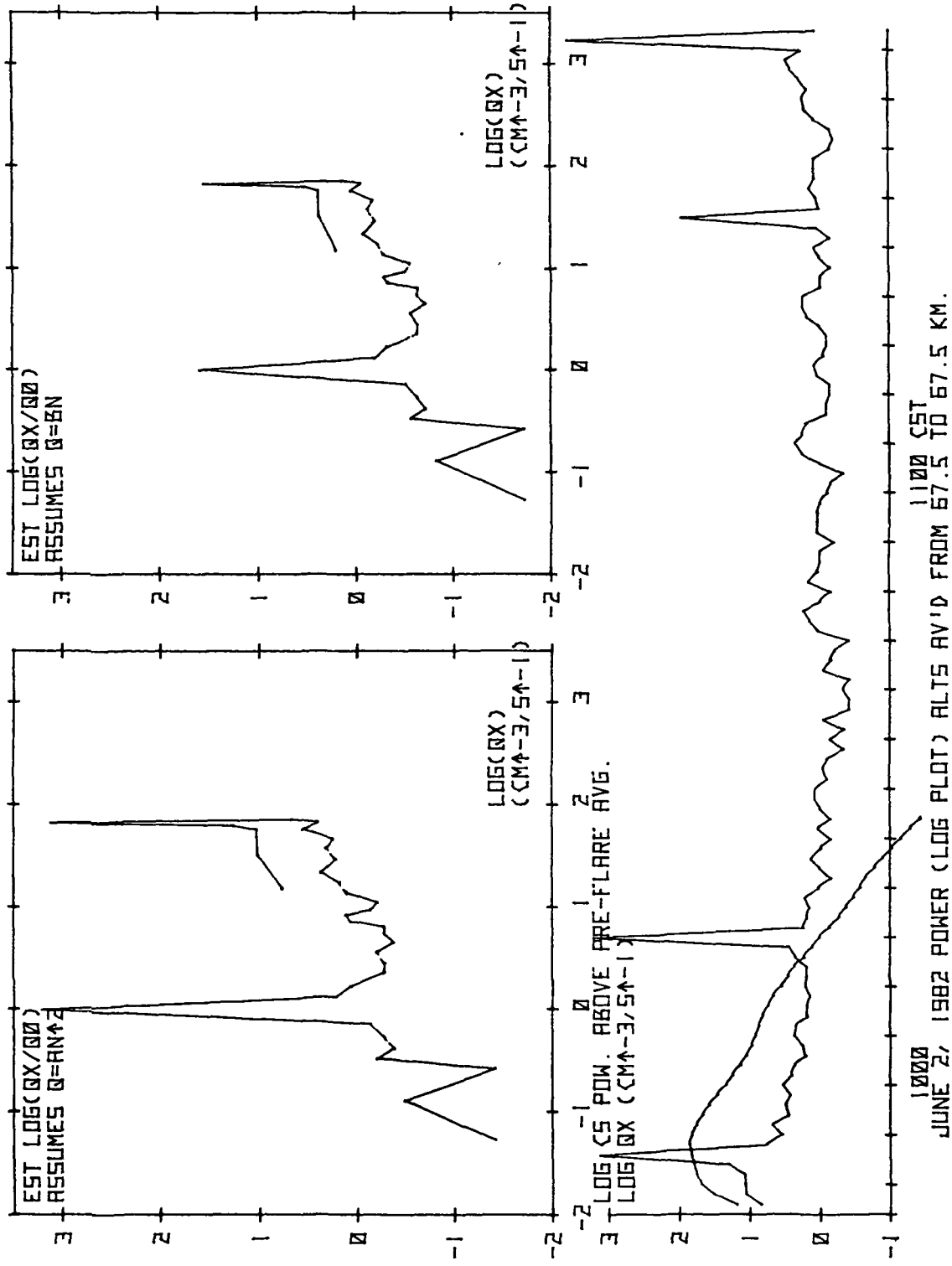

Figure 5.23 Flare-time scattered power enhancement and estimated electron production rate q_x due to flare X-rays at 67.5 km for the June 2, 1982 event.

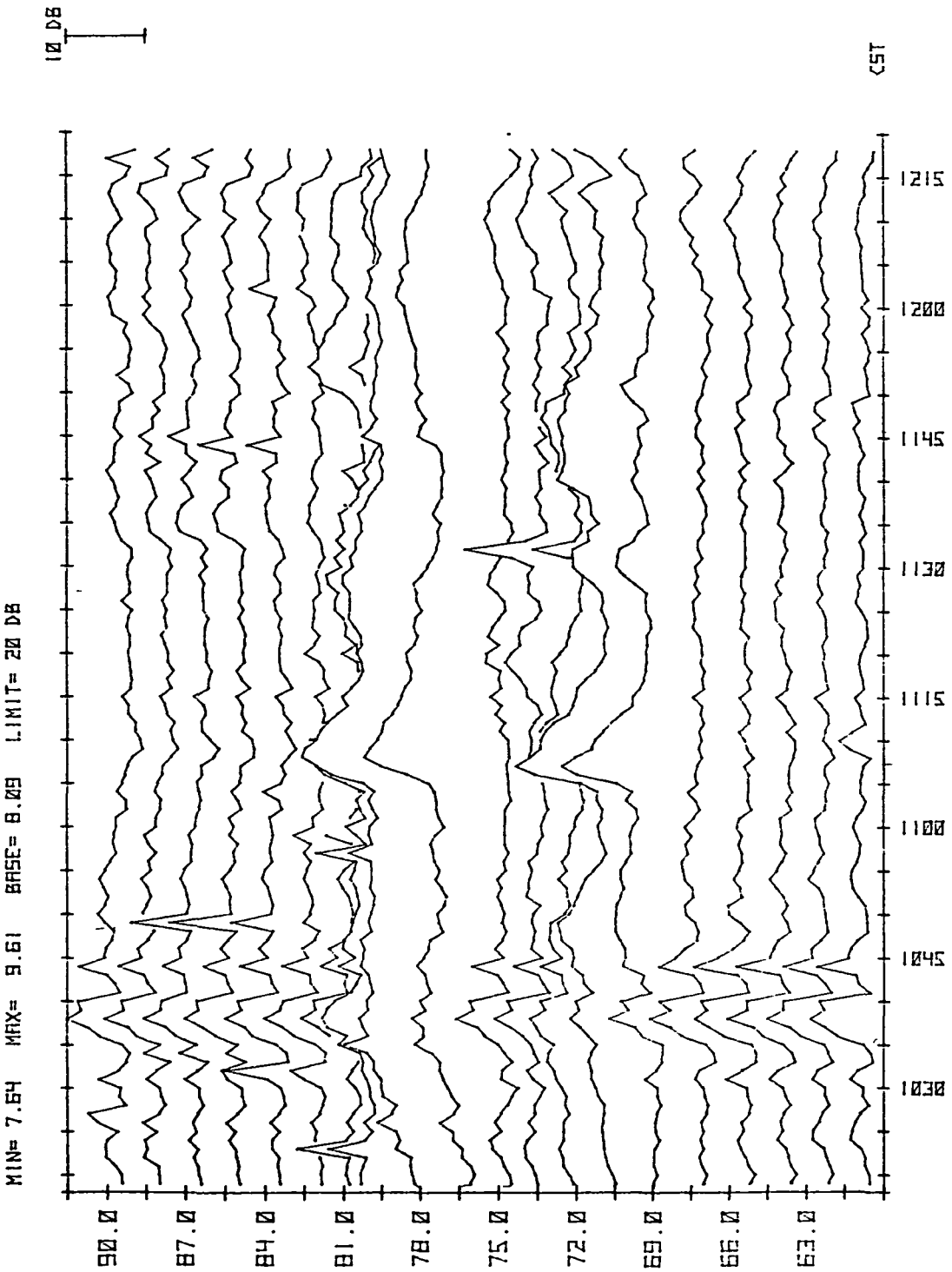

Figure 5.24 Coherent scattered power from 60-90 km over Urbana, beginning at 1019 CST October 14, 1981.

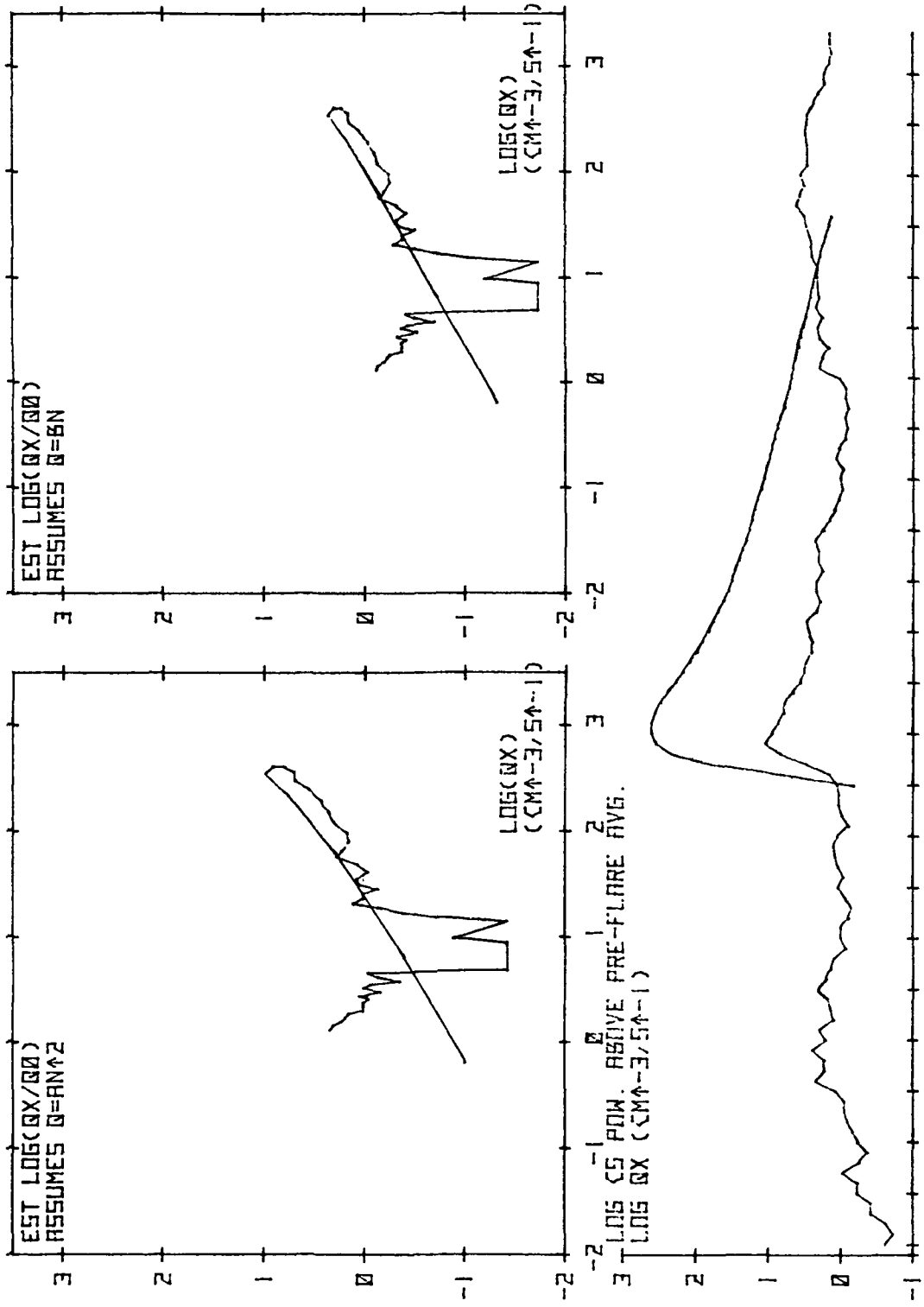

Figure 5.25 Flare-time scattered power enhancement and estimated electron production rate q_x due to flare X-rays at 76.5 km for the October 14, 1981 event.

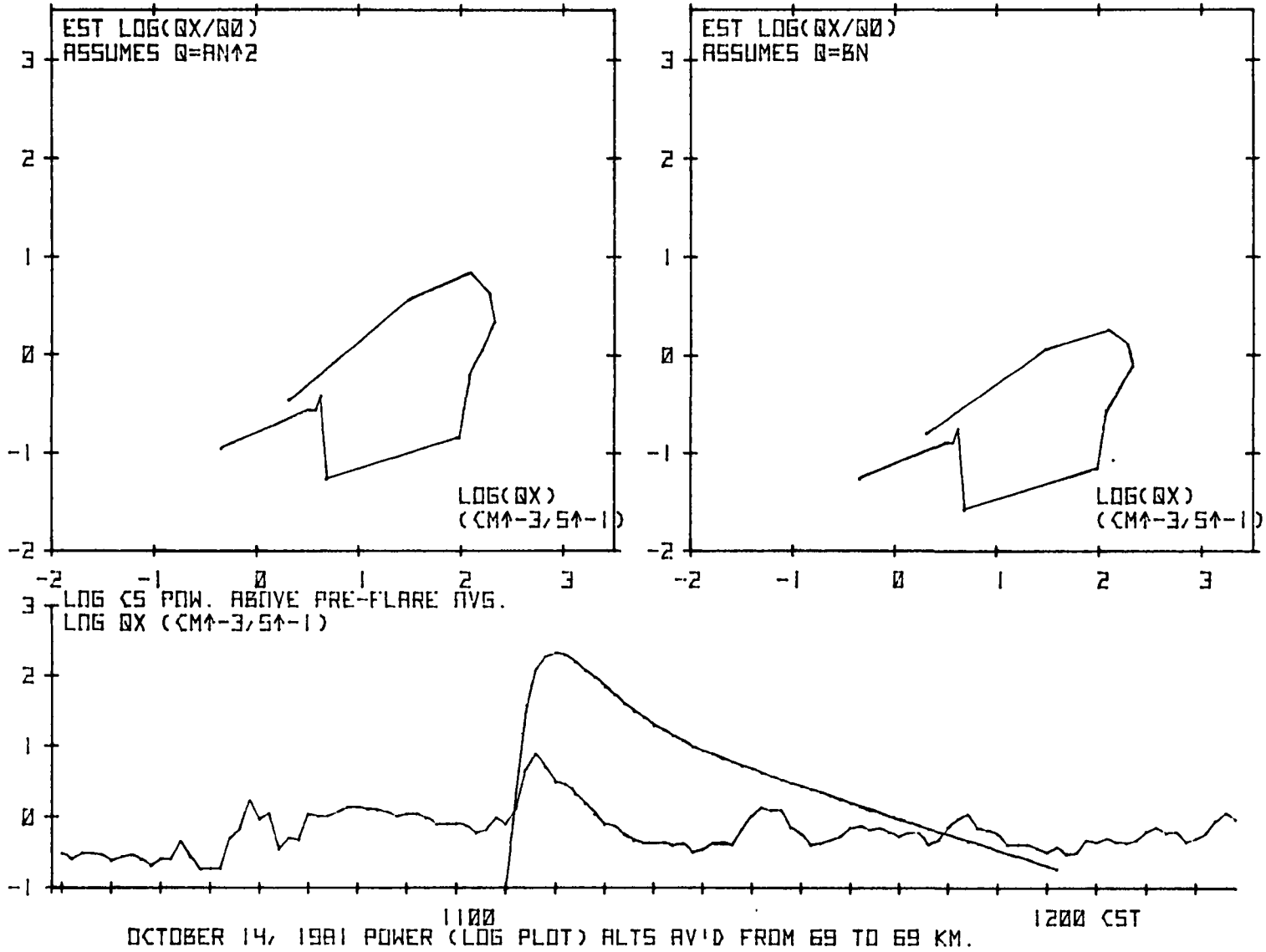

Figure 5.26 Flare-time scattered power enhancement and estimated electron production rate q_x due to flare X-rays at 69 km for the October 14, 1981 event.

Several additional flares cause enhancements in scattered power, but do not allow the most complete form of analysis.

March 31 1982 shows only delayed enhancements at altitudes at or below 72 km, with the time delay increasing with decreasing altitude (flare peak is about 1625 CST). No enhancement is detectable above about 72 km (Figure 5.27).

The flares of May 28, 1980 and May 5, 1981 show only small power enhancements in scattered power and therefore are not well suited to the analysis technique described above, despite the fact that both flares are large (0.1-0.8 nm flux of about 1.2×10^{-4} watts/meter^2). However, it is noteworthy that both these flare events resulted in a large increase in the number of altitudes which yielded valid line-of-sight velocity data. The number of altitudes showing velocity data increased for the May 28 event from a preflare range of about 6-11 to 14. For the May 5 event the number increased from about 7 to 16.

The flare of April 11, 1978 was very large (0.1-0.8 nm flux of 2×10^{-4} watts/meter^2) and of very long duration, on the order of three hours. The flare had already commenced when the Urbana radar began collecting data that day (Figure 5.28). By the time the flare X-ray level fell to negligible levels, the base scattered power level must have changed considerably, due to the change in zenith angle over that time span. Further, the method of estimating noise power as the minimum for the record does not seem to apply here, due to the size of the electron density enhancement all through the record. This prohibits using a near-in-date quiet day for an estimate of the preflare average scattered power. Therefore, no reliable estimate of P_0 can be formed with which to compare the enhanced levels.

The flares of August 3, 1981; August 13, 1983; and August 21, 1983,

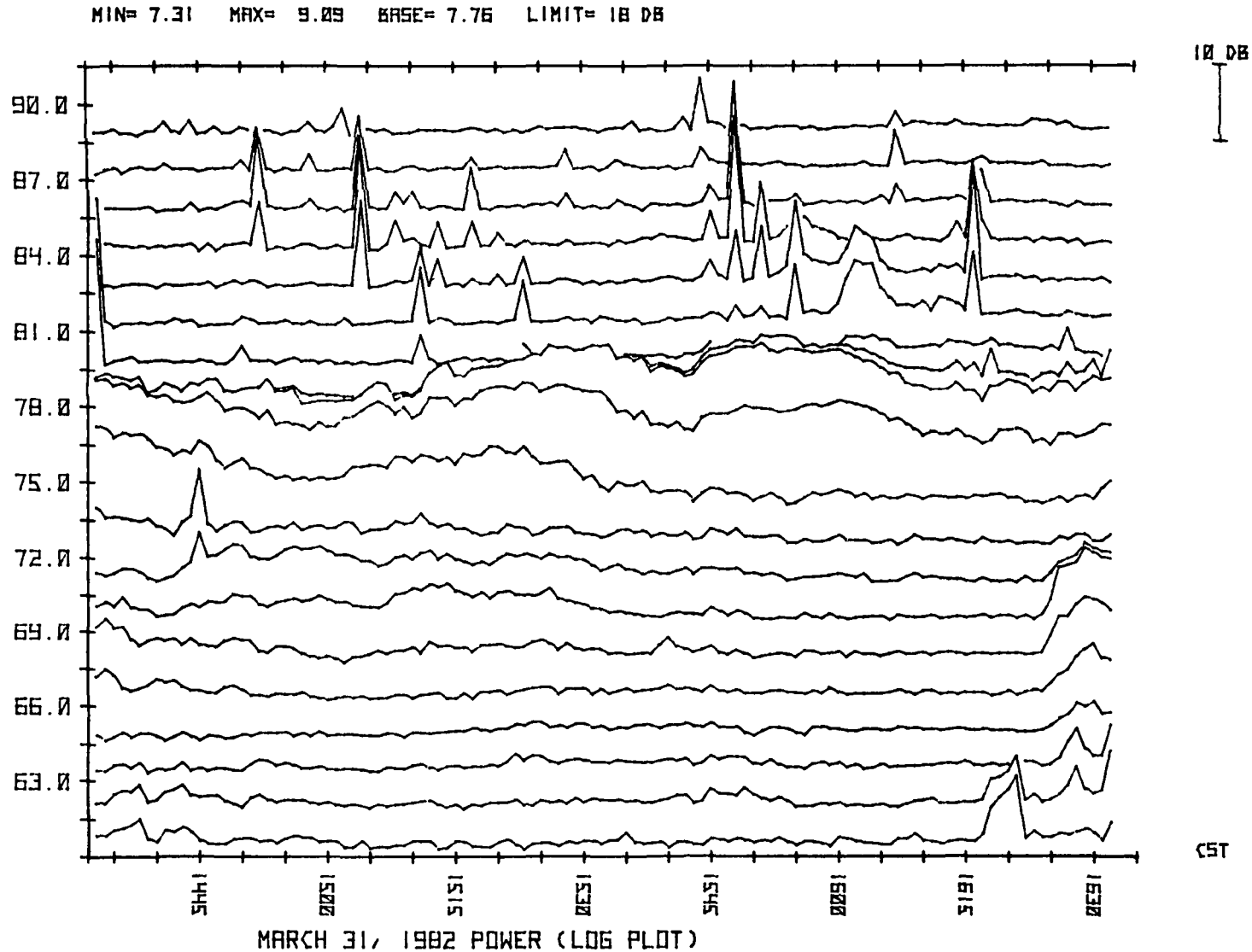

Figure 5.27 Coherent scattered power from 60-90 km over Urbana, beginning at 1433 CST, March 31, 1982.

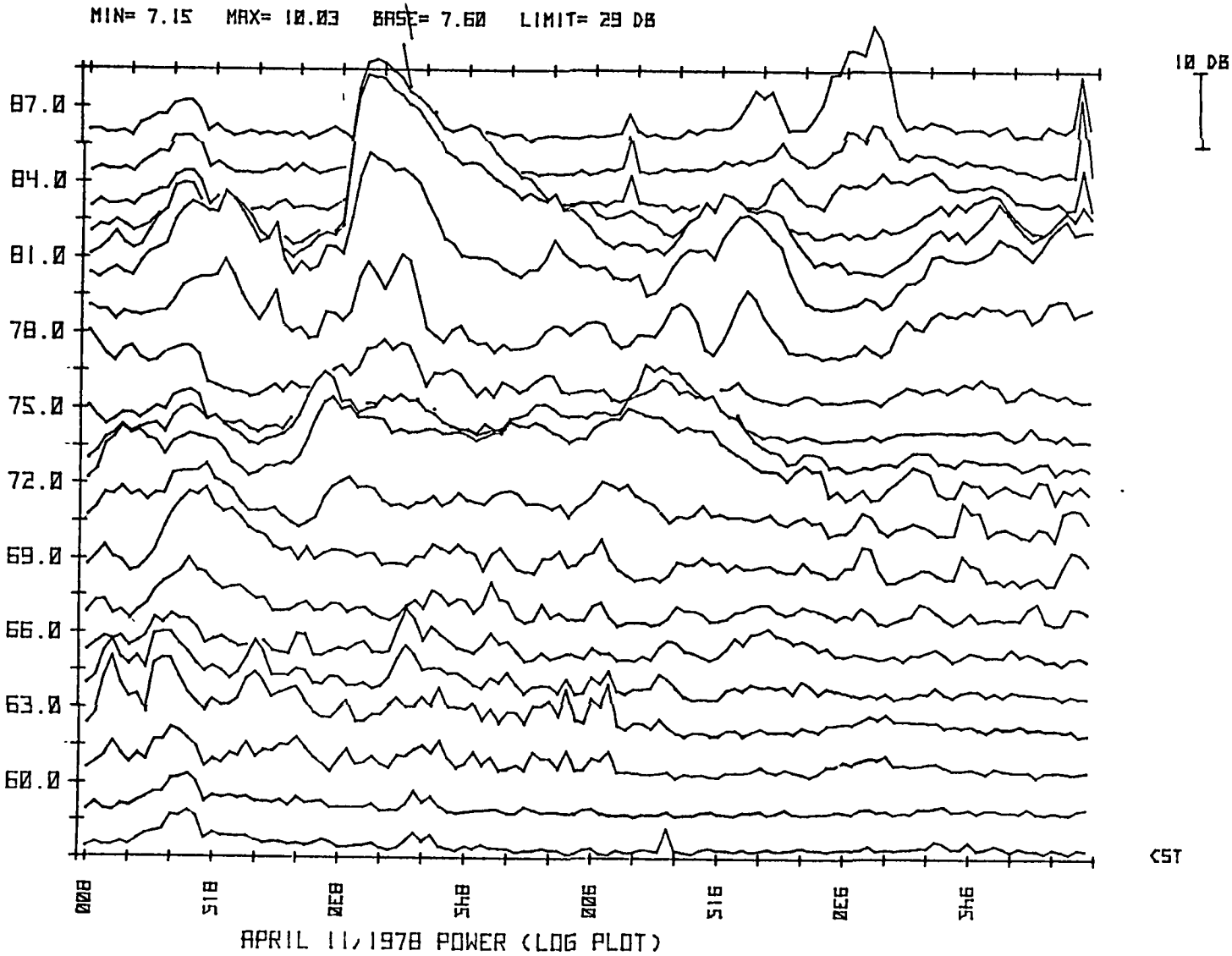

Figure 5.28 Coherent scattered power from 60-90 km over Urbana, beginning at 0800 CST, April 11, 1978.

show a typical onset and decay at some altitudes, suggesting a quadratic or linear equilibrium relationship between q and N (Figures 5.29, 5.30, and 5.31). However, detailed plots of the X-ray detector outputs for these times have not been obtained, so no detailed analysis has been performed.

5.3 Comparisons of different events

The regions showing each type of flare-time enhancement for each flare listed above are shown in Figure 5.32. Note that equilibrium enhancements above a steady baseline are confined to the region below 80 km. There seems to be some seasonal variation evident in this plot, for example a tendency for the delayed effect predicted by Thomas et al. (1973) to happen in the fall and winter, but not the spring or summer. However, the diversity of zenith angles and sizes of flares makes such comparisons inconclusive.

An even more pronounced effect is the dependence of the altitude range which shows any sort of power enhancement upon zenith angle. There appears to be a maximum altitude which shows enhancements, and this maximum altitude descends with increasing zenith angle. Chapman layers tend to rise with increased zenith angle, so this does not appear to be a simple photochemical effect; rather, this may be an indirect effect of a dependence of turbulent layer strength on zenith angle at a given altitude.

Estimates of q_0 for each flare are shown in Figure 5.33. These group roughly according to zenith angle. The smaller angles correspond to larger q_0 values, as expected. The effect of zenith angle on q_0 appears to swamp any seasonal effect.

The plot of Mathews (1984) (Figure 2.4) may also be analyzed somewhat and compared with these results. After reducing this plot to numerical values by hand, and estimating q_x by the same means used above, we can plot q_x vs. N directly, to test for linear vs. quadratic relationships. In

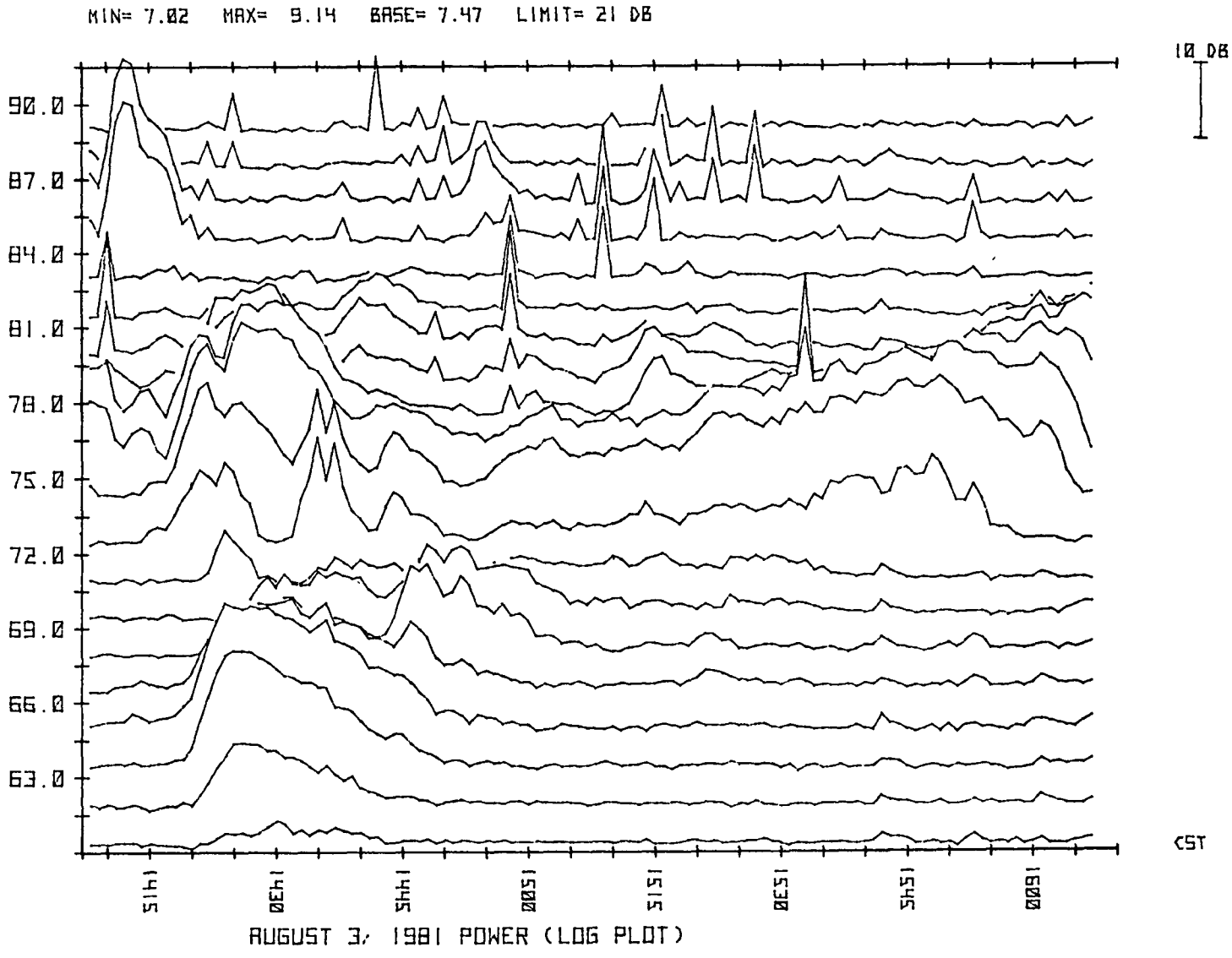

Figure 5.29 Coherent scattered power from 60-90 km over Urbana, beginning at 1408 CST, August 3, 1981.

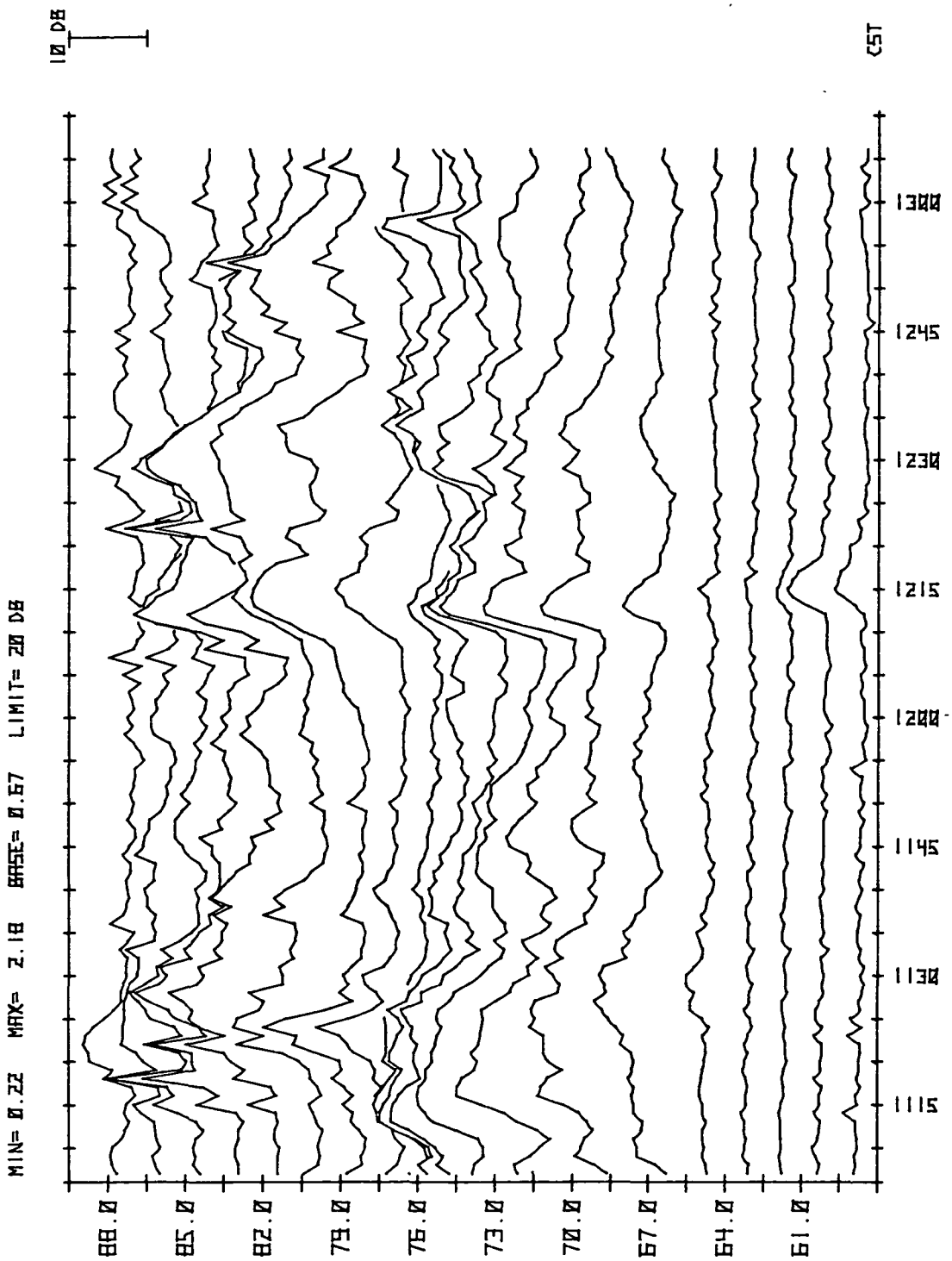

Figure 5.30 Coherent scattered power from 60-90 km over Urbana, beginning at 1107 CST, August 13, 1983.

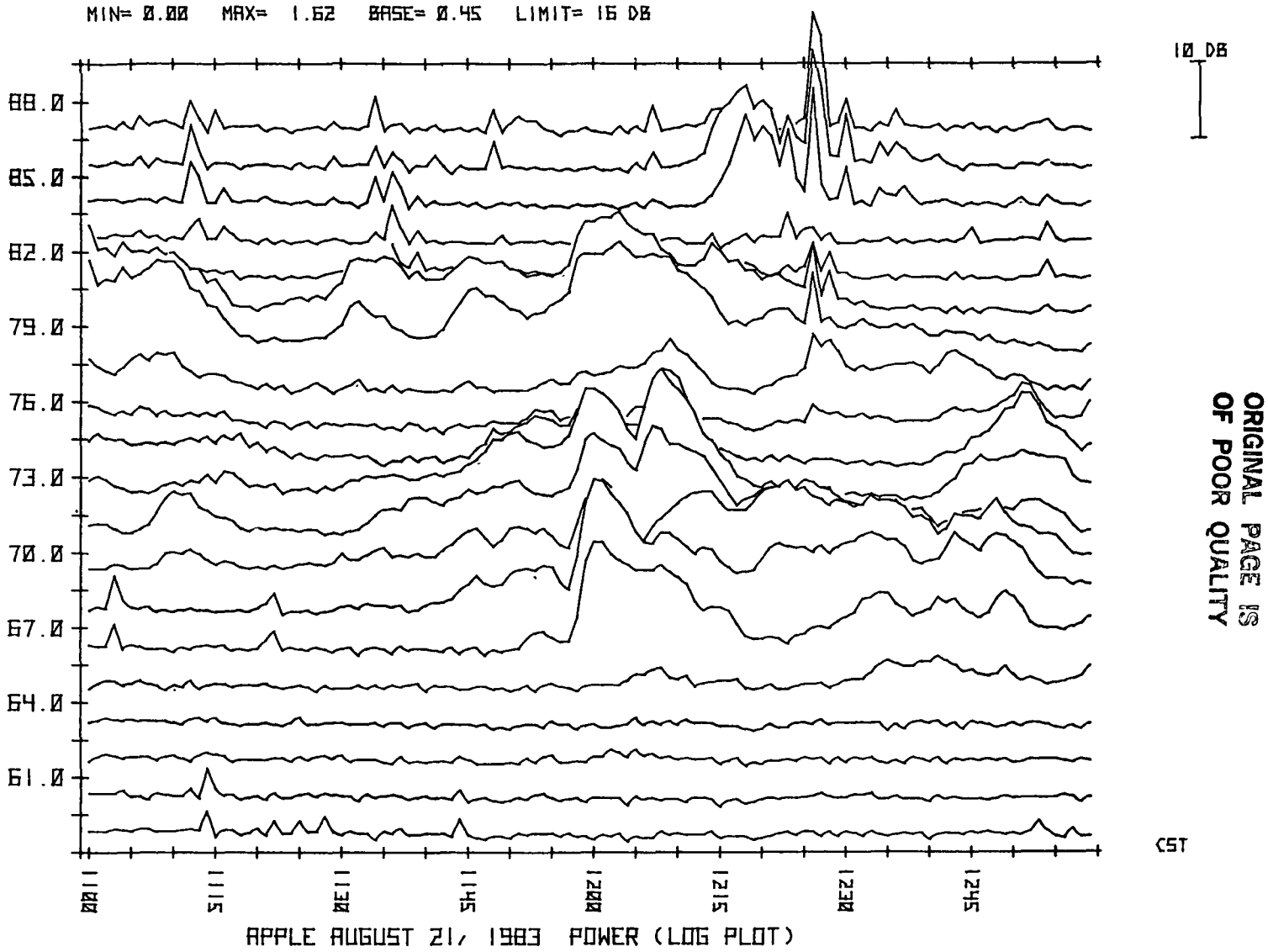

ORIGINAL PAGE IS
OF POOR QUALITY

Figure 5.31 Coherent scattered power from 60-90 km over Urbana, beginning at 1100 CST, August 21, 1983.

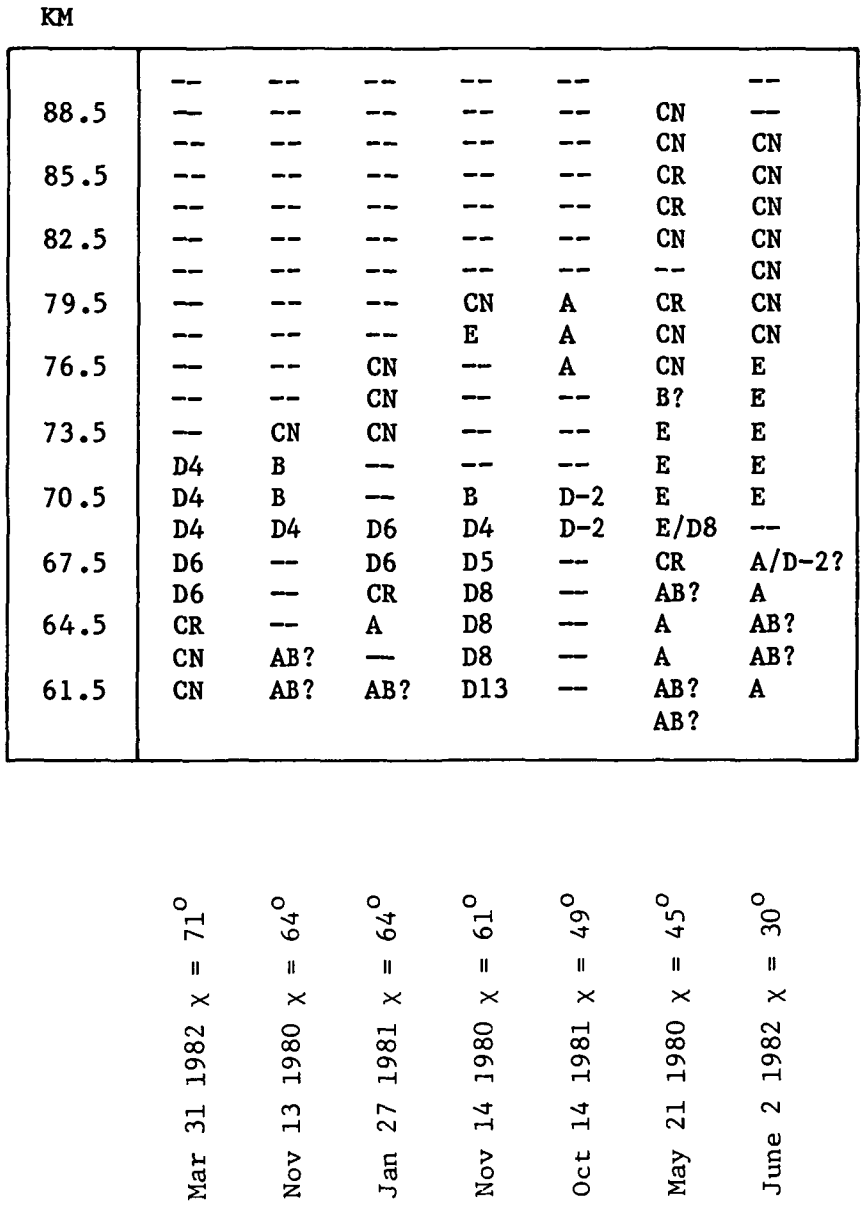

Figure 5.32 Types of response at each mesospheric altitude for each flare: A) $q = \alpha N^2$. B) $q = \beta N$. AB?) probably A or B, but plots are ambiguous. D#) Delayed effect, with peak power following q by # minutes. E) Extreme response, power increase greater than cases A or B. CN) coincident flare time power response, but unable to fit A or B model due to comparable nonflare fluctuations in power at that altitude. CR) Coincident response well above nonflare base power, but unable to fit A or B models due to large fluctuations on the order of the one minute sample time. —) no detectable response.

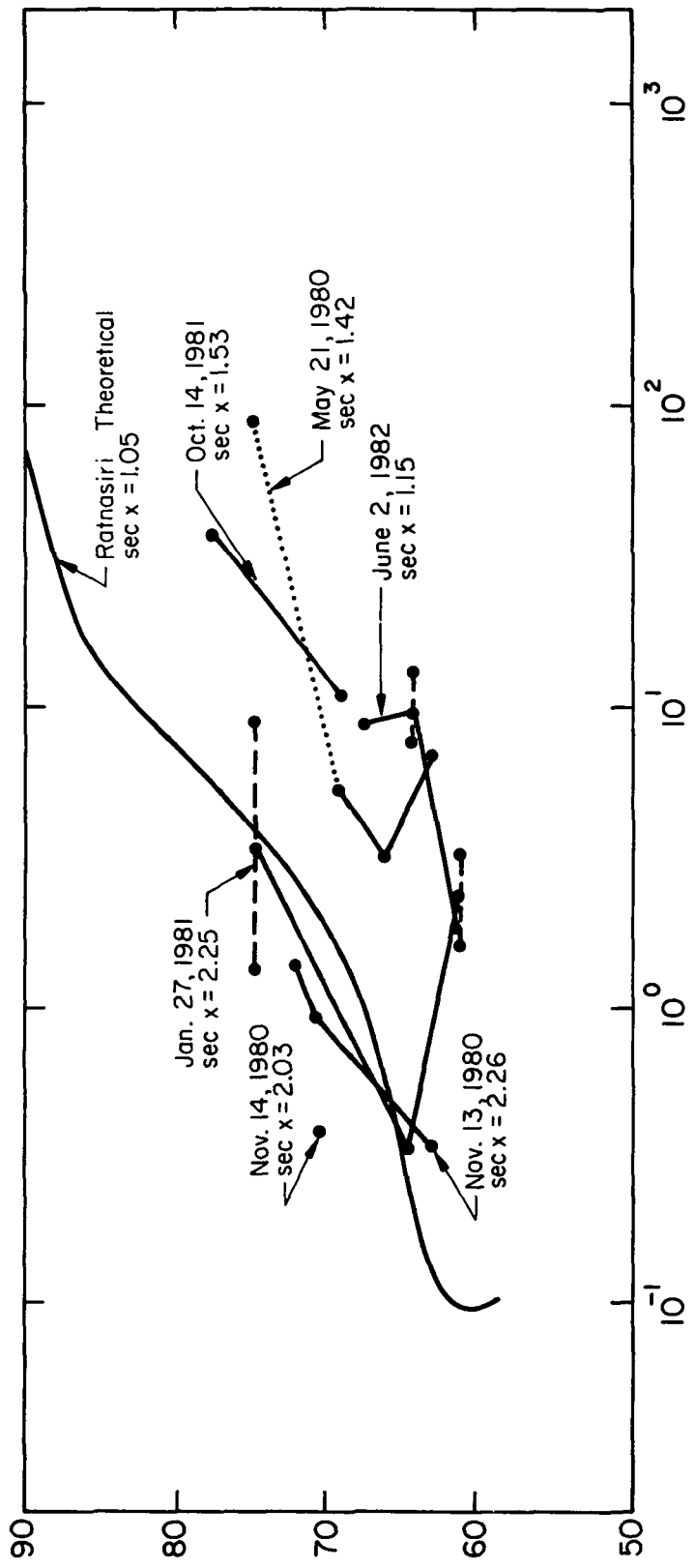

Figure 5.33 Estimates of q_0 made by finding intercept of $\log(q_x)$ vs $\log(q_x/q_0)$ plots with line $\log(q_x) = 0$ for each altitude and flare event which shows type A ($q=\alpha N^2$) or type B ($q=\beta N$) response. Horizontal dashed lines represent the span between the type A estimate of q_0 and type B estimate of q_0 at altitudes where the choice between type A and type B is ambiguous. The estimate of q_0 by Ratnasiri from Figure 3.1, is reproduced for comparison.

this case, N is known directly, both before and during the flare. Therefore, if $q = \alpha N^2$, then

$$q = q_0 + q_x = \alpha N_f^2 = \alpha (N_0 + N_x)^2 \tag{5.9}$$

while

$$q_0 = \alpha N_0^2 \tag{5.10}$$

so that

$$q_x = q - q_0 = \alpha (N_0 + N_x)^2 - \alpha N_0^2 = \alpha(N_f^2 - N_0^2) \tag{5.11}$$

(where N_f is the flare-time value of electron density). Therefore, if we plot N_f^2 vs. q_x the result should resemble a straight line; the slope is α and the intercept is N_0^2.

If, on the other hand, $q = \beta N$, then a similar analysis shows that a plot of q_x vs. N should resemble a line of slope β and intercept N_0.

Figures 5.34 and 5.35 show each kind of plot: it seems that all altitudes between 64 and 79 are governed by quadratic laws. Caution must be used with this result, however: since the data points are only shown for four-minute intervals, the ascending phase of the flare is absent from the analysis. It is conceivable that a nonequilibrium effect could resemble a quadratic equilibrium effect during the decay phase of the flare.

However, although this plot shows a wide spread due to noise, the resemblence is much closer to straight lines for the quadratic relationship at all altitudes than for the linear relationship between q and N.

Also, we may examine the data from Rottger (1983, Figure 2.5). This is the same flare as that examined by Mathews (1984, Figure 2.4), observed from Arecibo at different wavelengths and methods. As with the Urbana data, strong enhancements are only found at a few altitudes, namely 66 km, 70 km, and perhaps 63 km and 72 km. There may also be slight enhancements not confined to layers in the range above 72 km. But it is interesting that the

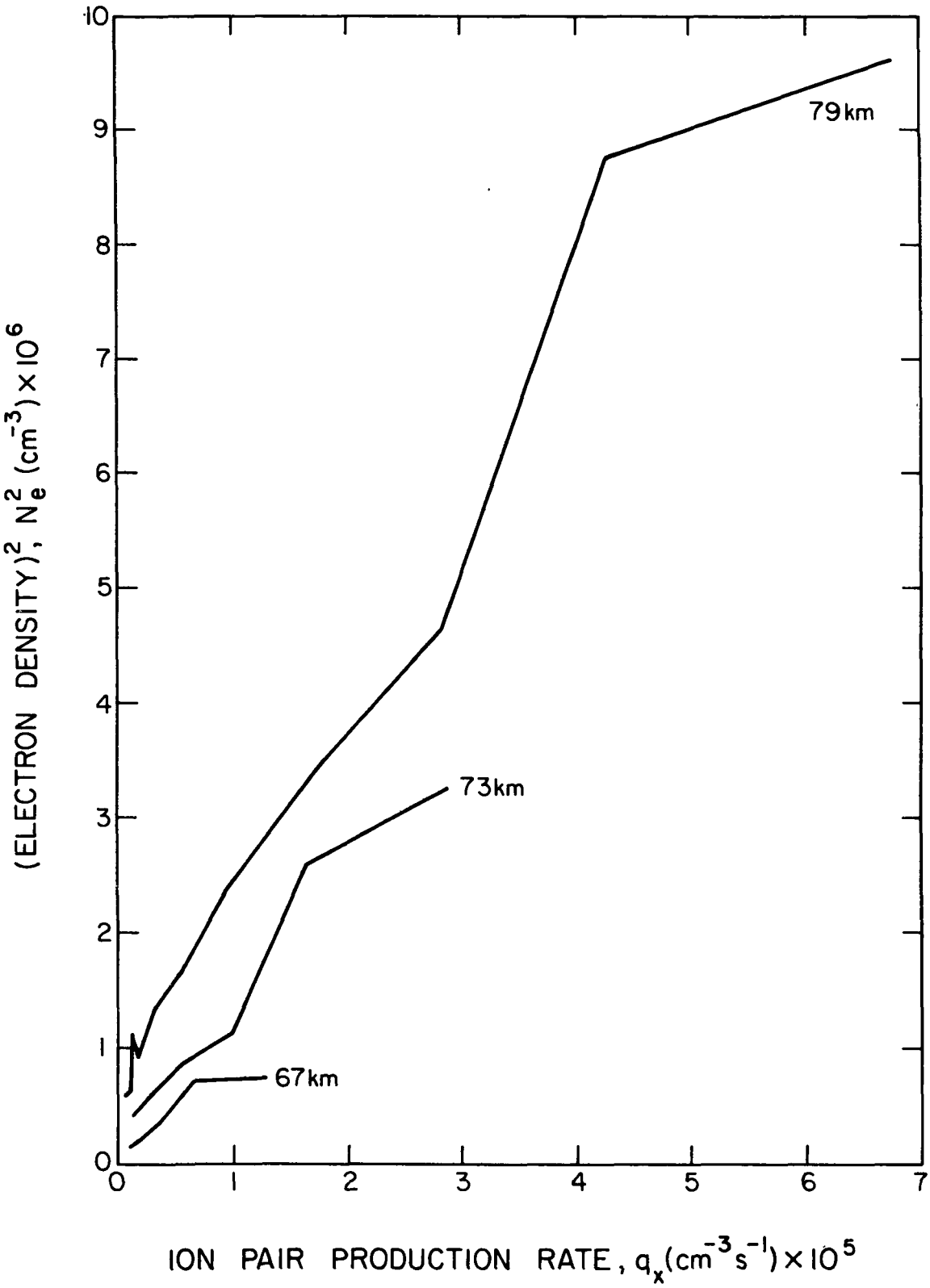

Figure 5.34 Estimated q_x from GOES data vs. incoherent scatter measurement of N_e squared over Arecibo (from Figure 2.4) for flare event of January 5, 1981.

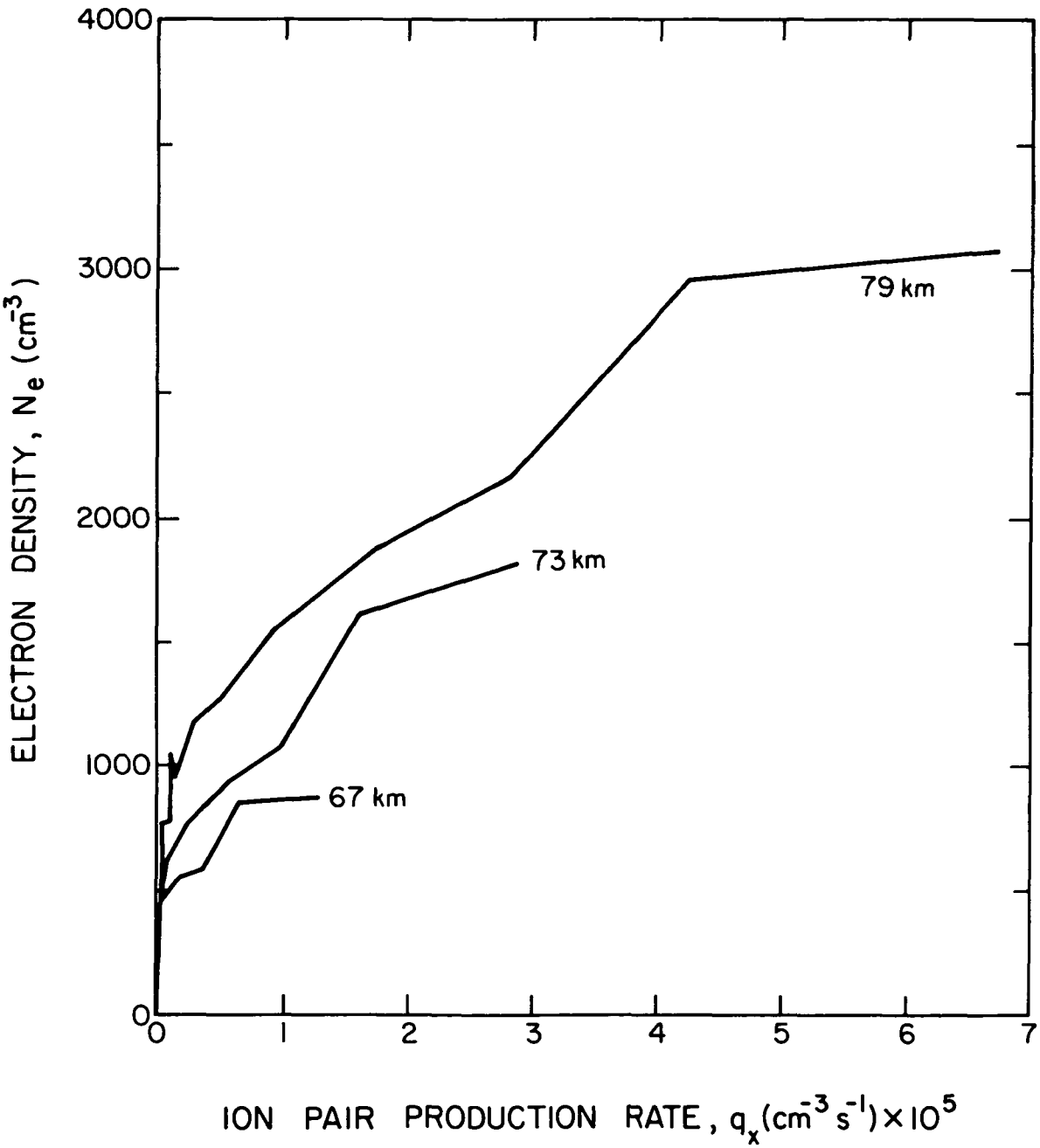

Figure 5.35 Estimated q_x from GOES data vs. incoherent scatter measurement of N_e over Arecibo (from Figure 2.4) for flare event of January 5, 1981.

strongest enhancement, at about 70 km, occurs at an altitude which had very little scatter immediately before the flare occurred. It is also worth noting the contrast with the data from Mathews: the electron density always increases with altitude, but the coherent scatter effect is confined to a few layers, with the maximum at about 70 km. This is in general agreement with the Urbana data.

5.4 Discussion of results

The data presented here show considerable areas of agreement with theory in that several altitudes for four flares show simultaneous effects, some of which indicate a proportionality of q with N, others showing a quadratic relationship. Five flares show delayed enhancements, with the delay often increasing with decreasing altitude as predicted by the model of Thomas et al. (1973). The estimates of q_0 suggest variations dominated by the solar zenith angle.

The spread of points about the suggested line of slope 1 of the q_x/q_0 vs q_x is at times so broad, presumably due to turbulence, that the choice between the two q vs N hypotheses cannot be made with assurance.

The huge enhancements which appear and disappear suddenly at the peak of the flare for the May 21, 1980 event, and perhaps the June 2, 1982 event are not accounted for by current theory. Perhaps a peculiar hydrated-proton reaction scheme suddenly slows recombination at a certain threshhold level of additional radiation; or the variation of refractive index at the length scale of the incident wave is greater than that which the theory of Chapter 4 predicts for the increase in N.

Another unexplained feature is the absence of increases in scattered power at altitudes showing preflare levels above noise (e.g., Figure 5.27, 78 km). This feature is probably not due to unknown chemical features; the

relationship between q and N may well fit one of the proposed models. Rather, the absence of an enhancement of scattered power may be due to a source of electromagnetic scatter which does not change with sudden changes in N.

For completeness, it must be mentioned that there are several flare events which meet the criteria of X-ray event size (from Section 5.1), but which fail to produce a scattered power enhancement, nor any enlargement of the set of altitudes producing valid velocity measurements. These are the events of April 14, 1978 (1652 CST), May 28, 1980 (1125 CST, earlier in the day of an observed flare event), November 14, 1980 (945 CST, earlier in the day of an observed flare event), February 26, 1980 (1400 CST), February 10, 1982 (1407 CST), July 14, 1982 (1250 CST), July 21, 1982 (1110 and 1240 CST), September 15, 1982 (1231 CST), and December 15, 1982 (1037 CST).

The sizes of these X-ray events range from 0.2×10^{-4} to 4×10^{-4} watts/meter^2 in the band 0.1-0.8 nm. Thus, some of the flare events which failed to produce coherent scatter observations are quite large. Most of these times show strong evidence of some form of interference to an extent which prevents reliable geophysical measurements. However, the remaining events may merit further investigation.

6. SUMMARY AND SUGGESTIONS FOR FUTURE WORK

6.1 Summary

We have developed the theoretical background necessary to compare coherent-scatter power data with current models of solar-flare D-region effects. Coherent-scatter data have been examined for times of X-ray events larger than a certain size, and 13 power enhancements have been identified in the period from April 1978 to December 1983. Hα flare size and SID importance have been noted for these flares, although these parameters have been judged less than adequate as criteria for determining which coherent-scatter records to examine.

Spectral modeling of solar X-ray emissions based on GOES X-ray detector data allows the estimation of Chapman theory photoionization rates integrated over all relevant wavelengths. This yields an electron production function q_x at each altitude during the times of solar flares. A theory of coherent backscatter and a set of possible ion-chemical recombination schemes have been used to compare the effects observed with the Urbana MST radar with the time evolution of this estimated $q_x(t)$ at a given altitude. It has been noted which type of chemical scheme agrees best with the coherent-scatter data at each altitude for each flare, and the following patterns of behavior have been observed:

1) For several flare events, at several altitudes, equilibrium assumptions with regard to chemical relaxation and turbulent mixing are validated by the coincidence of the $q_x(t)$ and $P(t)$ curves.

2) For several flare events, delayed (nonequilibrium) effects are evident at some altitudes; that is, the $P(t)$ curve lags the $q_x(t)$ curve significantly. These delayed effects tend to occur at the lowest altitudes,

with delay tending to decrease with increasing altitude. This lends some support to the ion recombination model of Thomas et al. (1973), but may also be due to turbulent mixing delay. Delayed effects tend to occur for flare observations of large solar zenith angles.

3) An extremely large enhancement in power, inconsistent with theories of chemical relaxation and coherent scatter presented in this work, is evident in the range 70 to 78 km for a few flares; the most pronounced of such effects are found in the data of the two flares at the smallest zenith angles, on days close to the summer solstice.

4) Apparent power enhancements which fit the chemical and scatter models in this work, and which occur above a steady baseline of scattered power, are confined to altitudes below 80 km. The absence of such effects above 80 km appears to be due chiefly to erratic turbulence patterns at the higher altitudes.

5) There is a strong zenith angle dependence on the altitudes showing no coherent-scatter power enhancement (Figure 5.32). The altitudes showing a response for high zenith angles are the very lowest, whereas Chapman theory would predict deposition of ionizing energy at higher altitudes for greater zenith angles.

6) A rough estimate of q_0, the preflare ion-pair production rate, may be made from the flare time data by the procedure described in Chapter 4. Estimates so made show some dependence on zenith angle, with greater values of q_0 corresponding to smaller χ, as expected. This demonstrates that such estimates have some degree of reliability, although the absolute accuracy is not estimated here.

7) Enhancements are sometimes entirely absent at altitudes which show scattered power levels well above noise and which appear to be relatively

constant during non-flare times. This may be due to radar energy getting absorbed at lower altitudes to a greater extent during the flare, or may suggest a coherent-scatter mechanism which does not increase with N(t). In any event, the absence of an enhancement in scattered power at the time of a flare, at an altitude showing significant pre-flare scatter, is not predicted by the simple models in this work.

8) At a few altitudes and flare events, the peak scattered power leads the maximum of the time curve for q_x by as much as two minutes. A scattered power peak leading the q_x peak also cannot be accounted for by the simple models used in this work.

9) Plots of P and q_x which coincide may be subjected to an analysis which distinguishes between the relationships A) $q = \alpha N^2$ and B) $q = \beta N$. The Urbana data suggest both occur in the mesosphere, depending on geophysical conditions not analyzed in this work. The incoherent-scatter data of Mathews (1984) support the possibility of relationship A occurring even in the lower D region, under at least some circumstances.

We conclude from these observations that coherent-scatter radar provides a powerful tool for the analysis of D-region flare effects. As with the previous methods of D-region flare effect observation described in Chapter 2, suitable analysis of coherent-scatter data can yield information about chemical schemes and geophysical conditions in the mesosphere. Particular strengths of the coherent-scatter method are the temporal and spatial resolutions achievable: about one minute and three kilometers, respectively, with the Urbana system. The coupling of turbulent scatter with background electron density gradients also has some drawbacks: some altitudes cannot be analyzed due to absent or erratic turbulence; and even the most favorable altitudes yield only a relative N, allowing determination

of $\Delta N/N_0$ at a single altitude, but not a comparison of the electron density at one altitude with that at another. The types of information provided by coherent scatter thus complement those from other methods.

6.2 Suggestions for future work

It would be good to continue the same sort of analysis at Urbana. Data have been collected nearly daily since 1983, providing a richer database than the one examined in this work. An analysis involving more flare effects may allow further isolation of the conditions which influence the features of the flare effects. It is likely that zenith angle, day of year, year of solar-cycle, and perhaps gravity wave intensity and other geophysical conditions influence the quantities we examine in this work. A richer database could help isolate the effects of each of these conditions. However, since the time from 1983 to the present is near the minimum of the sun-spot cycle, we may expect fewer flare effect occurrences per time of observation in the more recent data than were found in the time span examined by this work, 1978-1983.

The effects numbered 4, 7 and 8 above merit further investigation. The theory in this work does not account for the huge power enhancements shown for some flares, layers of scattered power which do not seem to change during a large flare event, or power curves which lead the estimated $q_x(t)$ curve at a given altitude. A more complex theoretical treatment may account for such effects, and yield further insights into D-region processes.

Combined rocket probes with coherent scatter data collection, even during nonflare conditions, may further make clear the relation between electron density and coherent-scattered power (the relationship may not be as simple as the one described in Chapter 4).

Rocket probes and other methods such as incoherent scatter allow

inference about the molecular constituents of the mesosphere. More research of this sort is needed, and further gas-phase chemical reaction rates need to be determined, in order to develop a more adequate overall set of chemical schemes which ultimately relate q to N.

The solar X-ray spectral development of this work is based on rather small numbers of measured high-resolution solar spectra. Future observations of solar X-ray spectra and development of the underlying solar physical theory should improve the accuracy of estimates of q_x.

If such improvements are made in the theory pertaining to the estimation of q_x and ion recombination schemes, we may be able to isolate the two effects which give rise to a delay of the power enhancement curve behind the q_x curve. If we have a good idea which delays are principally due to chemical relaxation, and which are due to turbulent mixing delay, we might be able to infer facts about the turbulence parameters at several altitudes from the flare-time scattered power response at those altitudes.

Planned enhancements of the Urbana radar system will increase spatial resolution significantly in the future. This should allow collection of more independent spatial samples of parameters estimated from solar-flare analysis, such as q_0. We may be able to thus map out concentrations of trace constituents which contribute to q_0, such as NO, or which affect the nature of the recombination or attachment coefficients, such as hydrated protons.

APPENDIX A. LISTING OF FLAREMASTER5

```
1  REM  FLAREMASTER5 IS INTENDED TO BE FINAL THESIS VERSION OF FLARE ANAL
     YSIS ROUTINE.
2  REM  IT USES GQ INTEGRATION FOR QX ESTS AND WRITES RESULTS TO A POWW-L
     IKE FILE
3  REM  FILE PRODUCED HAS 1 OR 2 AVGD CS POWER LINES AND 1 OR 2 QX LINES,
      ALL MEASURED IN CENTIBELS
4  REM  NOTE HEADER CHANGED: L$ HAS ALTITUDES AVERAGED ADDED, A6 CONTAINS
     PRE-FLARE AVGD VALUE (RAW, NOT CBS) AND L2 CONTAINS NUM LINES
5  REM  AND H4 CONTAINS AVERAGE ALT.
10 D$ =  CHR$ (4)
11 B$ =  CHR$ (7)
12 PI = 3.14159265358979
13 I1 = .387 / 2: REM  I1,I2 ARE GQ NORMALIZERS
14 I2 = .5065
15 GC = 4.09E - 6
16 LX =  LOG (10)
17 AA = 1.69E - 6
18 CC = 9.5E - 24
19 D = 2.8
20  DEF  FN G(X) = 1 + .4227843351 * (X - 2) + .41184033 * (X - 2) ^ 2
30  DIM XR(240,2): REM   CONTAINS   XRAY FLUX IN CENTIBELS ABOVE 10^-8
40  DIM CS%(240,20)
50  DIM QR(240): DIM QS(240)
60  DIM PAV(240)
70  DIM Y(2,6): DIM G(2,6): DIM W(6)
99  GOSUB 8000: REM  INITIALIZE Y,G,W
100  GOSUB 1000
103  GOSUB 2000
104  PRINT B$
105  INPUT "ZENITH ANGLE IN DEGREES: ";CHI
106  POKE 216,0
108 CHI = CHI * PI / 180
110  INPUT "WHICH HTS (IN KM), FROM:";LHT
120  IF LHT = 0 THEN  GOTO 9999
130  INPUT "TO: ";HHT
135 H4 = (LHT + HHT) / 2
140  PRINT "AVERAGE HT IS: ";H4
150  INPUT "AIR NUM DENSITY (IN M^-3) AT THAT ALT IS:";NA
160  INPUT "SCALE HT IN M AT SAME ALT: ";HS
170  INPUT "REL. FLARE START TIME: ";TSTART
180  INPUT "REL. FLARE END TIME: ";TZ
190  INPUT "REL. START TIME FOR PRE-FLARE AVG DESIRED: ";TB
200  INPUT "REL. END TIME OF PFA: ";TC
220 ZZ = 0
230  INPUT "ALL PARAMETERS OK? (1=YES,0=NO)";ZZ
235  PRINT "MAKE SURE DEST. DISK IN SLOT"
240  IF ZZ = 0 GOTO 104
```

```
250  GOSUB 3000
260  GOSUB 4000
270  GOSUB 6000
280  GOTO 110
999  END
1000  REM  INPUT X-RAY FILE  TO XR(120,2)
1002  INPUT "HOW MANY XR FILES?: ";II
1004 T9 = II * 120
1006  FOR I = 1 TO II
1008  PRINT "FILE"; SPC( 1); STR$ (I);" START TIME: ";
1009  INPUT TGIVEN(I)
1010  NEXT I
1015 TTRUE = 60 *  INT (TGIVEN(1) / 100) + (TGIVEN(1) - 100 *  INT (TGIVE
     N(1) / 100))
1018  FOR I = 1 TO II
1020  PRINT D$;"VERIFY XR/";TGIVEN(I)
1030  ONERR  GOTO 10000
1040  PRINT D$;"OPEN XR/";TGIVEN(I)
1050  PRINT D$;"READ XR/";TGIVEN(I)
1055 X1 = (I - 1) * 120 + 1
1056 X2 = X1 + 120 - 1
1060  FOR T = X1 TO X2
1070  INPUT XR(T,1): INPUT XR(T,2)
1080  NEXT T
1090  PRINT D$;"CLOSE XR/"TGIVEN(1)
1100  NEXT I
1999  RETURN
2000  REM  INPUT CS DATA FROM POWW FILE
2005  PRINT "READING POWW FILE"
2007  FOR I = 1 TO II
2010  PRINT D$;"VERIFY POWW/";TGIVEN(I)
2020  ONERR  GOTO 10000
2030  PRINT D$;"OPEN POWW/";TGIVEN(I)
2040  PRINT D$;"READ POWW/";TGIVEN(I)
2050  GOSUB 7000
2055 X1 = (I - 1) * 120 + 1
2056 X2 = X1 + 120 - 1
2060  FOR Z = 1 TO 20
2070  FOR T = X1 TO X2
2080  INPUT CS%(T,Z)
2090  NEXT T
2100  NEXT Z
2110  PRINT D$"CLOSE POWW/";TGIVEN(I)
2120  NEXT I
2999  RETURN
3000  REM  COMPUTE SATELLITE-PREDICTED ELECTRON PRODUCTION FUNCTION, QS(T
     )
3010 AQ = AA * NA / D
3015 CQ = CC * NA * HS /  COS (CHI)
3020  FOR T = TSTART TO TZ
3030 R = 10 ^ ((XR(T,2) - XR(T,1)) / 100)
3040 B =  LOG (R) /  LOG (2) - 1
3050  GOSUB 8500: REM  CALCULATE A FROM INTEGRAL
```

```
3080 PD = (B + 1 + D) / D
3100 QS(T) = AQ * A *  FN G(PD) * CQ ^  - PD
3110  NEXT T
3999  RETURN
4000  REM  COMPUTE RADAR-BASED ESTIMATE OF ACTUAL QX/Q0, IN QR(T)
4010 LOHT =  INT ((LHT - H2) / 1.5 + .5)
4020 HIHT =  INT ((HHT - H2) / 1.5 + .5)
4050  FOR T = 1 TO T9
4055 PAV(T) = 0
4060  FOR Z = LOHT TO HIHT
4070 PAV(T) = PAV(T) + 10 ^ (CS%(T,Z) / 100)
4080  NEXT Z
4090 PAV(T) = PAV(T) / (HIHT - LOHT + 1)
4100  NEXT T
4190 PB = 0
4200  FOR T = TB TO TC
4210 PB = PB + PAV(T)
4220  NEXT T
4230 PB = PB / (TC - TB + 1)
4300  FOR T = TSTART TO TZ
4310 QR(T) = PAV(T) / PB - 1
4315  IF QR(T) < 0 THEN QR(T) = 10000
4320  NEXT T
4999  RETURN
5000  REM  ROUTINE TO CONVERT TO HR,MIN NOTATION
5010 HR =  INT ((TTRUE + T - 1) / 60)
5020 MIN = TTRUE + T - 1 - 60 *  INT ((TTRUE + T - 1) / 60)
5999  RETURN
6000  REM  PRINT TABLE OF RESULTS
6005  GOTO 6150: REM  SKIP PRINTING
6010  PRINT "AVERAGE CS POWER FROM ALTITUDES ";LHT;" TO ";HHT
6020  PRINT "HR","MIN","POWER","DBS"
6030  FOR T = 1 TO T9
6040  GOSUB 5000
6050  PRINT HR,MIN,PAV(T),10 *  LOG (PAV(T)) / LX
6060  PRINT H4
6100  PRINT "ESTIMATES OF QX(CM^-3,S^-1),QX/Q0 FOR HT ";H2;" KM"
6105  PRINT "HR";" ";"MIN","QX","QX/Q0","QX DB","QX/Q0 DB"
6110  FOR T = TSTART TO TZ
6115  IF QR(T) <  = 0 GOTO 6140
6116  IF QR(T) = 10000 GOTO 6140
6120  GOSUB 5000
6130  PRINT HR;" ";MIN,QS(T) / 1E6,QR(T),10 *  LOG (QS(T)) / LX,10 *  LOG
    (QR(T)) / LX
6140  NEXT T
6150 F$ = "TX/" +  STR$ (H3(1))
6151 F$ = F$ +  STR$ (M3(1))
6152 F$ = F$ + "."
6153 F$ = F$ +  STR$ (LHT)
6154 F$ = F$ + "-"
6155 F$ = F$ +  STR$ (HHT)
6160  PRINT D$;"OPEN";F$
6170  PRINT D$;"DELETE";F$
```

```
6180  PRINT D$;"OPEN";F$
6190  PRINT D$;"WRITE";F$
6200 L3 = T9 / 60
6210 A6 = PB
6212  IF II = 1 GOTO 6220
6215  IF S2(1) > S2(2) THEN S2(1) = S2(2)
6220 T8 = 20 * 120 - 2 * T9
6222 M$ = L$ + " ALTS AV'D FROM "
6224 M$ = M$ +  STR$ (LHT)
6226 M$ = M$ + " TO "
6227 M$ = M$ +  STR$ (HHT)
6228 M$ = M$ + " KM."
6230  PRINT M$
6240  PRINT H3(1): PRINT M3(1): PRINT N3(1)
6250  PRINT S2(1): PRINT L3: PRINT A6
6260  PRINT H4
6270  REM  CREATE BOGUS ALTS
6280  FOR T = 1 TO T9
6290 P% =  INT (100 *  LOG (PAV(T)) / LX)
6300  PRINT P%
6310  NEXT
6319  IF TSTART = 1 THEN  GOTO 6360
6320  FOR T = 1 TO TSTART - 1
6330 P% =  - 999
6340  PRINT P%
6350  NEXT
6360  FOR T = TSTART TO TZ
6370 P% =  INT (100 *  LOG (QS(T)) / LX)
6380  PRINT P%
6390  NEXT
6399  IF TZ = T9 THEN  GOTO 6444
6400  FOR T = TZ + 1 TO T9
6410 P% =  - 1000
6420  PRINT P%
6430  NEXT
6444  FOR T = 1 TO T8
6450  PRINT 0
6460  NEXT
6470  PRINT D$;"CLOSE";F$
6999  RETURN
7000  REM  READ HEADER
7010  INPUT L$: INPUT H3(I): INPUT M3(1)
7020  INPUT N3(I): INPUT S2(I): INPUT L2
7030  INPUT A6: INPUT H2
7040  RETURN
8000  REM  INITIALIZE Y,G,W
8010 W(1) = .1713244923
8020 W(2) = .3607615730
8030 W(3) = .4679139345
8040 W(4) = W(3):W(5) = W(2):W(6) = W(1)
8045  REM  2 SETS OF 6 GAUSS-QUAD NODES
8050 Y(1,1) = 0.013067149
8060 Y(1.2) = 0.065555984
```

```
8070 Y(1,3) = 0.147327188
8080 Y(1,4) = 0.239672813
8090 Y(1,5) = 0.321444016
8100 Y(1,6) = 0.373932851
8110 Y(2,1) = 0.4212041912
8120 Y(2,2) = 0.5585974460
8130 Y(2,3) = 0.7726393823
8140 Y(2,4) = 1.014360618
8150 Y(2,5) = 1.228402554
8160 Y(2,6) = 1.365795809
8165  REM  1-8 A CHAMBER RESPONSE AT NODES
8170 G(1,1) = 1.3720506E - 8
8180 G(1,2) = 5.4828782E - 7
8190 G(1,3) = 3.5587326E - 6
8200 G(1,4) = 6.1757465E - 6
8210 G(1,5) = 6.1306138E - 6
8220 G(1,6) = 5.7315707E - 6
8230 G(2,1) = 4.1248167E - 6
8240 G(2,2) = 3.8205141E - 6
8250 G(2,3) = 1.5494062E - 6
8260 G(2,4) = 2.1812467E - 7
8270 G(2,5) = 1.6217009E - 8
8280 G(2,6) = 1.870358E - 9
8499  RETURN
8500  REM  COMPUTE GAUSS QUAD EST. OF A
8510 J1 = 0:J2 = 0
8520  FOR I = 1 TO 6
8530 J1 = J1 + W(I) * G(1,I) * Y(1,I) ^ B
8540 J2 = J2 + W(I) * G(2,I) * Y(2,I) ^ B
8550  NEXT
8560 J3 = I1 * J1 + I2 * J2
8570 A = 10 ^ (XR(T,2) / 100) * 1E - 8 * GC / J3
8571  REM  THE 1E-8 IS NECESSARY SINCE THE XR FILE IS CENTIBELS ABOVE 1E-
     8 W/M^2
8580  REM  PRINT T;SPC(1);A;SPC(1);LOG(A)/LX;SPC(I);B
8999  RETURN
9999  PRINT "BYE": END
10000  REM  ERROR HANDLING ROUTINE
10010  PRINT "FILE ACCESS ERROR, CAUGHT BY ONERR"
10020  POKE 216,0
10030  END
```

APPENDIX B. LISTING OF FLAREPLOT

```
10 REM FLARE PLOT 21:00:0. . .. .
20 REM USED WITH APPLE DISK FILES OF CS DATA
30 REM JAY PARKER
40 DIM P[240],Q[240],D[20,120],L$[80],T$[3],M$[80]
50 DEG
60 ENTER 2,+,N$
70 ENTER 2,+,H3
80 ENTER 2,+,M3
90 ENTER 2,+,N3
100 ENTER 2,+,S2
110 ENTER 2,+,L2
120 ENTER 2,+,A6
130 ENTER 2,+,H2
140 IF N3-120 THEN 160
150 MAT D=ZER
160 FOR J=1 TO N3
170 FOR I=1 TO 20
180 ENTER 2,+,D[J,I]
190 NEXT J
200 NEXT I
210 FOR I=1 TO L2/2
220 FOR T=1 TO 120
230 P[T+120*(I-1)]=1+D[I,T]/100)^-10↑S2
240 Q[T+120*(I-1)]=D[L2/2+I,T]/100-6
250 NEXT T
260 NEXT I
270 A7=A6-10↑S2
280 L1=POS(M$,".")
290 L$=M$[1,L1-1]
300 L$[L1]=","
310 L$[L1+1]=M$[L1+1]
320 PRINT L$
330 DIM S$[128]
340 S$="CST"
350 PRINT "LOCAL START TIME";M3+H3*100;S$
360 PRINT "NO. OF RECORDS=";N3
370 PRINT "# MINUTES IS";60*L2
380 PRINT "AVE IS";A6
390 SCALE -80,700,-15,115
400 PRINT "H2=AVE ALT.=";H2
410 OFFSET 0,0
420 PEN
430 H1=H2
440 REM TITLE
450 IPLOT 100,-112,1
460 LABEL (*,1.5,1.7,0,8/11)L$
470 SCALE 0,5.5/4.75*11,0,5.5/4.75*8.5
480 OFFSET 0.75*5.5/4.75+2,3.5*5.5/4.75+2
490 XAXIS -2,1,-2,3.5
```

```
500 XAXIS 3.5,1,-2,3.5
510 YAXIS -2,1,-2,3.5
520 YAXIS 3.5,1,-2,3.5
530 FOR I=-2 TO 3
540 PLOT -2,I,1
550 CPLOT -3,-0.3
560 LABEL (*)I
570 NEXT I
580 FOR I=-2 TO 3
590 PLOT I,-2,1
600 CPLOT -1,-1.5
610 LABEL (*)I
620 NEXT I
630 DISP "FLARE START REL TIME?";
640 INPUT T1
650 DISP "FLARE REL END TIME?";
660 INPUT T2
670 DISP "PRINT VALUES (NO=0)";
680 INPUT R9
690 PLOT -2,3,1
700 CPLOT 1,1
710 LABEL (*)"EST LOG(0%/Q0)"
720 PLOT -2,3
730 CPLOT 1,0
740 LABEL (*)"ASSUMES 0=AN↑2"
750 PLOT 2,-2,1
760 CPLOT 0,2
770 LABEL (*)"LOG(0%)"
780 PLOT 2,-2,1
790 CPLOT 0,1
800 LABEL (*)"(CM↑-3,S↑-1)"
810 FOR T=T1 TO T2
820 IF P[T]<A7 THEN 860
825 IF LOG(P[T]/A7-1).LOG(10)<-2 THEN 860
826 IF Q[T]<-2 THEN 860
830 IF R9=0 THEN 850
840 PRINT T,P[T],LOG(P[T]/A7-1)/LOG(10),Q[T]
850 PLOT Q[T],LOG(P[T]/A7-1)/LOG(10),-2
860 NEXT T
870 OFFSET 6.15*5.5/4.75+2,3.5*5.5/4.75+2
880 XAXIS -2,1,-2,3.5
890 YAXIS 3.5,1,-2,3.5
900 XAXIS 3.5,1,-2,3.5
910 YAXIS -2,1,-2,3.5
920 PLOT -2,3,1
930 CPLOT 1,1
940 LABEL (*)"EST LOG(0%/Q0)"
950 PLOT -2,3
960 CPLOT 1,0
970 LABEL (*)"ASSUMES 0=BN"
980 PLOT 2,-2,1
990 CPLOT 0,2
1000 LABEL (*)"LOG(0%)"
1010 PLOT 2,-2,1
1020 CPLOT 0,1
```

```
1030 LABEL (*)"(CM↑-3,S↑-1)"
1040 FOR T=T1 TO T2
1050 IF P[T]<A7 THEN 1080
1060 IF LOG(SQR(P[T]/A7)-1)/LOG(10)<-2 THEN 1080
1065 IF Q[T]<-2 THEN 1080
1070 PLOT Q[T],LOG(SQR(P[T]/A7)-1)/LOG(10),-2
1080 NEXT T
1090 PEN
1100 FOR I=-2 TO 3
1110 PLOT -2,I,1
1120 CPLOT -3,-0.3
1130 LABEL (*)I
1140 NEXT I
1150 FOR I=-2 TO 3
1160 PLOT I,-2,1
1170 CPLOT -1,-1.5
1180 LABEL (*)I
1190 NEXT I
1200 PEN
1210 SCALE 0,60*L2/10*11,0,4/2.5*8.5
1220 OFFSET 60*L2/10+0.75,4/2.5*0.5+1
1230 XAXIS -1,5,0,5-5+(M3/5-INT(M3/5))
1240 XAXIS -1,5,5-5*(M3/5-INT(M3/5)),60*L2
1250 YAXIS 0,1,-1,3
1260 PEN
1270 PLOT 0,3,1
1280 CPLOT 1,0
1290 LABEL (*)"LOG CS POW. ABOVE PRE-FLARE AVG."
1300 PLOT 0,3,1
1310 CPLOT 1,-1
1320 LABEL (*)"LOG Q!! (CM↑-3,S↑-1)"
1330 FOR T=1 TO 60*L2
1340 PLOT T,LOG(P[T]/A7)/LOG(10),-2
1350 NEXT T
1360 PEN
1370 FOR T=1 TO L2*60
1380 IF Q[T]<-1.5 THEN 1400
1390 PLOT T,Q[T],-2
1400 NEXT T
1410 PEN
1420 FOR I=-1 TO 3
1430 PLOT 0,I,1
1440 CPLOT -3,-0.3
1450 LABEL (*)I
1460 NEXT I
1470 PLOT 60-M3,-1,1
1480 CPLOT -2,-1.5
1490 LABEL (*)H3+1
1500 LABEL (*)"00"
1510 PLOT 120-M3,-1,1
1520 CPLOT -2,-1.5
1530 LABEL (*)H3+2
1540 LABEL (*)"00 CST"
1550 PEN
1560 END
```

REFERENCES

Abramowitz, M. and Stegun, I. A. (1964) (Eds.), Handbook of mathematical functions, National Bureau of Standards, U. S. Government Printing Office, Washington.

Banks, P. M. and G. Kockarts (1973), Aeronomy, Part A, Academic Press, New York.

Bleiweiss, M. P. (1972), Solar X-ray spectrum definition and the prediction of ionospheric radio wave propagation, NELC/TR 1840, Naval Electronics Laboratory Center, San Diego.

Dasgupta, M. K., R. K. Mitra, and S. K. Sarkar (1973), Some studies on the association of solar optical flares and microwave bursts with sudden ionospheric disturbances, J. Atmos. Terr. Phys., 35, 805-813.

Dellinger, J. H. (1937), Sudden ionospheric disturbances, Terr. Mag. and Atmos. Elec., 42, 49-54.

Deshpande, S. D., and A. P. Mitra (1972a), The flare spectrum below 10 Å deduced from satellite observations, J. Atmos. Terr. Phys., 34, 229-242.

Deshpande, S. D., and A. P. Mitra (1972b), The quantitative relationship of flare X-rays to SIDs, J. Atmos. Terr. Phys., 34, 243-254.

Deshpande, S. D., and A. P. Mitra (1972c), Electron density profiles deduced from measurements of SCNAs and VLF phase and amplitude, J. Atmos. Terr. Phys., 34, 255-266.

Deshpande, S. D., C. V. Subrahmanyam and A. P. Mitra (1972a), The statistical relationship between X-ray flares and SIDs, J. Atmos. Terr. Phys., 34, 211-227.

Deshpande, S. D., S. Ganguly, V. C. Jain and and A. P. Mitra (1972b), The

flare event of 30 January 1968 and its implications, J. Atmos. Terr. Phys., 34, 267-282.

Donnelly, R. F. (1977), Solar X-ray measurements from SMS-1, SMS-2, and GOES-1 information for data users, NOAA Technical Memorandum ERL SEL-48.

Gibbs, K. P. and S. A. Bowhill (1983), An investigation of turbulent scatter from the mesosphere as observed by coherent-scatter radar, Aeron. Rep. No. 110, Aeron. Lab., Dep. Elec. Eng., Univ. Ill., Urbana-Champaign.

Gradshteyn, I. S., and I. M. Ryzhik (1965), Tables of integrals, series, and products, Academic Press, New York.

Hargreaves, J. K. (1979), The upper atmosphere and solar-terrestrial relations, Van Nostrand Reinhold Co., New York.

Heath, D. F. (1973), Space observations of the variability of solar irradiance in the near and far ultraviolet, J. Geophys. Res., 78, 2779-2792.

Hocking, W. K. (1983), The relationship between strength of turbulence and backscattered radar power at HF and VHF, Handbook for MAP, Vol. 9, SCOSTEP Secretariat, Univ. Ill., Urbana-Champaign, 289-301.

Kreplin, R. W., T. A. Chubb, and H. Friedman (1962), X-ray and Lyman-Alpha emission form the sun as measured from the NRL SR-1 satellite, J. Geophys. Res., 67, 2231-2253.

Manson, J. E. (1972), Measurement of the solar spectrum between 30 and 128 Å, Solar Phys., 27, 107-131.

Mathews, J. D. (1984), The incoherent scatter radar as a tool for studying the ionospheric D-region, J. Atmos. Terr. Phys., 46, 975-986.

May, B. R. (1966), The behaviour of the D-region at mid-latitudes during a sudden ionospheric distubance, J. Atoms. Terr. Phys., 28, 553-564.

Mechtly, E. A., S. A. Bowhill and L. G. Smith (1972), Changes of lower ionosphere electron concentrations with solar activity, J. Atmos. Terr. Phys., 34, 1899-1907.

Miller, K. L., S. A. Bowhill, K. P. Gibbs and I. D. Countryman (1978), First measurements of mesospheric vertical velocities by VHF radar at temperate latitudes, Geophys. Res. Lett., 5, 939-942.

Mitra, A. P. (1974), Ionospheric effects of solar flares, Reidel Publishing Co., Dordrecht-Holland.

Mitra, A. P. (1975), D-region in disturbed conditions, including flares and energetic particles, J. Atmos. Terr. Phys., 37, 895-913.

Montbriand, L. E. and J. S. Belrose (1972), Effective electron loss rates in the lower D region during the decay of solar X-ray flare events, Radio Sci., 7, 133-142.

NOAA (1976), U. S. Standard Atmosphere, 1976, National Oceanic and Atmos. Admin., U. S. Government Printing Office, Washington.

NOAA (1981), Sudden ionospheric disturbances, Solar-Geophys. Data, 438 (Supplement), 27-30.

Narcisi, R. S., A. D. Bailey, L. E. Wlodyka and C. R. Philbrick (1972), Ion composition measurements in the lower ionosphere during the November 1966 and March 1970 solar eclipses, J. Atmos. Terr. Phys., 34, 647-658.

Rastogi, P. K. and S. A. Bowhill (1975), Remote sensing of the mesosphere using the Jicamarca incoherent-scatter radar, Aeron. Rep. No. 68, Elec. Eng. Dep., Univ. Ill., Urbana-Champaign.

Ratnasiri, P. A. J., and C. F. Sechrist Jr. (1975), An investigation of the solar zenith angle variation of D-region ionization, Aeron. Rep. No. 67, Elec. Eng. Dep., Univ. Ill., Urbana-Champaign.

Roth, P. (1982) (Ed.), Research in Aeronomy October 1, 1981-March 31, 1982, Progress Report 82-1, Aeron. Lab., Dep. Elec. Eng., Univ. Ill., Urbana-Champaign.

Rottger, J. (1983), Origin of refractive index fluctuations in the mesosphere as opposed to the stratosphere and troposphere, Handbook for MAP, Vol. 9, SCOSTEP Secretariat, Univ. Ill., Urbana-Champaign, 143-144.

Rowe, J. N., A. J. Ferraro, H. S. Lee, R. W. Kreplin, and A. P. Mitra (1970), Observations of electron density during a solar flare, J. Atmosph. Terr. Phys., 32, 1609-1614.

Thomas, L., P. M. Gondhalekar, and M. R. Bowman (1973), The influence of negative-ion changes in the D-region during sudden ionospheric disturbances, J. Atmosph. Terr. Phys., 35, 385-395.

Tucker, W. H. and M. Koren (1971), Radiation from a high-temperature, low-density plasma: the X-ray spectrum of the solar corona, Astrophys. J., 168, 283-311.

USNO (1976), The American ephemeris and nautical almanac for the year 1978, U. S. Naval Observatory, Dept. of the Navy, U. S. Government Printing Office, Washington.